IMPROVED UPSCALING & WELL PLACEMENT STRATEGIES FOR TIGHT GAS RESERVOIR SIMULATION AND MANAGEMENT

A Thesis

by

YIJIE ZHOU

Submitted to the Office of Graduate Studies of
Texas A&M University
in partial fulfillment of the requirements for the degree of

DOCTOR OF PHILOSOPHY

Chair of Committee,	Michael J. King
Committee Members,	Akhil Datta-Gupta
	Eduardo Gildin
	Yalchin Efendiev
Head of Department,	Daniel Hill

August 2013

Major Subject: Petroleum Engineering

ABSTRACT

Tight gas reservoirs provide almost one quarter of the current U.S. domestic gas production, with significant projected increases in the next several decades in both the U.S. and abroad. These reservoirs constitute an important play type, with opportunities for improved reservoir simulation & management, such as simulation model design, well placement. Our work develops robust and efficient strategies for improved tight gas reservoir simulation and management.

Reservoir simulation models are usually acquired by upscaling the detailed 3D geologic models. Earlier studies of flow simulation have developed layer-based coarse reservoir simulation models, from the more detailed 3D geologic models. However, the layer-based approach cannot capture the essential sand and flow. We introduce and utilize the diffusive time of flight to understand the pressure continuity within the fluvial sands, and develop novel adaptive reservoir simulation grids to preserve the continuity of the reservoir sands. Combined with the high resolution transmissibility based upscaling of flow properties, and well index based upscaling of the well connections, we can build accurate simulation models with at least one order magnitude simulation speed up, but the predicted recoveries are almost indistinguishable from those of the geologic models.

General practice of well placement usually requires reservoir simulation to predict the dynamic reservoir response. Numerous well placement scenarios require many reservoir simulation runs, which may have significant CPU demands. We propose a novel simulation-free screening approach to generate a quality map, based on a combination of static and dynamic reservoir properties. The geologic uncertainty is taken into consideration through an uncertainty map form the spatial connectivity analysis and variograms. Combining the quality map and uncertainty map, good infill well locations and drilling sequence can be determined for improved reservoir management. We apply

this workflow to design the infill well drilling sequence and explore the impact of subsurface also, for a large-scale tight gas reservoir.

Also, we evaluated an improved pressure approximation method, through the comparison with the leading order high frequency term of the asymptotic solution. The proposed pressure solution can better predict the heterogeneous reservoir depletion behavior, thus provide good opportunities for tight gas reservoir management.

DEDICATION

To my parents Xianbin Zhou and Qingfen Wang for their love and support

ACKNOWLEDGEMENTS

I would like to express my sincere gratitude to my graduate advisor Dr. Michael King for his continuous support and efforts to my Ph.D. study and research. He expertly guided me through my graduation education. It is an honor to have such a great advisor and mentor.

I would like to extend my gratitude to Dr. Akhil Datta-Gupta, who provided valuable mentoring and encouragement during my study, and some of the insights become part of this work.

I would like to thank Dr. Gildin and Dr. Efendiev for serving on my committee, for their encouragement, insightful comments, and suggestions for this work.

I would like to thank my colleagues in the Model Calibration and Efficient Reservoir Imaging group (MCERI) for their precious help and discussion. Thanks also go to all the faculty and staff at Petroleum Engineering Department, Texas A&M University for providing great resources and environment.

TABLE OF CONTENTS

Page

LIST OF FIGURES

Page

LIST OF TABLES

Page

1. INTRODUCTION

1.1 Motivation

Tight gas reservoirs have been playing an important role in the current U.S gas production. Figure 1-1 shows the statistics of U.S. gas production in 2011(Figure 1-1a) and 2013 (Figure 1-1b), we can see that tight gas reservoirs provide almost one quarter of the U.S. gas production, and will continue increase the production in the next several decades.

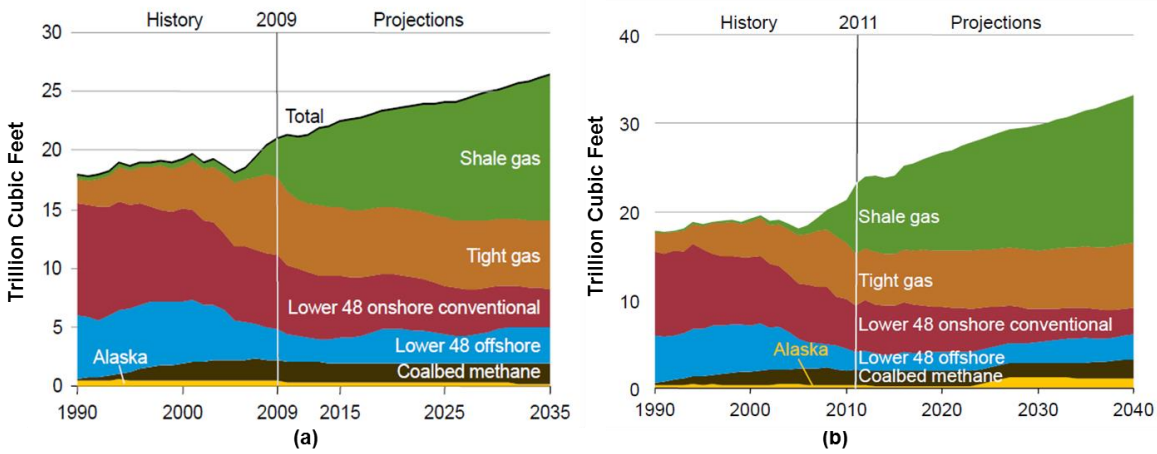

Figure 1-1: U.S. nature gas production. (a): EIA, annual energy outlook 2011; (b): EIA, annual energy outlook 2013;

With the increasing importance of tight gas resources, tight gas reservoir simulation and management become very important and challenging, for our reservoir studies. Our research work, including the design the simulation models using novel upgridding & upscaling techniques, rapid simulation-free well placement workflow, and efficient pressure solution in heterogeneous systems, would provide good opportunities for improved tight gas reservoir simulation and management.

Firstly, to acquire the deep understanding of the reservoir heterogeneity, interactions between wells and fractures, complex reservoir dynamic responses which associated with depletion history, robust and efficient reservoir simulation models are required. Unfortunately, geologic descriptions about the fluid-rock properties, from geophysical or petrophyscial measurements and interpretations are typically limited in smaller scale, core/log scale, thus become very expensive for routine simulation work. Upgridding & upscaling techniques are required to obtain the coarse models, or simulations models. Great effort has been put into developing robust upgridding & upscaling strategies for conventional oil reservoirs. However, such strategies may not be applicable in the unconventional tight gas reservoirs, due to their special reservoir heterogeneities. First part of our research is to develop novel upgridding & upscaling strategies for tight gas reservoir simulation.

Secondly, well placement in an infill drilling program is a routine procedure for reservoir management. Once we have the simulation models, general practice of well placement usually requires reservoir simulation to predict the dynamic reservoir response. Numerous well placement scenarios require many reservoir simulation runs, which may have significant CPU demands, and this is only for one specific realization. Furthermore, to account for the geologic uncertainty, people tend to consider multiple realizations, thus make it more expensive, even impractical, for large scale simulation for each realization. Another part of our research is to develop a rapid simulation-free procedure to determine infill well locations, which also takes the subsurface uncertainty into consideration.

Lastly, both the upgridding design and well placement research work need some understanding of the reservoir depletion behavior, like drainage volumes, pressure depletion, etc., which can be acquired from the Fast Marching Method and geometric pressure approximation. However, these methods cannot provide accurate pressure solutions, due to the underlying assumptions, especially within a more heterogeneous

medium. Therefore, they cannot provide accurate drainage volume or pressure change history associated with depletion time. Last part of our research is to evaluated an improved pressure approximation method, through the comparison with the leading order high frequency term of the asymptotic solution, theoretically, and further extend its applications for tight gas reservoir management.

In summary, tight gas reservoir poses some interesting and challenging questions for reservoir simulation and management work, like the complex spatial pattern, intermittently connected fluvial sand packages within a non-pay background, hydraulically fractured wells with different trajectories within the near well region, interactions between different fractures or wells. This work tries to take on some of the challenges, and also provide some understanding of the tight gas reservoirs.

1.2 Research Objectives

The ultimate objective of our research work is to provide the robust and efficient approaches for the tight gas reservoir simulation and management, which includes the following details:

First, we provide robust upgridding & upscaling strategies to build accurate and efficient simulation models, which can achieve at least one-order magnitude simulation speed-up. As for the upgridding:

1. We studied the characteristic of tight gas reservoirs, and explored the current upgridding methods, layer-based coarsening, studied its applications in tight gas reservoirs, which will be discussed in the following section.
2. We analyzed underlying assumptions that associated with upscaling calculation, and identified the most important assumption, which is pressure equilibrium/continuity within a coarse cell, for tight gas upgridding & upscaling. We also understood the reason why current layer-based coarsening cannot work for tight gas reservoir, during the error analysis.

3. We introduced the diffusive time of flight to check the pressure equilibrium/continuity within a coarse cell, also guide us to develop the adaptive coarsening strategies.

As for the upscaling:

1. We compared current two upscaling methods, permeability upscaling, and transmissibility upscaling, and found out that transmissibility upscaling can better preserve the flow barriers and tortuosity.
2. We explored the impact of pressure boundary on the upscaling calculation, proposed local seal side point source and line source transmissibility calculations. These two calculations provide the lower estimation and upper estimation of the upscaled transmissibility, and the average of two bounds gives a more accurate estimation.

Second, we develop an efficient well placement approach for large scale tight gas field application, propose an appropriate drilling sequence/ schedule for the tight gas development.

1. We studied the current well placement approaches, and they all require the flow simulation, thus become computational expensive for the large scale field development.
2. We proposed a quality map, based on a combination of static properties and dynamic property, through the analysis of well productivity. The quality map could basically match with the exhaustive flow simulations.
3. We proposed an uncertainty map to access the subsurface uncertainty, the uncertainty map also match with the results from multiple realizations, which is the current uncertainty assessment method.
4. We explored the impact of subsurface uncertainty on the well placement and field recovery predictions in tight gas reservoirs.

In the end, we evaluated an improved pressure approximation method, through the comparison with the leading order high frequency term of the asymptotic solution in tight gas systems.

1. We studied the limitations of current geometric pressure approximation method.
2. We evaluated an improved pressure approximation method, through the comparison with the leading order high frequency term of the asymptotic solution and the unit analysis.
3. From the proposed improved pressure approximation, we derived the general conversion of the diffusive time of flight (τ) and pressure impulse actual time (t) in heterogeneous reservoirs. Also validated our approximation through a conceptual model.

1.3 Structure of the Thesis

The structure of this thesis is as follows:

Section 2 introduces the proposed adaptive upgridding & upscaling strategies for tight gas reservoir simulation. We begin with the introduction, then apply the previous strategies to the tight gas reservoir upgridding and upscaling, discuss the limitations of each strategy. After that, we investigate a full-field tight gas reservoir first, then, followed by a prior upscaling error analysis. The most significant upscaling errors will be identified through the analysis. Next, we design vertical adaptive upgridding and corresponding upscaling strategy, and test it with a 10x10 sector model. With the success of vertical adaptive upgridding method, we further extend it to fixed areal resolution plus adaptive vertical resolution grid design, and 3D adaptive grid design. The corresponding upscaling methods are also proposed and analyzed here. In the end, we will conclude this section with our discussions and recommendations about the adaptive upgridding & upscaling strategies.

Section 3 presents a rapid simulation-free procedure to determine infill well locations. We outline our approach and basic mathematical background first. Next, we demonstrate

this approach on a 10x10 test area of a U.S. on-shore tight gas reservoir model. After that, we utilize this approach to design an infill well drilling sequence for the large scale tight gas reservoir model. The influence of subsurface uncertainty is also discussed here. Without considering subsurface uncertainty, the sweet spots for well placement are often the un-depleted regions far from existing wells. However, these regions would also be the most risky in that we have the least confidence about the reservoir model far from well data. We contrast a multi-year drilling sequence, with and without this risk assessment and show the benefit including risk. We also contrast our approach with a uncertainty assessment based upon multiple realizations to further show the benefits of our proposed workflow. The efficiency of this workflow makes it feasible for large scale field application, providing good opportunities for improved tight gas reservoir management.

In section 4, we will show a detailed derivation of improved pressure solution and the validation. We start from a simple introduction of the asymptotic solution of the diffusivity equation, depth of investigation for symmetric flow in the homogeneous reservoir. Then we will further explore the asymptotic solutions in 3D, 2D and 1D. Through the comparison with the geometric pressure approximation, an improved pressure approximation is introduced, also the general conversion from diffusive time to actual time, which can also applied in the heterogeneous reservoir is derived. It is followed by a detailed comparison of the actual time, bottom hole pressure, etc, based on a conceptual model; This section is concluded with some discussions and future work proposal.

Section 5 is the general conclusion and discussion about our research work. We briefly discussed the potential and limitations of each part of our work, and then we will propose the future work plan to further extend this work.

Finally, in Appendix A, we present the derivation of Kriging interpretation, which could be utilized to access the reliability/uncertainty of the data in the static model. In appendix B, a simple illustration of the Fast Marching Method is introduced, which is the background of the geometric pressure approximation method.

2. ADAPTIVE UPGRIDDING & UPSCALING STRATEGIES FOR FLOW SIMULATION OF TIGHT GAS RESERVOIR MODELS *

2.1 Introduction

Great effort has been put into developing robust upgridding & upscaling strategies for conventional oil and gas reservoirs. However, some special characteristics of unconventional gas reservoirs, like its non-pay background, highly varied flow units, thin fluvial sand package with the intermittent channels, lead to the coarsening of such geologic models become very complex and challenging.

Previous studies had developed the non-uniform coarsening of geologic models for simulation grid design (Li et.al. 1995; Durlofsky et.al. 1997; Stern et.al. 1999; Fincham et.al. 2004; Sablok and Aziz 2005). Li and Beckner (2000) applied these techniques to simulation layer design. King et.al. (2006) and King (2007A) developed a more effective error measure which also lead to the definition of an optimal layering scheme. The latter has been further extended by Hosseini and Kelkar (2010), Du et.al. (2010) and Kelkar and Atiq (2010). The last study was applied to tight gas reservoirs. However, tight gas reservoir models are some of the most complex as they must represent intermittent reservoir continuity, fractured well performance, and a transition from near well local drawdown to large scale global pressure depletion over the lifetime of a field. None of these strategies can capture the essential reservoir heterogeneity and connectivity, thus, are not applicable for tight gas reservoir simulation model design.

For these reservoir simulation models to be useful they must preserve important characteristics of the fine scale description, while at the same time providing rapid

enough calculations that they can be used for reservoir management decisions. That is the context of this work. King et.al (2006) first proposed a vertical adaptive coarse grid, based upon the knowledge of the errors which limit the robustness and accuracy of an upscaling flow calculation. The adaptive coarse grid is designed to capture the reservoir connectivity, which can minimize the most important source of the tight gas upscaling errors. Our work based on the similar error analysis, here, pressure transient Diffusive Time of Flight is introduced to understand tight gas reservoir pressure continuity. Based on the concept of pressure equilibrium, we design and adapt the spatial resolution of the simulation grid to honor the continuity of the reservoir sands.

The specific upscaling techniques we apply are also fairly distinctive. We compare the flow based transmissibility upscaling with the permeability upscaling, and demonstrate that simply using a single upscaled permeability as the simulation scale flow parameter will introduce systematic biases which will under-estimate well performance or over-estimate lateral reservoir continuity, or both. Our approach is an extension of that presented by King et.al.(1998), King (2007B), and is similar to that of Chen et.al.(2008, 2009). Other authors have studied transmissibility based upscaling and near well modeling (White and Horne 1987; Ding 1995; Durlofsky et.al. 2000; Muggeridge et.al. 2002), but few have explored the advantages of the two in combination. In addition, because of the spatially adaptive nature of our simulation grid design, purely local upscaling gives an excellent representation of flow. There is no need for either extended-local or global upscaling as is often otherwise the case (Holden and Nielsen, 2000, Wen et.al. 2003, Wu et.al. 2007).

Our approach has three key technical elements: (1) we explicitly preserve the local continuity of the reservoir sands in the geologic model through the design of the simulation grid. Each simulation cell is an adaptive amalgamation of the geologic scale corner point cells. (2) We have developed a “Well Index” based upscaling, to determine the upscaled permeability and which preserves the local reservoir quality. It does not

require knowledge of the well locations within the upscaled simulation model, but it will preserve the performance of these wells. (3) The heterogeneity within each sand is preserved through the use of transmissibility upscaling, which we show performs systematically better than the usual permeability upscaling. In combination, these three elements provide simulation results which are almost indistinguishable from the fine scale model. We develop and demonstrate our calculations on sector model taken from the center of a full field onshore U.S. tight gas reservoir. The results are then validated using the full field model. Our approach differs from earlier studies which have attempted to preserve the global heterogeneity of the reservoir models though layer-based statistical calculations. Although these statistical approaches are superior to uniformly coarsened models, they are not as robust or as accurate as the current work constrained by local continuity. Our approach also differs in the use of accurate property upscaling techniques that simultaneously preserve the internal contrast of permeability within each sand, and the performance of wells within the model.

We apply this combination of techniques to the tight gas sector model and obtain 1x1xN upscaled results that are almost indistinguishable from the fine scale model (Zhou and King, 2011). However, the simulation run time reduction is not sufficient, and so we perform a 2x2, 3x3 areal coarsening. This provides the desired speed-up although the results are not quite as accurate as for the 1x1xN upscaling. These results are then replicated with the full field model, where we validate the understanding developed using the sector model. A further extension of the strategies is 3D adaptive simulation grid, which is designed based on the concept of depth of investigation. 3D adaptive allows variable resolution in both vertical and horizontal direction, thus, would lead to some bizarre cell geometry, like “U” or “L” shape geometry. 3D adaptive upgridding could get minimum cell count, and still preserve the internal connectivity within each cell. However, upscaling calculation based on such grid is still an open question, we proposed some transmissibility upscaling methods, but each method has its own limitation, further investigation is still required.

2.2 Motivation: Limitations of Previous Strategies

This section will show the previous upgridding and upscaling strategies' applications in tight gas reservoirs. Test model is the sector model mentioned before, and will be discussed in details later. We will apply the uniform layering, non-uniform layering and adaptive coarsening proposed by King et.al. (2006) in this sector model, and discuss the limitations of each method.

Uniform layering is the earliest upgridding & upscaling strategies, which is to merge the fine scale layers into coarse layers uniformly, according to a constant ratio. Figure 2-1 shows the recoveries of different uniform coarsened models (1x1x5, 1x1x5) with permeability and transmissibility upscaling.

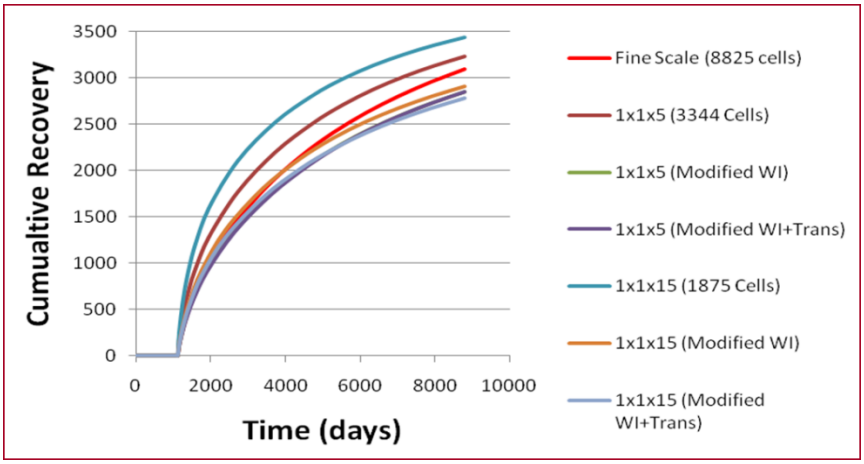

Figure 2-1: Recoveries of uniform coarsened models. Fine scale model recovery curve (red) is also included for comparison. Note that "WI" means the well index upscaling, and "WI + Trans" means the combination of well index upscaling and transmissibility upscaling.

The recovery of fine scale model is also included for comparison. Note that "WI" means the well index upscaling, and "WI + Trans" means the combination of well index

upscaling and transmissibility upscaling. Here, we could find none of these strategies works here for our tight gas sector model, since the coarse model are too homogeneous compared to reservoir response, and unable to capture the reservoir heterogeneity.

Non-uniform layering or statistical layering introduces a property P first as a measure of heterogeneity during coarsening. The coarsening algorithm relies on the analysis of "total variation" in a property P. The total variation is the sum of two terms: a "within cell" variation (W) and a "between cell" variation (B). For a 3D grid which has been coarsened to some extent, we have:

$$W = \sum_{ijk=1}^{NX,NY,NZ} n_{ijk} \cdot \left(P_{ijk} - P^{C}_{ijk}\right)^2 \tag{2-1}$$

$$B = \sum_{ijk=1}^{NX,NY,NZ} n_{ijk} \cdot \left(P^{C}_{ijk} - \bar{P}_{ij}\right)^2 \tag{2-2}$$

$$H = W + B = \sum_{ijk=1}^{NX,NY,NZ} n_{ijk} \cdot \left(P_{ijk} - \bar{P}_{ij}\right)^2 \tag{2-3}$$

Here

n_{ijk} is the bulk rock volume of each cell;

P_{ijk} is the static property of each cell at the fine scale;

$P^{C}_{ijk} = \sum_{k'} n_{ijk'} \cdot P_{ijk'} \Big/ \sum_{k'} n_{ijk'}$ is the coarsened static property of each cell;

$\bar{P}_{ij} = \sum_{k=1}^{NZ} n_{ijk} \cdot P_{ijk} \Big/ \sum_{k=1}^{NZ} n_{ijk}$ is the column based average of the static property;

Upon sequential coarsening, each property may be obtained by a recursive relationship from the averages of the previous layering scheme. For instance, the within cell variation obtained by merging two coarse cells a and b is given by:

$$W = W_a + W_b + \frac{n_a \cdot n_b}{\left(n_a + n_b\right)}\left(P_a - P_b\right)^2 \tag{2-4}$$

Equivalently, the within cell variation is increased by an amount

$$\delta W = \frac{n_a \cdot n_b}{(n_a + n_b)} (P_a - P_b)^2 \quad (2\text{-}5)$$

The algorithm is initiated with the number of layers within the geologic model with W=0 in all cells. Layer pairs are selected, recursively, to minimize the increase in δW. King et.al. (2006) and King (2007A) proposed an interstitial velocity of the Buckley-Leverett front as a measure of heterogeneity:

$$P = \frac{k}{\phi} f' \quad (2\text{-}6)$$

Where, f' is the Buckley-Leverett frontal speed, k is the permeability, ϕ is the porosity and the variance in that property across the layers is used as a figure of merit: small variance is suitable for coarsening while high variance does not. By sequential coarsening the layers which has the minimum δW, or heterogeneity loss, we can obtain the following curve:

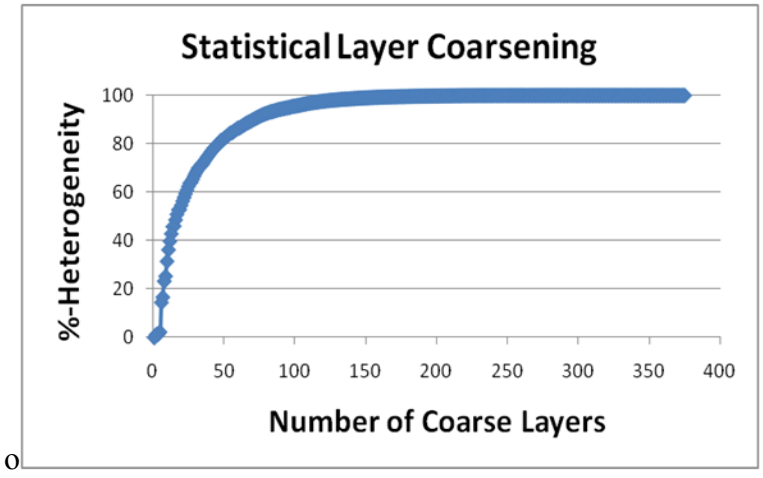

Figure 2-2: Heterogeneity preserved with the number of coarse layers. Statistical layering analysis is performed on the tight gas sector model

Figure 2-2 shows the results of statistical layering analysis, which tell us how much heterogeneity could be preserved with the corresponding number of coarse layers. For

this sector model, the optimal coarse layers would be 75 layers, which can preserve about 90% of heterogeneity. We can also coarsen further to obtain a low resolution coarse model, for example, 47 layers, which can preserve about 55% of heterogeneity.

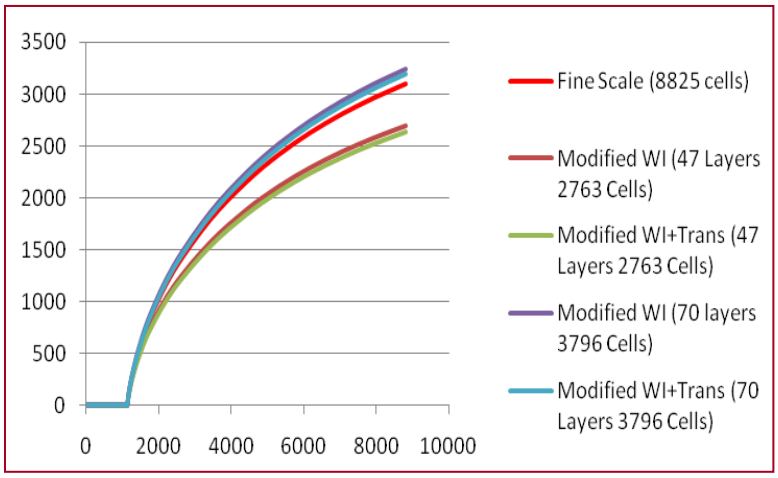

Figure 2-3: Recoveries of non-uniform coarsened models. Fine scale model recovery curve (red) is also included for comparison. Note that "WI" means the well index upscaling, and "WI + Trans" means the combination of well index upscaling and transmissibility upscaling.

Figure 2-3 shows the recoveries of non-uniform coarsened models, which include high resolution optimal layering model, and low resolution layering model. We could find that the optimal layering works better than the comparable uniform layering, however, it still cannot provide accurate results, since it cannot preserve the essential reservoir connectivity.

In order to preserve the reserve connectivity, King et.al. (2006) first proposed vertical adaptive coarsening, which is to design the simulation grid to preserve the reservoir sand connectivity, which becomes the starting point of our adaptive coarsening strategies.

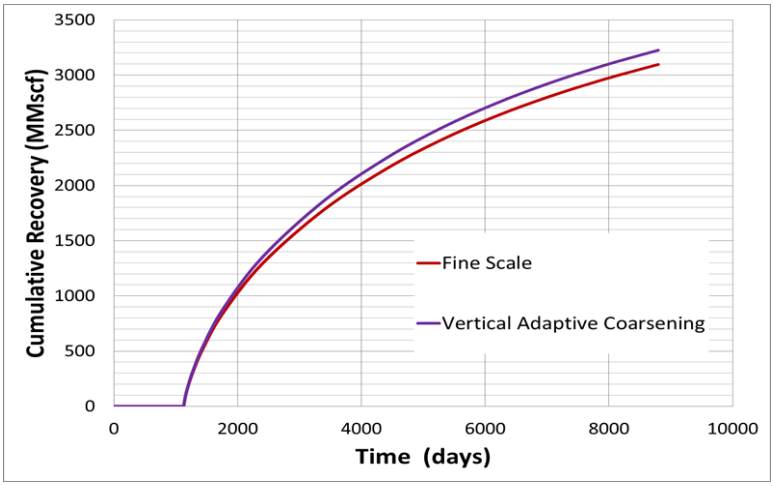

Figure 2-4: Recoveries of vertical adaptive coarsened model. Fine scale model recovery curve (red) is also included for comparison.

Figure 2-4 shows the recovery of vertical adaptive coarsened model. The adaptive coarsening can provide much better results, compared to the layer-based coarsening strategies. However, it still use the permeability upscaling to obtain the upscaled properties, which cannot preserve 3D flow tortuosity and barriers, therefore, the recovery is still not very accurate.

2.3 Geologic Models of Tight Gas Reservoir

The 3D geologic model is a conventional high resolution 3D model and is typical of such models routinely being constructed by operating companies (King et.al. 2006, Tobin et.al. 2010). Our model uses a simple sand/non-sand facies description to represent the thin fluvial channels. Non-net is defined using a permeability threshold. The full field model has in excess of $4x10^6$ cells, and we want to achieve a simulation run time reduction of at least an order or magnitude: hours reduced to minutes for the full field model and minutes to seconds for the sector model.

The example we will study is a tight gas reservoir high resolution geologic model, shown in Figure 2-5a. The model size is 103x108x375 cells. The cells are about 250 ft in width and length, and 1 foot in height. Therefore, the vertical resolution is much higher than the areal resolution. Red cells are non-pay, and its pore volume is close to 0. Usually these cells will be identified as inactive cells for reservoir simulation. Blue cells are pay, and they have non-zero permeability and pore volume. The pay cells will be identified as active cells for reservoir simulation. There are only 66,530 active cells for this full field geologic model. Therefore, the tight gas reservoir is usually formed on a non-pay background. There is also some intermittent connectivity, constituted by small sand packages.

Figure 2-5b shows the porosity of the pay cells only, the distribution is relatively uniform. The majority of the pay cells have porosity values from 10%~15%. Meanwhile, Figure 2-5c shows a relatively heterogeneous permeability distribution of the pay cells within this model, with a range of 0.0001 to 10 md. 70% of the pay cells permeability is above 0.1 md, while the other 30% of the permeability is below 0.1md.

As for the tight gas reservoir with such high heterogeneity, to preserve the barrier of the non-pay cells and flow channels of sands, to capture the internal reservoir heterogeneity become the crucial objective for our coarse grid design. Traditional layer based grouping, including the uniform layering and statistical layering, seems to lose its application in tight gas reservoir since it will inevitably merge the pay and non-pay cells into one coarse cell. A novel and effective grid design is required for the tight gas reservoir, or unconventional reservoir upgridding and upscaling.

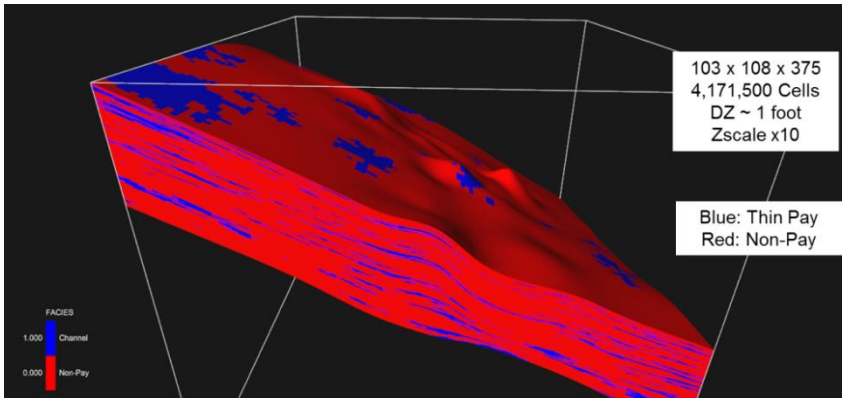

(a)

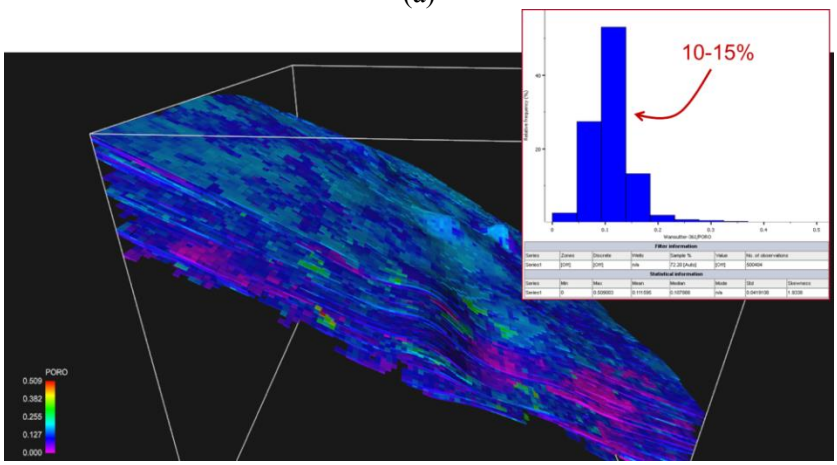

(b)

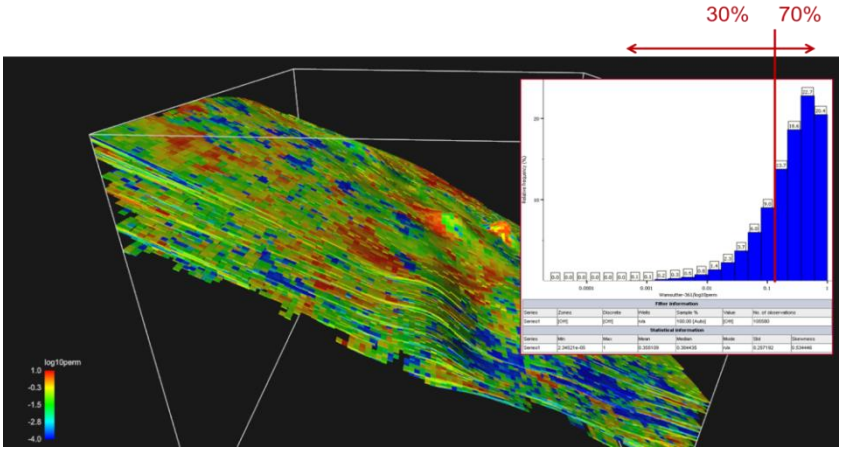

(c)

Figure 2-5: High resolution geologic model of our studied field. (a): Facies distribution, red cells are non-pay cells, and blue cells are pay cells; (b): Porosity distribution for the pay cells only; (c): Permeability distribution for the pay cells only.

We will begin our study using a detailed 10x10 sector model of the above tight gas reservoir, being depleted by a single well. To give a sense of the reservoir heterogeneity, the final pressure of the sector model (channel facies only) after being depleted for 8796 days is shown in Figure 2-6. The sector model has 10x10x375 = 37,500 cells, but only 8825 cells are active. From Figure 2-6, we could see that red cells have the lowest pressure, 1000-1200 psi. These portions of the reservoir are depleted due to the excellent communication with well. In contrast, the blue cells have the highest pressure of 3600-3800 psi, very close to the initial pressure. These volumes are isolated from the well.

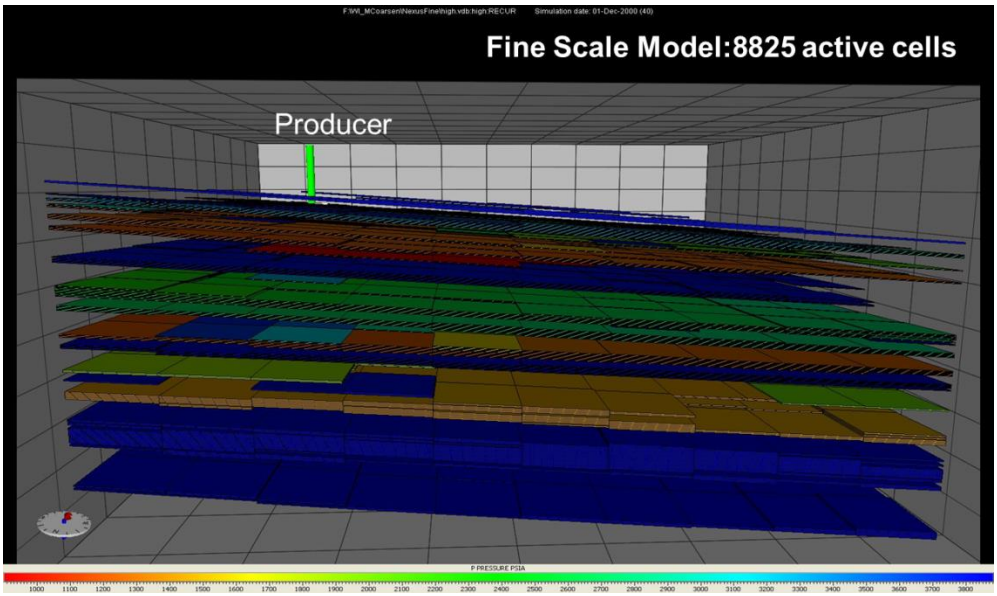

Figure 2-6: High resolution 375 layer 3D geologic model of a 10x10 test area of a tight gas reservoir.

As you can see, the depleted and isolated volumes are in close proximity. This reservoir model has the intermittent connectivity characteristics observed of tight gas reservoirs in the field. Our challenge is to preserve these characteristics during the upscaling process.

2.4 Errors and Biases in Upgridding & Upscaling

Upgridding & Upscaling usually requires some assumptions to make sure the whole coarsening process is correct. However, most of assumptions cannot be true in reality. Therefore, these assumptions will cause the residual errors that cannot be eliminated by upscaling process. But such errors could be minimized by the grid design. Knowledge of the sources of a priori upscaling errors can be used to obtain robust and accurate upgridding approach of high resolution geologic models.

2.4.1 A Prior Error Analysis in Upgridding

Table 1 summarizes three important assumptions for upgridding & upscaling, and their corresponding errors.

Assumptions	Corresponding errors
Pressure equilibrium within one coarse cell	Disconnect pay within the coarse cell will not be in pressure equilibrium
Single velocity within one coarse cell	Distribution of multiphase frontal velocities replaced by single value
Fluid velocity is parallel to the pressure drop	Flow may depend on the transverse pressure drop

Table 1: Assumptions and their corresponding errors

As discussed in King (2007A), there are three remaining errors which will be present, to some degree, in any upscaling calculation. Each error is consistent with certain assumptions that are made on the coarse grid. The most important assumption is that each coarse cell has a single cell pressure. For tight gas reservoirs this may be true so long as the coarse cell does not connect two thin fluvial channels that would otherwise be disconnected. If these channels are incorrectly connected, then it does not matter which upscaling techniques are applied, as the connectivity of the channels will no

longer be correct. Testing for this error is possible. We will show in the later section, how to design the simulation grid so that this error does not occur.

For multiphase flow, the next most important error is based on the assumption that there is only a single total velocity within each coarse cell. When performing a flow based upscaling calculation we impose pressure and/or no flow boundary conditions and calculate total flux per unit pressure drop to obtain the effective permeability. However, at the same time as we calculate the total flux we can calculate the local flow velocity and determine its variance on the fine scale. If we then consider the impact on multiphase flow, regions with high velocity variance will do a poor job of preserving the local spread in frontal motion, while regions of low variance will better preserve a flood front. This may be used to determine the quality of a coarse grid. It has been used to define an optimal coarse layering scheme by King et.al. (2006), and has later been extended by Hosseini and Kelkar (2010) and by Du et.al. (2010).

Finally, the remaining error is more of a current numerical limitation instead of a physical one. Especially when upscaling channelized systems, as the upscaling volume increases, so the does the strength of the off diagonal terms in the effective permeability tensor (White and Horne 1987; Kasap and Lake 1990; Durlofsky 1991; Pickup et.al. 1994; King 1995). Most of our simulators are unable to utilize these off-diagonal terms which will indicate that the flow velocity is not aligned with the pressure gradient. Once these terms become significant, then the quality of the upscaling calculation will again degrade.

In summary, and in order of importance: connectivity, velocity variance, and off-diagonal permeability tensor elements may be used as grid diagnostics to determine the a priori quality of a simulation grid. Unfortunately, layer based upgridding, including the uniform layering and statistical layering, will inevitably merge the pay and non-pay cells into one coarse cell. Therefore, the most significant error cannot be minimized using

layer based upgridding method. Compared to uniform layering, statistical layering will minimize the velocity/ slowness variance within one coarse cell. Therefore, statistical layering will minimize the second error, it may perform better than the uniform layering, which has been proved in the previous section.

To minimize the most significant error for tight gas reservoir upgridding, we need to make sure the pay and non-pay cells can never be merged together; pay can only merge with pay. Note that non-pay cells are barriers, but does pay cells are necessarily good flow conduits? If the answer is yes, then only merging the pay cells can guarantee the pressure equilibrium. However, if the answer is no, then this important assumption is not valid, this strategy will introduce errors. Here, we returned to a fundamental result of well test analysis to ask whether we should have pressure equilibrium within a coarsened cell.

When a well starts producing from a reservoir at initial conditions or when a well is shut in for a well test, there is an impulse created at the well which generates pressure waves which propagate into the reservoir. The depth up to which the pressure wave has propagated at any time is given by the term 'depth of investigation'. Specifically, we calculated the time it would take a pressure pulse to propagate across each cell in the geologic model using the depth of investigation.

$$\delta t_x = \frac{1896\phi\mu c_t}{k_x} \cdot DX^2(hours) \tag{2-7}$$

$$\delta t_z = \frac{1896\phi\mu c_t}{k_z} \cdot DZ^2(hours) \tag{2-8}$$

Here δt is the time for a pressure pulse to pass across a cell, in field units, and DX and DZ are the cell dimensions. The results are shown in Figure 2-7.

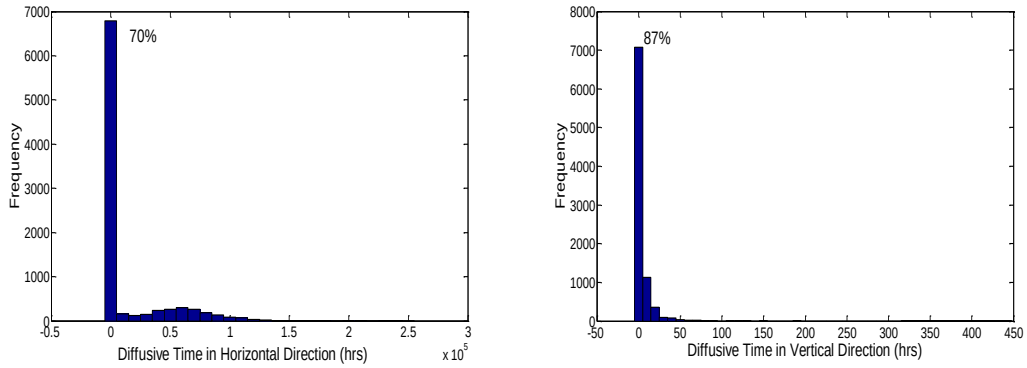

(a) (b)

Figure 2-7: Diffusive time of flight in horizontal and vertical direction. (a): Diffusive time in horizontal direction across each cell (channel facies only); (b): Diffusive time in vertical direction across each cell (channel facies only);

Interestingly, while the diffusive times in the vertical direction are measured in hours, the diffusive times for pressure equilibrium in the horizontal direction is measured in years for 30% of the cells. In other words, 30% of "pay" cells may act as baffles to horizontal gas depletion while being conduits of flow for vertical depletion. If we only work on the vertical coarsening, as long as only connected pay cells are merged, we can guarantee the pressure equilibrium. But if we work on the horizontal coarsening, 30% of horizontal baffles may introduce the upscaling errors.

2.4.2 Error Analysis in Upscaling

A good upscaling approach should be able to preserve the reservoir heterogeneity as much as possible. Currently we have two upscaling approaches, permeability upscaling and transmissibility upscaling. The mathematical expression for effective permeability upscaling and transmissibility upscaling had been studied earlier (Chen et al., 2003; Du et al., 2010). The permeability upscaling depends on the flow within a cell: from coarse cell face to coarse cell face. The transmissibility upscaling depends on the flow between cells: from coarse cell center to coarse cell center. Earlier studies have proven

permeability upscaling may lose the internal reservoir heterogeneity information, thus unable to provide a good reservoir simulation model. Figure 2-8 shows the difference of local transmissibility upscaling and permeability upscaling with a 2x4 upscaling example:

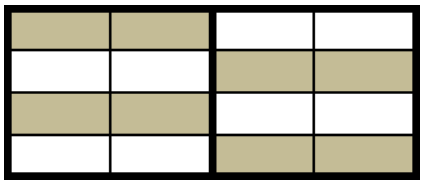

Figure 2-8: A diagram of 2x4 upscaling

The grey cell is non-pay, permeability is 0. And white cell is pay, permeability is 100 md. We merge this 4x4 cells into 2x1 coarse cells with 2x4 coarsening. For the permeability upscaling, the upscaled permeability of left coarse cell is 50 md, and right coarse cell is same. Therefore, the transmissibility between these two coarse cells is non-zero, which is calculated from the upscaled permeability. As for transmissibility upscaling, the transmissibility could be zero since there is no flow between these two coarse cells. Therefore, transmissibility upscaling would preserve the internal reservoir heterogeneity.

King et.al (1998) recognized that within a simulator we may choose to define the cell permeability to preserve the upscaled well productivity, and then modify the calculated transmissibility within the simulator through directional permeability multipliers to preserve the intercell transmissibility. This has the additional specific advantage of not requiring coarse cells to represent flow barriers. This significantly improves the ability of the coarse grid to simultaneously represent continuous coarse pay cells and continuous barriers as cell face properties.

Our upscaling techniques are summarized in Figure 2-9. The well index upscaling corresponds to radial flow around a well. As shown in Figure 2-9b, the productivity of a vertical well in the coarse cell is the weighted average of the vertical well productivities in each of the fine cells. This calculation is repeated along the three directions of the grid to obtain three upscaled well productivities, which are then transformed into cell permeabilities. Figure 2-9a also shows the transmissibility based upscaling for contrast. This is a flow based calculation of flow from coarse cell center to coarse cell center. It is essentially equivalent to the upscaling for the link permeability that characterizes flow between two coarse cells. As discussed in King et. al. (2008), this upscaling calculation refers to the fine scale permeabilities within each half of the coarse cell, and is sometimes called "half-cell" permeability upscaling. However, it is more accurate to think of it as intercell transmissibility or link permeability upscaling.

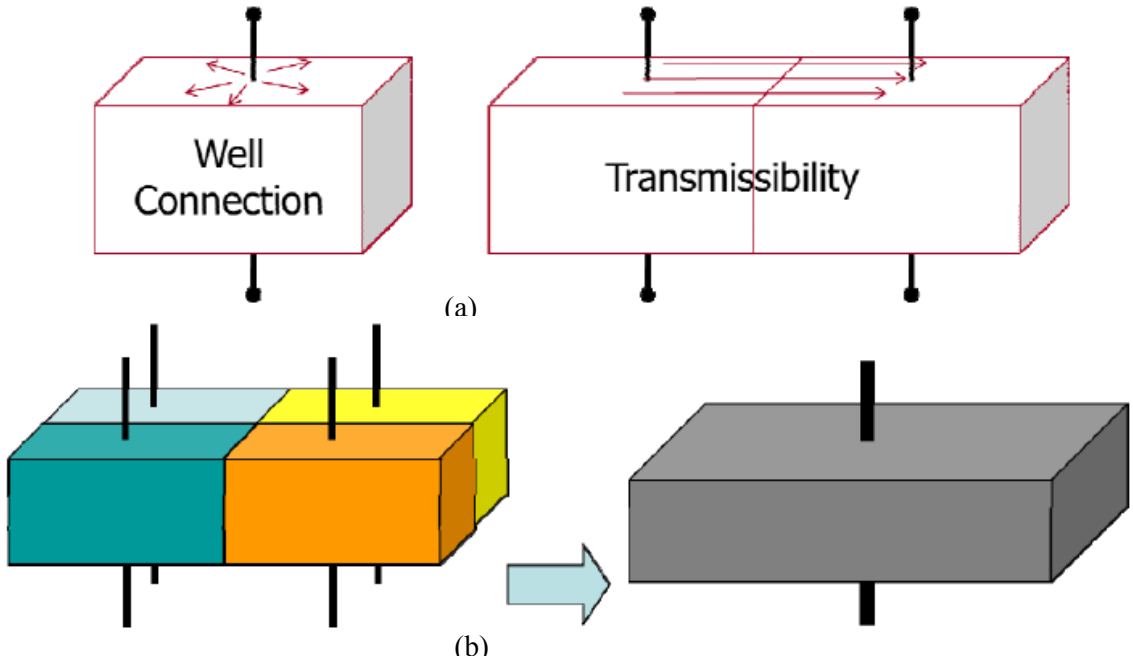

Figure 2-9: A illustration of upscaling strategies. (a): Well index and transmissibility based upscaling methods (b): Well index upscaling method.

It is worth noting the other characteristic of these two upscaling approaches. The well index based upscaling is similar to an arithmetic average and tends to approach an upper estimation. As such it is a good indicator of reservoir quality, but it is not sensitive to reservoir barriers. It is comparable to what we learn about a reservoir from the initial productivity of a well. In contrast, if the flow based calculation for link permeability is performed with sealed side boundary conditions, then it tends to approach a lower estimation, comparable to the harmonic average. In this case, the transmissibility upscaling calculation provides an excellent diagnostic of a reservoir barrier, but a very poor estimate of how a well would perform. This is demonstrated with the simple example of 3x3 upscaling of a channel system in Figure 2-10. In Figure 2-10a the channel system is upscaled using a sealed side flow based calculation of horizontal permeability. In Figure 2-10b, the upscaling uses the well index upscaling to obtain the cell permeability and a sealed side flow based calculation for the horizontal transmissibility. The zero transmissibility is marked as cell face properties.

In Figure 2-10a, the continuous high permeability channel has been replaced by a continuous, but lower quality channel. The dot on the diagram represents a vertical well placed within the channel. On the coarse grid, it now appears to be in a channel margin and has significantly reduced productivity. In contrast, in Figure 2-10b, the well index upscaling has preserved the continuity of the major channel, and almost all of the productivity of the well. However, on its own it has lost the channel margin barrier between the two channels. These barriers are reintroduced through the use of the sealed side flow based calculation for the intercell transmissibility. In combination, the coarse grid properties of Figure 2-10b provide a much more accurate representation of the original properties than any single upscaling calculation would on its own. We will use this combination of techniques to upscale the tight gas models, where they'll be shown to be extremely effective in providing a very accurate representation of the fine scale fluid flow.

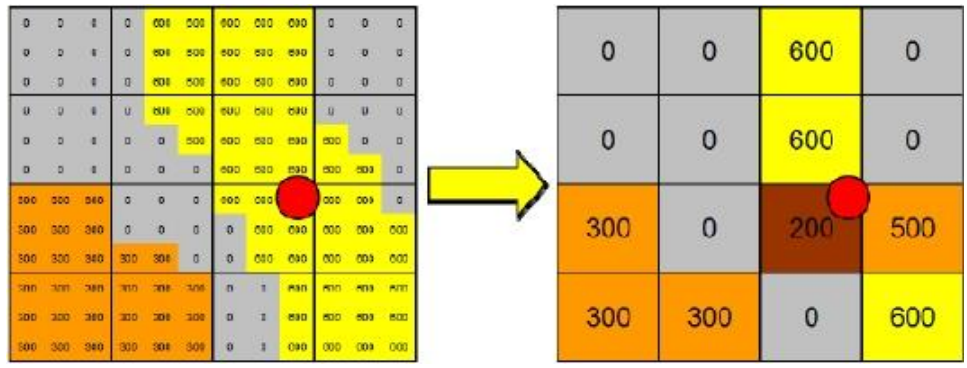

(a)

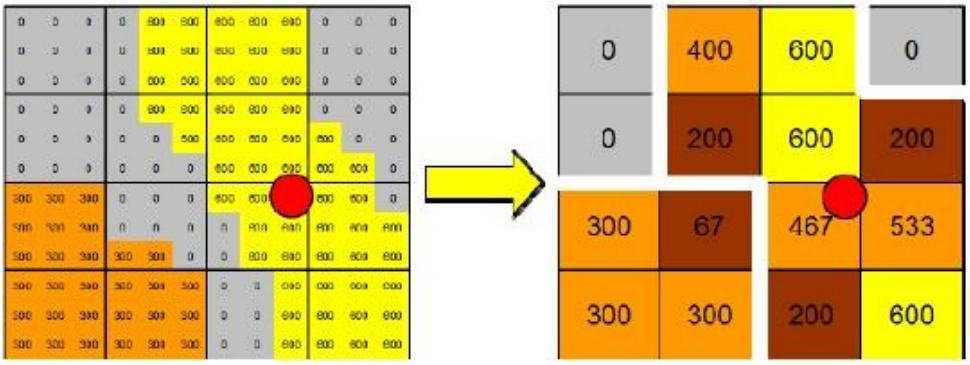

(b)

Figure 2-10: Permeability upscaling vs. Transmissibility upscaling. (a) Flow based permeability upscaling and (b) Combined well index and transmissibility upscaling.

2.5 1x1xN Adaptive Upgridding & Upscaling

2.5.1 1x1xN Upgridding & Upscaling Approaches

Based on the previous analysis, when vertically coarsening a reservoir model, once we merge pay, non-pay and, then pay again, we have the potential for amalgamating two distinct thin fluvial channels. We can choose to design a flow simulation grid in which pay and non-pay are never merged. Specifically, for our tight gas systems, we will perform 1x1xN upscaling, where N is variable throughout the model. We choose N to be no thicker than the thickness of a channel if within a pay cell, and choose N to be as thick as a stack of non-pay cells within not in a channel facies. This is a conservative

simulation grid which preserves the lateral resolution within the geologic model and is designed to never amalgamate distinct channels upon vertical coarsening. The concept of a layer is no longer present on the simulation grid, as instead we now appear to have an unstructured numerical problem. This style of unstructured grid may not be appropriate for waterfloods, since they may not correctly represent vertical segregation of fluids within a sand, but they will be shown to perform well for tight gas reservoirs.

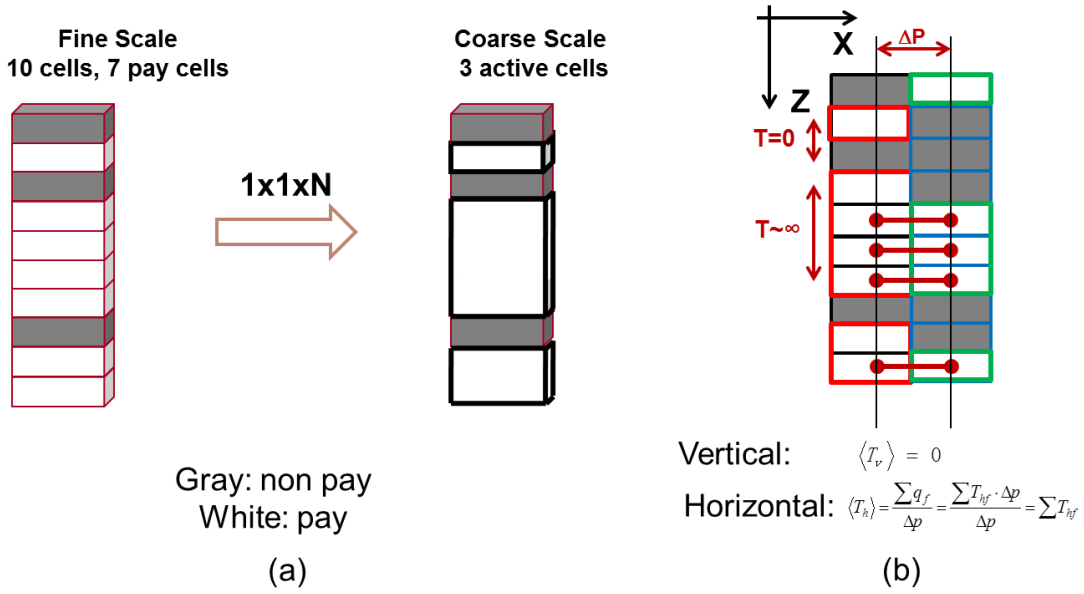

Figure 2-11: 1x1xN adaptive upgridding & upscaling. (a): 1x1xN adaptive upgridding, cells are only merged in vertical direction; (b):1x1xN high resolution upscaling strategy, vertical transmissibility between pay and non-pay is zero, and horizontal transmissibility would be the summation of horizontal flux/ transmissibility between two adjacent coarse cells;

Figure 2-11 shows 1x1xN coarsening strategy. Figure 2-11a shows the 1x1xN adaptive upgridding strategy, the connected pays are merged together in this column, and we would merge the model column by column according to this strategy, the internal reservoir connectivity and non-pay barriers could be preserved in 1x1xN coarse models. Figure 2-11b shows the 1x1xN transmissibility upscaling strategy, simple algebraic calculation is applied through the 1x1xN coarse grid to calculate the inter-cell transmissibility.

2.5.2 1x1xN Upgridding & Upscaling Results

The calculation was performed using the unstructured workflow of the Nexus simulator (Nexus 2010). It is possible to perform similar coarsening calculations in other commercial simulators, but was especially simple to implement in Nexus as described in King et.al. (2006). In this workflow the final scale reservoir model is provided to the simulator pre-processor, which calculates fine scale pore volumes, intercell transmissibilities, and well indices. Our upscaling code then creates coarse versions of these same properties. The fine scale grid is provided to the Nexus simulator, together with an "MCOARSE" array which tells the simulator how to coarsen the grid to build a coarse scale simulation model at run time. The results of the flow simulation are shown in Figure 2-12 for the upscaled sector model. This figure should be contrasted with Figure 2-6 which shows an almost identical distribution of pressures within the fine scale sector model.

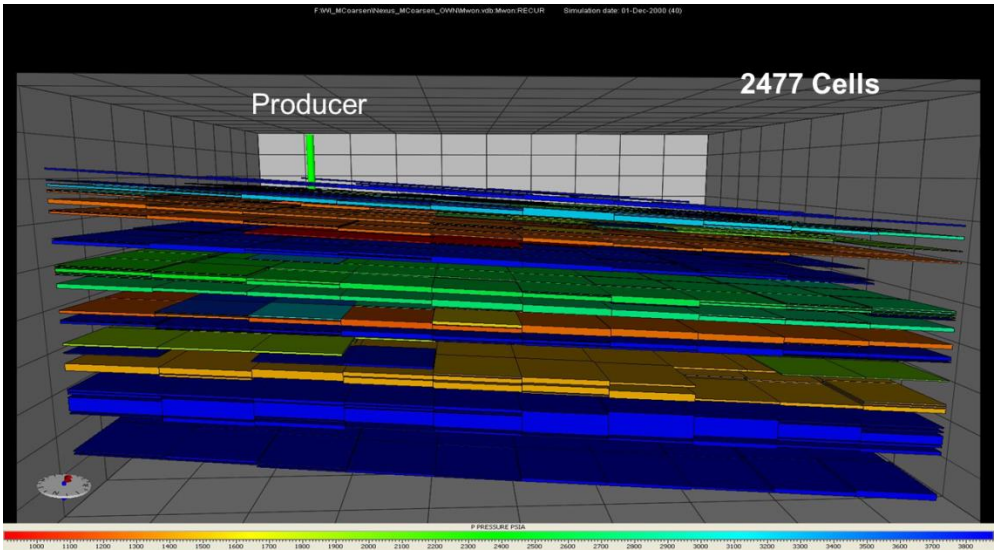

Figure 2-12: 1x1xN adaptive coarsening. Cells follow pay/non-pay contrast in each column of the model.

We contrast these results with layer based simulation grid design. Such grids will inevitably merge the pay and non-pay cells, therefore, it cannot preserve as much heterogeneity as the 1x1xN adaptive grid design. Figure 2-13 shows the 1x1 optimal layering strategy calculated from the statistical layering analysis of King et al., (2006), and conventional upscaling with 1x1x5 uniform coarsening, both has been briefly mentioned in the previous section.

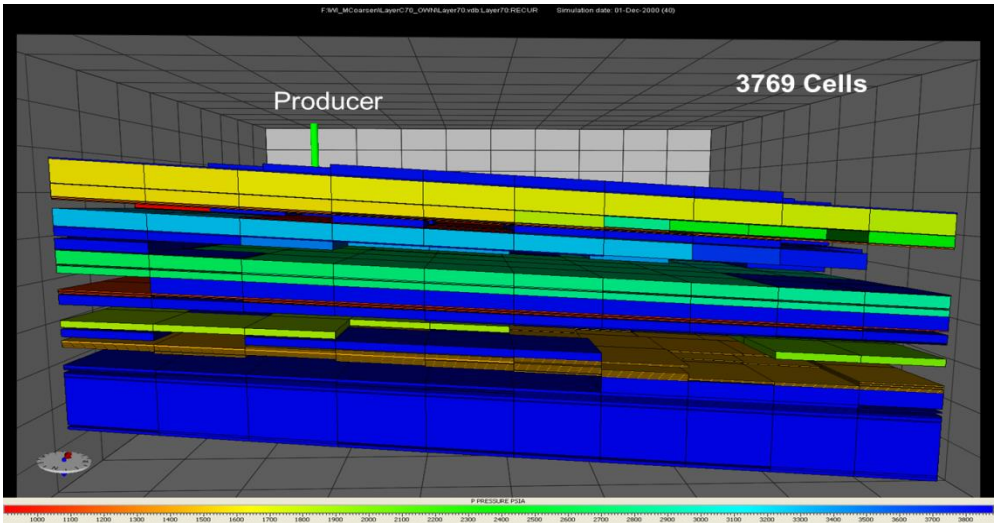

(a)

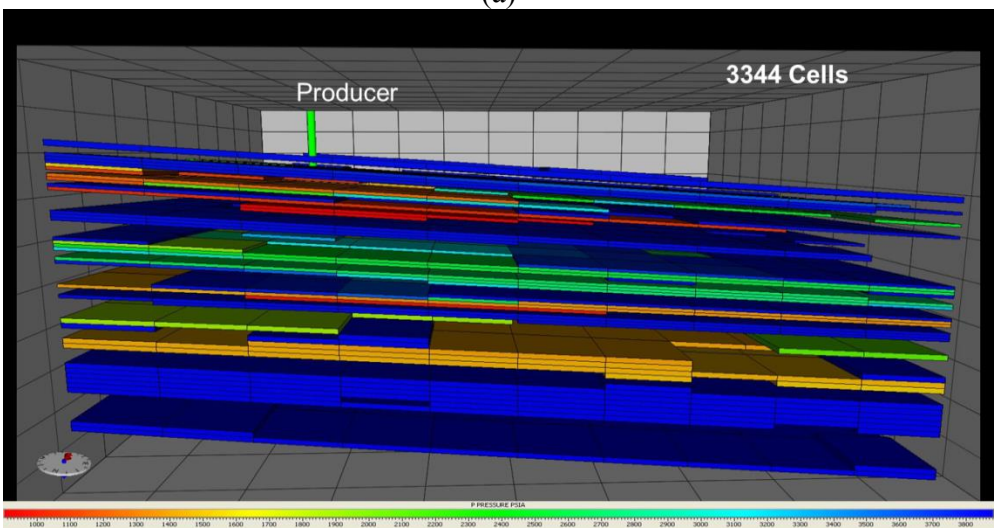

(b)

Figure 2-13: Layer-based coarse models. (a) Optimal statistical layer coarsening with 70 layers. (b) 1x1x5 uniform layer coarsening (75 layers).

1x1 statistical layering can still preserve the heterogeneity contrast between the coarse layers. However, within a layer, the horizontal permeability is too high, as expected, and the horizontal heterogeneity cannot be preserved. The horizontal communication has been overestimated. For uniform layering, we see that the vertical communication has been underestimated, and the horizontal communication has been overestimated, both as expected. Especially for the case of uniform layer coarsening, even for such minimal amounts of upscaling, the depletion pattern of the fine scale model has not been preserved.

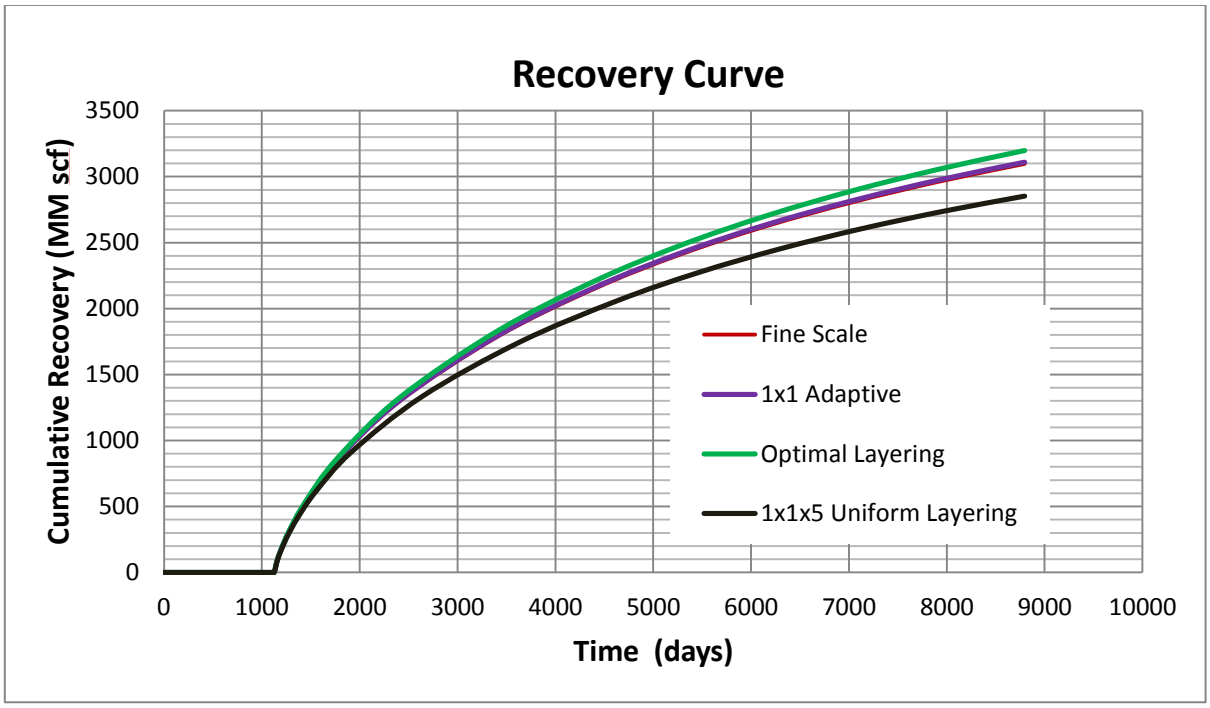

Figure 2-14: Recovery curves of different vertical upscaled models

We apply the transmissibility upscaling and well index upscaling techniques to different upscaled simulation models, and plot the cumulative recovery versus time in Figure 2-14. As a reference, Figure 2-14 also includes the recovery curve of the fine scale geologic model.

The results can be understood as follows. The recovery curve of fine scale geologic model is shown in the red line; it almost overlaps with the purple line, which is the recovery curve of the 1x1xN adaptive upscaled model. This demonstrates that the adaptive upgridding plus the transmissibility and well index upscaling can give us results which are indistinguishable from the fine scale model results. It validates the previous analysis about pressure continuity: 1x1xN adaptive coarsening can guarantee the pressure continuity in each of the simulation grid, thus, will minimize the most important upscaling error.

In contrast, the 1x1 optimal statistical layering is a good estimate, but it slightly over-estimates the recovery. This is not unexpected since it does a reasonable job of preserving the vertical heterogeneity, but will over-estimate the horizontal continuity. The 1x1x5 uniform layering has two competing errors, as show in Figure 2-13b, vertical communication has been underestimated, and the horizontal communication has been overestimated. But underestimation of the vertical communication is the dominant error in this case; therefore, the recovery is under-estimated.

We have also studied a wider range of upscaling calculations to put these results in context. These cases are summarized in Figure 2-15.

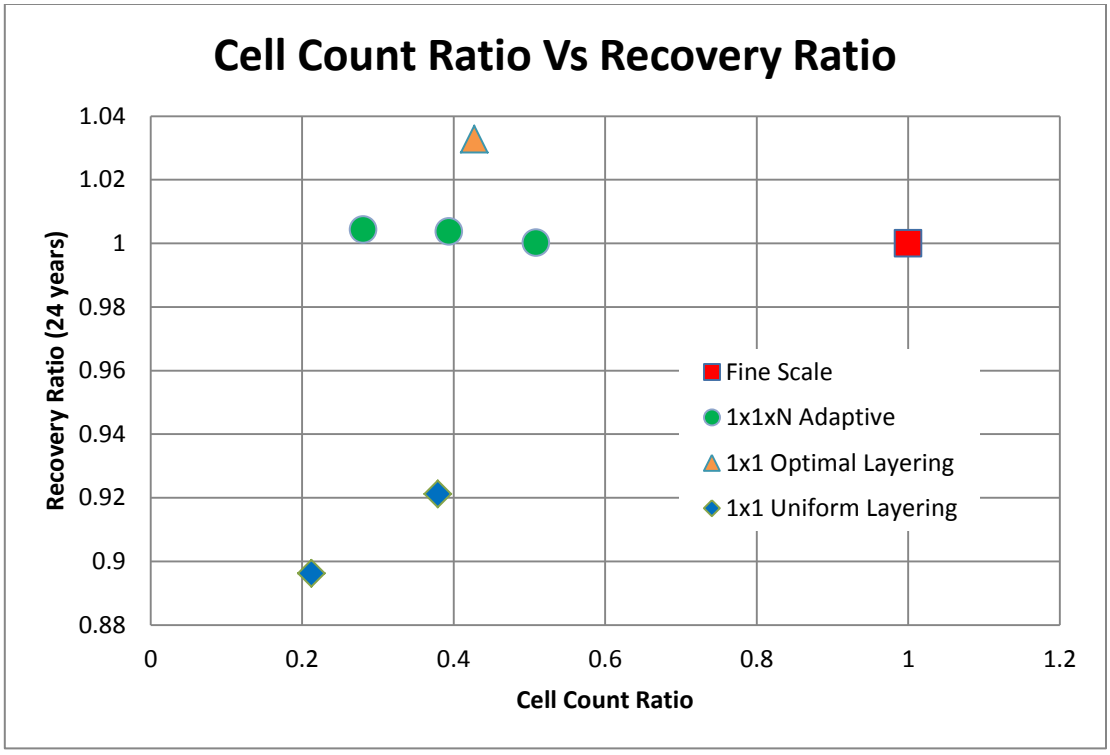

Figure 2-15: Cell count ratio versus sector model recovery ratio for all the 1x1 upgridding cases.

This is a plot of the gas recovered after 24 years of production from the upscaled model compared to the same amount from the fine scale model. The horizontal axis is the ratio of active cells between the same two models. The red square is the fine scale model at a value of (1, 1). The 1x1xN adaptive models, for different values of N, are the three green circles. The left most model has essentially the same recovery as the fine scale model with approximately 25% of the active cells. We can preserve additional reservoir heterogeneity and increase the cell count to approximately 50% and the result does not change. The 1x1 statistically optimal case of 70 layers provides a very good approximation as well. If we further increased the degree of coarsening, we find that the recovery reduces significantly (beyond the range of this plot, which has been discussed before). In other words, even though we are not studying a frontal advance problem, the statistical analysis still does assist in the calculation of a coarse simulation grid. The last

two blue points shown are for 1x1x5 and 1x1x15 uniform coarsening, which would under-estimate recovery.

To better understand each upgridding strategy, we have compared the fine and coarse reservoir pressure at the end of the simulation. We have mapped the final pressure back to the fine scale geologic model, and take the difference between the final pressure calculated from the upscaled model and the final pressure calculated from the fine scale model. The differences in the final pressures provide us with insights about our upgridding strategy.

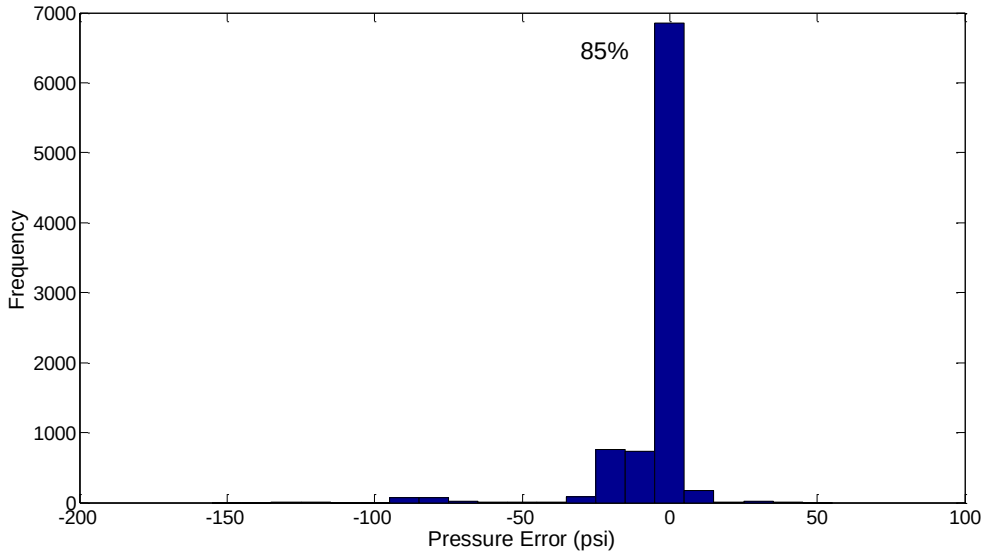

Figure 2-16: Final pressure difference between 1x1xN adaptive upscaled model and reference model (channel facies only).

Figure 2-16 shows the histogram of the final pressure difference between the 1x1xN adaptive upscaled model and the fine scale geologic model. The difference in 85% of the cells is very close to 0, which demonstrates the effectiveness of adaptive upgridding strategy. About 10% of the active cells have a final pressure which is slightly lower than

the fine scale, In other words, the communication among a small fraction of the cells has been overestimated when we merged them.

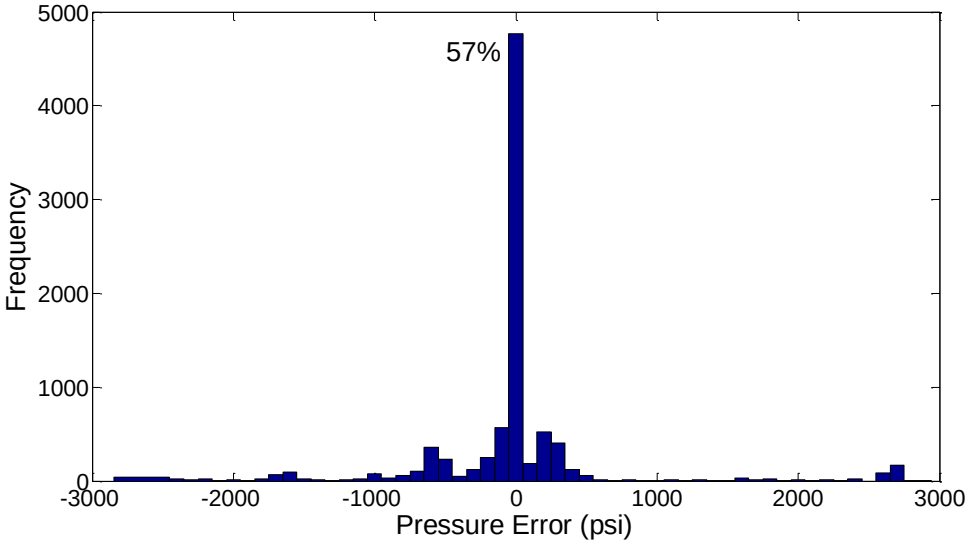

(a)

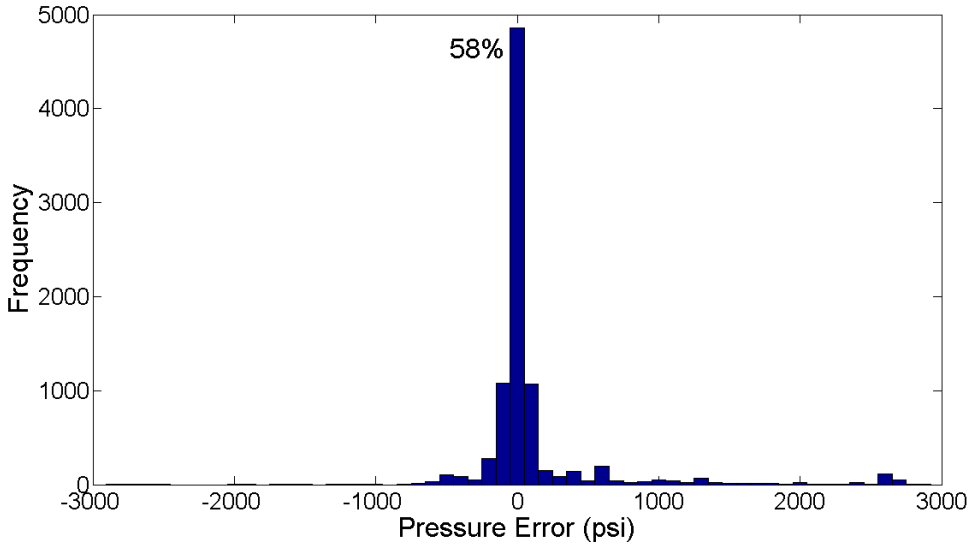

(b)

Figure 2-17: Final pressure error for layer-based coarse models. (a): Final pressure difference between 1x1 optimal layered model and the fine scale model (channel facies only); (b): Final pressure difference between the 1x1x5 uniformly layered model and the fine scale model (channel facies only).

In contrast, Figure 2-17 shows the comparable results corresponding to Figure 2-13. Now the magnitude of the pressure difference is greater than that in Figure 2-16 by about a factor of 20. In both cases, less than 60% of the cells have close to no error. Both distributions show a bump in the distribution with large positive errors. These correspond to cells where the pressure in the fine scale is at essentially initial pressure at the end of the flow simulation. These cells have non-zero porosity, but zero permeability in the original model, and should have been more correctly characterized as non-pay cells. The remaining pressure errors appear to be unbiased for the uniform layering case. However, for the statistical layering case, there are more cells with negative errors, corresponding to increased communication compared to the fine scale.

Finally we examine the scaling of the simulation CPU time for these calculations. Figure 2-18 shows the relationship between the active cell count and CPU time for the 10x10 sector model. All the 1x1 upgridding cases have been included in this plot. Interestingly, there is a close to linear trend for all of the simulation models. According to such linear relationship, if we know how many cells in our upscaled model, we basically can predict how long the simulation run can take. For instance, for our 1x1xN adaptive upgridding, the cell count ratio is 0.28; this upscaled model would probably take about 28% of fine scale model simulation time. This linear trend is not strongly dependent upon the style of upscaling (transmissibility or permeability) or the style of layer design (uniform, statistical, or 1x1xN adaptive). It does scale with the coarse grid active cell count.

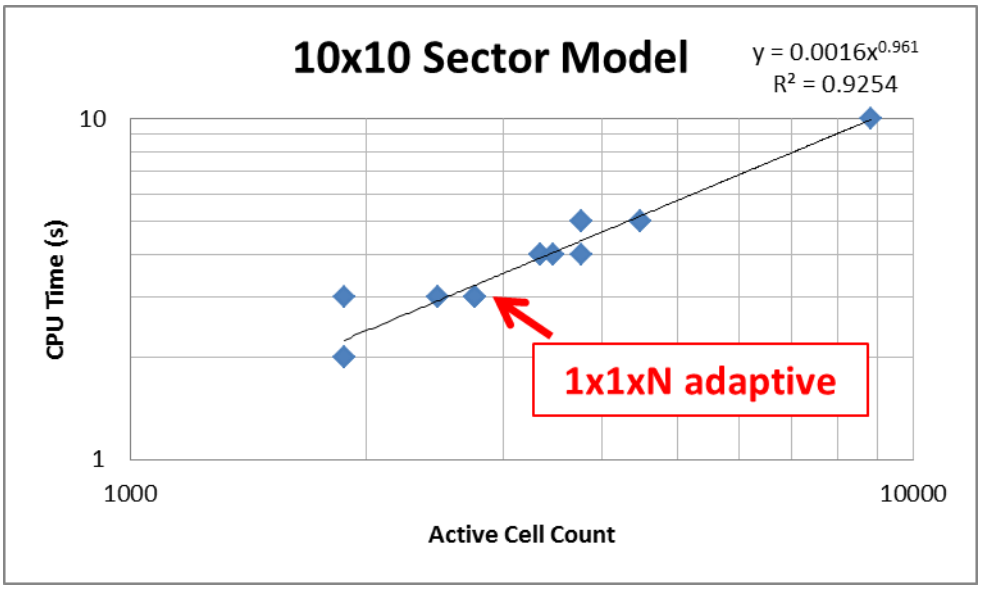

Figure 2-18: CPU time versus cell count for 10x10 sector model (fine scale and vertical coarse models)

2.5.3 Full Field Application

We also apply the same upgridding & upscaling strategies for the full-field model, to ensure scaling to the full field. Similar results could be acquired for the full-field application.

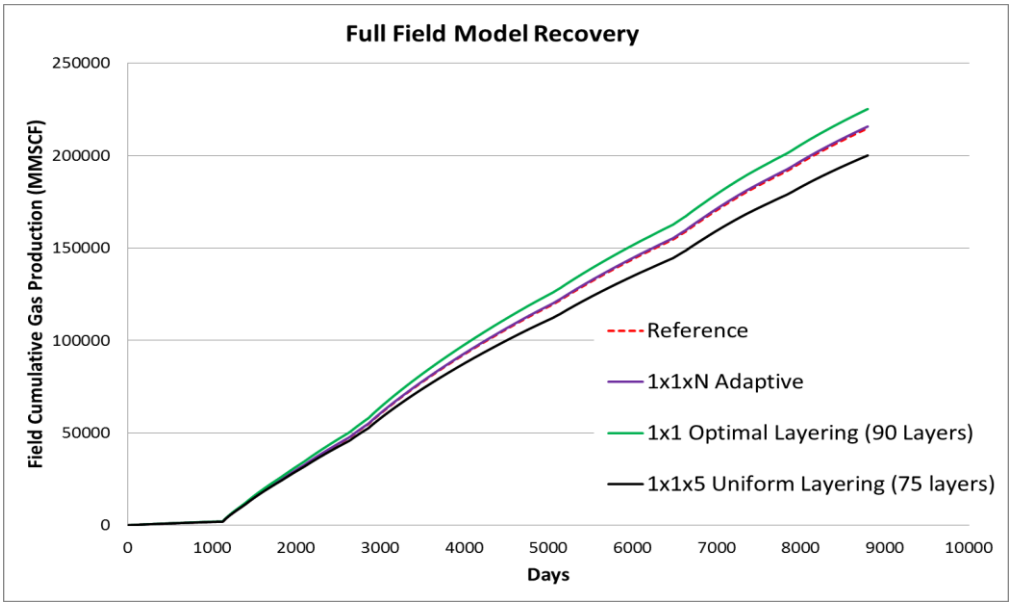

Figure 2-19: Full field recovery curves of different upscaled models (fine scale and vertical coarse models)

Figure 2-19 shows the comparable results corresponding to Figure 2-14, 1x1xN adaptive coarsening provides most accurate result with only about 30% of simulation cells. Similarly, optimal layering overestimates the recovery, and uniform layering still underestimates the recovery.

Figure 2-20 shows the CPU scaling behavior for the full field model. As shown in Figure 2-17, close to linear scaling also occurs in the full field model. Specifically, the full field model simulation time has been reduced from 76 minutes down to 20 minutes, consistent with the reduction in active cell count.

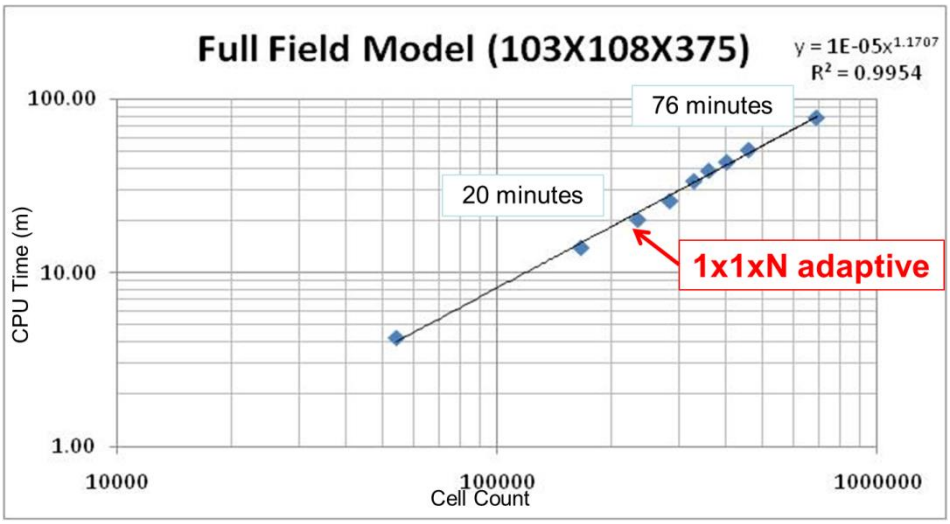

Figure 2-20: CPU time versus cell count for the full field model (fine scale and vertical coarse models)

Unfortunately, a reduction of run time to approximately 30% does not achieve the CPU run time reduction we desire, despite the quality of the upscaling calculation result. As a result we will now explore areal coarsening in addition to vertical coarsening.

2.6 2x2xN Adaptive Upgridding & Upscaling

2.6.1 2x2xN Upgridding & Upscaling Approaches

According to our prior error analysis, 1x1xN coarsening strategy should be the most accurate upgridding and upscaling strategy, however, it may not efficient enough. Because we only merge cells in vertical direction, and the coarsening scale "N" is determined by the thin sand thickness. 1x1xN adaptive coarsening has a cell count ratio of approximately 30% for both the sector model and the full field model. Extension of 1x1xN coarsening could speed-up the CUP time further.

1x1xN vertically adaptive upgridding is designed to make sure that pay and non-pay cells can never be merged together. 2x2xN means areally the cells are merged with a

fixed areal resolution (2x2), and vertically the cells are merged with a flexible resolution. Figure 2-21 shows a comparison of the grid designs for 1x1xN and 2x2xN adaptive upgridding.

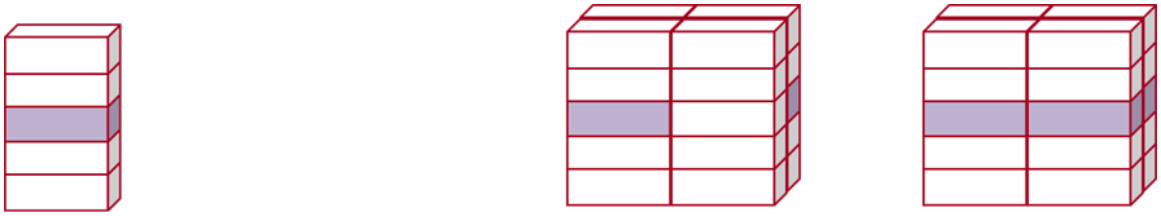

(a) (b)

Figure 2-21: 1x1xN and 2x2xN upgridding strategies. (a) 1x1xN adaptive upgridding cannot merge these cells into one coarse cell. (b) 2x2xN adaptive upgridding, left diagram can merge into one coarse cell, while the right diagram cannot merge into one coarse cell.

For 1x1xN adaptive upgridding, a single barrier or non-pay cell (shaded cell) in the 1x1 column would prevent vertical flow communication. If we wish to be consistent with the requirement of pressure equilibrium within a coarse cell, then these cells will not be merged together. For 2x2xN adaptive upgridding, we will consider both horizontal and vertical flow paths when assessing continuity. In the right diagram in Figure 2-21b, there are sufficient non-pay cells so that there is no vertical communication in any of these four columns. In this case, N would have a maximum value of 2, not 5, as shown. In contrast, the left diagram in Figure 2-21b describes the situation where merging is permissible since the one pay cell in layer three is sufficient to have pressure communication between the top and base of these reservoir layers. However, Note that even they are vertically connected, they may be not horizontally well connected. According to the priori error analysis, there are 30% of pay cells acting as the flow barriers, which should not be merged with the adjacent cells horizontally. Unfortunately, 2x2xN will inevitably merge such barrier cells, therefore, the pressure equilibrium may

not valid in these cells; the upscaling errors should be expected in such coarsening strategy.

Specifically, we will apply a uniform 2x2 areal coarsening on the grid, and then adapt N vertically. N will only be constrained by the layers in which all cells in the upper layer have no communication with the cells in the lower layer, like all four of the permeabilities are non-pay, and so we will be able to achieve larger values for N than for 1x1xN adaptive upgridding.

2x2xN adaptive upscaling is also different with 1x1xN adaptive upscaling. For 1x1xN coarsening, the horizontal flux between different coarse cells is the inter-flux across the adjacent columns. Therefore, upscaled transmissibility is the sum of the harmonic average of the permeabilities, horizontally. The flow based transmissibility calculation is same with the simple algebra calculation, as shown in Figure 2-11b. However, for 2x2xN coarsening, the inter-flux is calculated between different groups of 4 columns, simple algebra calculation no longer works here.

Figure 2-22 shows the 2x2xN adaptive upscaling strategies. Different flow-based transmissibility calculations could be applied in such 2x2xN coarse grid. Here, we utilize the local seal side boundary flow-based transmissibility calculation. There are two variations regarding to the placement of boundary condition: line source and point source. The left diagram shows line source and sink boundary condition. Pressure is assigned as 1 along the central line of the yellow coarse cell, and assigned as 0 along the central line of the green coarse cell, follow this construction, the inter-cell flux, thus, transmissibility could be obtained. It should be the upper estimation of the upscaled transmissibility. Similarly, the right diagrams shows point source and sink boundary condition. Pressure is assigned as 1 at the center of the yellow coarse cell, and assigned as 0 at the center of the green coarse cell, follow this construction, the inter-cell flux, thus, transmissibility could be obtained. It should be the lower estimation of the upscaled

transmissibility. Since these two approaches would give the upper estimation and lower estimation of the upscaled transmissibility. We recommend using the geometric average of the two estimations as the upscaled transmissibility. Later section will show a detailed comparison of this two upscaling methods.

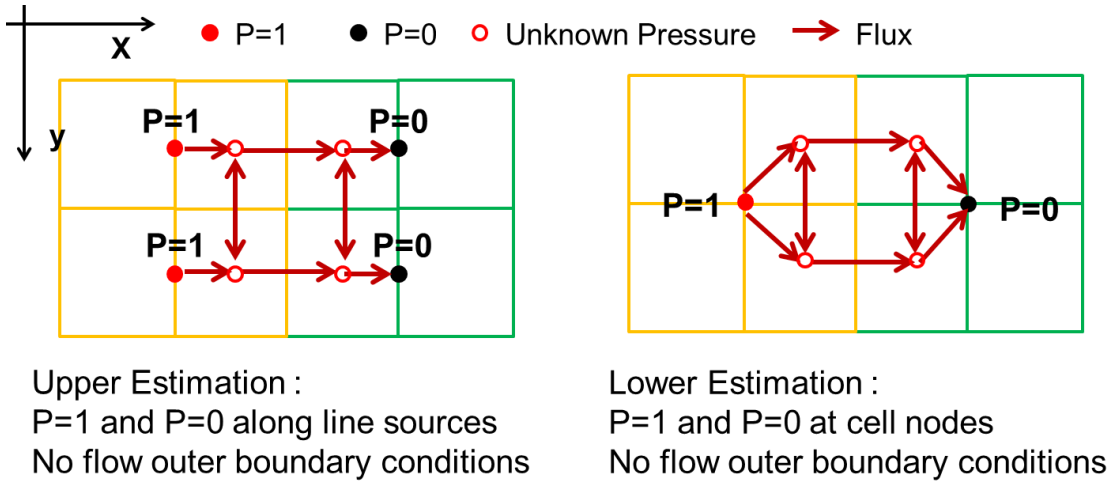

Figure 2-22: 2x2xN local sealed side flow based transmissibility calculations. (a): Line source and sink construction of two coarse cells, which should be our upper estimation estimation of the transmissibility. (b): Point source and sink construction of two coarse cells, which should be our lower estimation estimation of the transmissibility;

2.6.2 2x2xN Upgridding & Upscaling Results

The implementation of 2x2xN adaptive coarsening in Nexus is basically the same with 1x1xN coarsening. We first provide final scale reservoir model to the simulator pre-processor, then replace the fine scale properties with our upscaled properties. The results of the flow simulation are shown in Figure 2-23 for the upscaled sector model. This figure should be contrasted with Figure 2-6 (fine scale model) and Figure 2-12 (1x1xN coarse model).

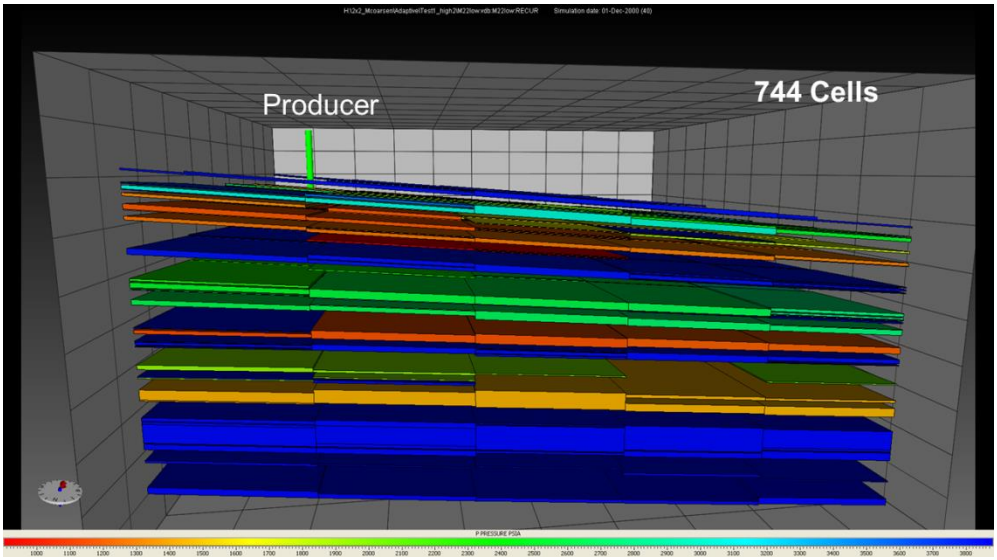

Figure 2-23: 2x2xN adaptive coarse model.

Figure 2-23 shows the final pressures of the 2x2xN upscaled sector model after being depleted for 8796 days. The pressure range is the same with Figure 2-6 and Figure 2-12 for comparison. 2x2xN adaptive grid design has reduced the cell count to 744 active cells and basically preserves the drainage area and isolated volumes. This is despite the reduction in spatial resolution compared to the 1x1xN adaptive upscaled model.

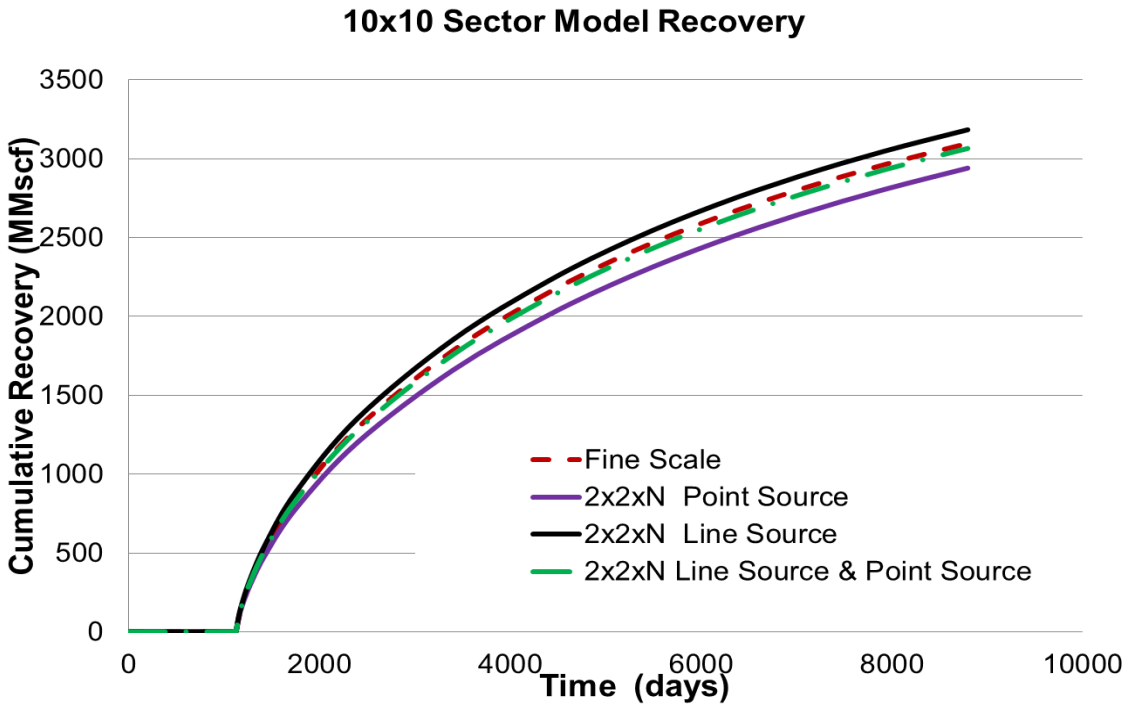

Figure 2-24: Recovery curves of 2x2xN coarse model with different upscaling methods.

The cumulative recovery versus time of 2x2xN coarse model with different transmissibility calculation methods is shown in Figure 2-24. Figure 2-24 also includes the recovery curve of the fine scale geologic model.

All the 2x2xN upscaled models could provide good results, and the error is within 2%. The recovery curve of fine scale geologic model is shown in the red line; Black line shows the line source transmissibility calculation result, as discussed, it serves as the upper estimation of the upscaled transmissibility, thus, overestimates the recovery. In contrast, purple line shows the point source transmissibility calculation result, it serves as the lower estimation of the upscaled transmissibility, both has about 1~2% error, in terms of the final recovery. A geometric average of the upper estimation and lower estimation of the transmissibility should prove more accurate results, as the green line. It also overlaps with the fine scale recovery curve. Figure 2-24 also shows the influence of

different upscaling methods based on the same grid. Here, we recommend using the geometric average of line source and point source transmissibility calculation for the 2x2xN coarse model upscaling method.

We add 3 more upscaled models in the cell count ration vs. recovery ratio plot in Figure 15, as shown in Figure 2-25.

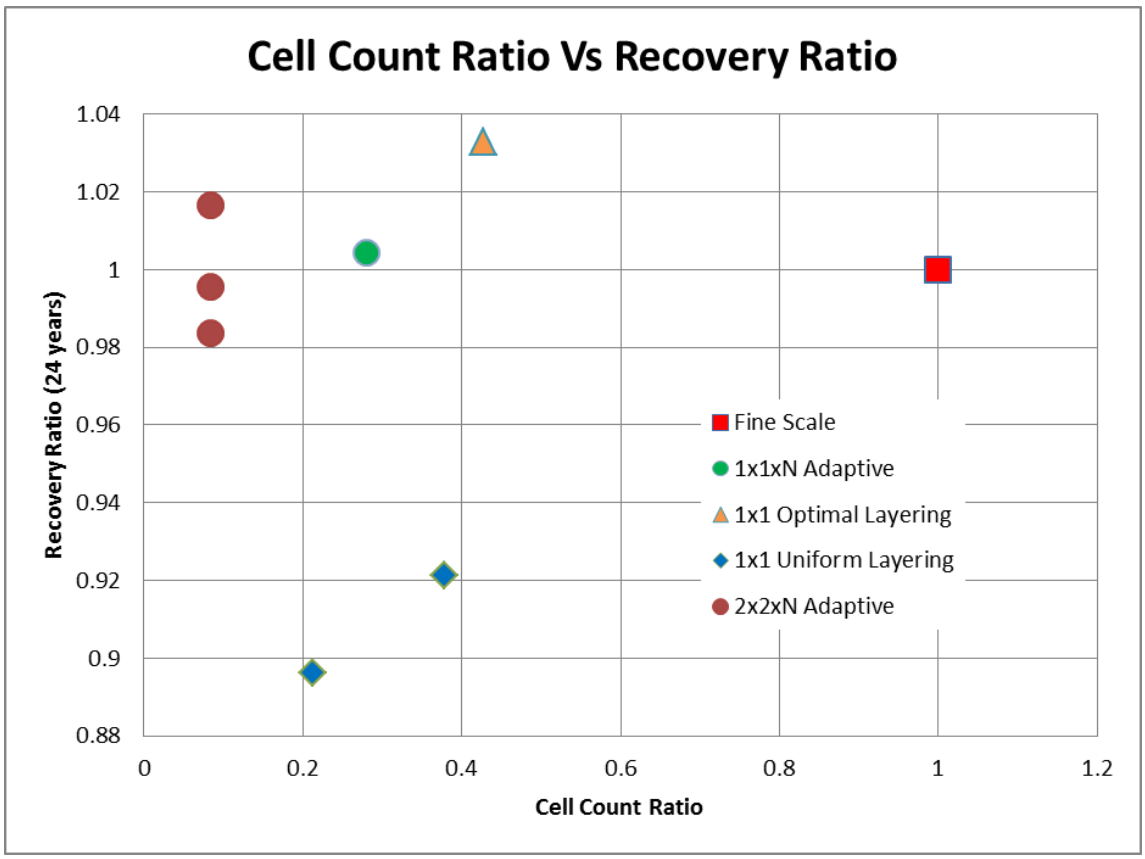

Figure 2-25: Cell count ratio versus sector model recovery ratio (fine scale and 1x1, 2x2 coarse models).

The axis is still the same with Figure 2-15, horizontal axis is the ratio of active cells between the two models. Red square is the fine scale model. And 1x1xN is the green

point, which is the most accurate coarse model. Still, Figure 2-25 also shows the optimal statistical layered model (orange triangle point) and uniform layered model (blue points), which are discussed in Figure 2-15. Besides that, 3 maroon points are shown in the left, which are the 2x2xN coarse model with different upscaling methods. Upper point is the line source upscaling method, and lower point is the point source upscaling method. The middle one is the geometric average of these two methods, which also provides accurate result, with less than 10% of the cell count ratio.

Similarly, we also plot the differences in the final pressures of the coarse model and fine scale model. Note that here we show the coarse model with our recommend upscaling method.

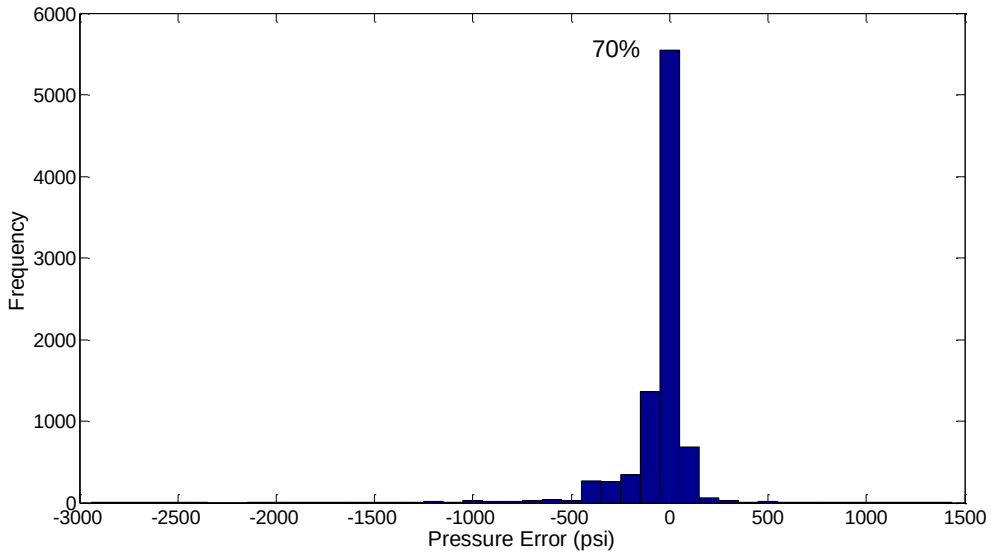

Figure 2-26: Final pressure difference between 2x2xN adaptive upscaled model and reference model (channel facies only).

Figure 2-26 shows the histogram of the final pressure difference between the 2x2xN adaptive upscaled model and the fine scale geologic model. This figure should be

contrasted with Figure 2-16 (1x1xN coarsening) and Figure 2-17 (layer-based coarsening). Here, the difference in 70% of the cells is very close to 0. Figure 2-16 shows pressure difference of 85% of the cells is close to 0 for 1x1xN coarse model, and Figure 2-17 shows pressure difference of about 58% of the cells is close to 0 for layer-based coarse model.

Still, 2x2xN adaptive coarsening performs much better, compared to 1x1 layer-based coarsening. But in terms of accuracy, it is not as accurate as 1x1xN adaptive coarsening. As discussed before, there are 30% of pay cells acting as the flow barriers horizontally. 1x1xN adaptive coarsening can accurately preserve such barriers, however, 2x2xN adaptive coarsening may not preserve these horizontal barriers during the 2x2 areal coarsening.

Again, we re-examine the scaling of the simulation CPU time for these calculations. Figure 2-27 shows the relationship between the active cell count and CPU time for the 10x10 sector model and more upscaled models are taken into account, compared to Figure 2-18. All the 1x1 and 2x2 upgridding cases have been included in this plot. The linear trend still exists here. 1x1xN adaptive coarse model could provide CPU speed-up x 3.5, with the most accurate results. While 2x2xN adaptive coarse model could provide CPU speed-up x10, with slightly less accurate results.

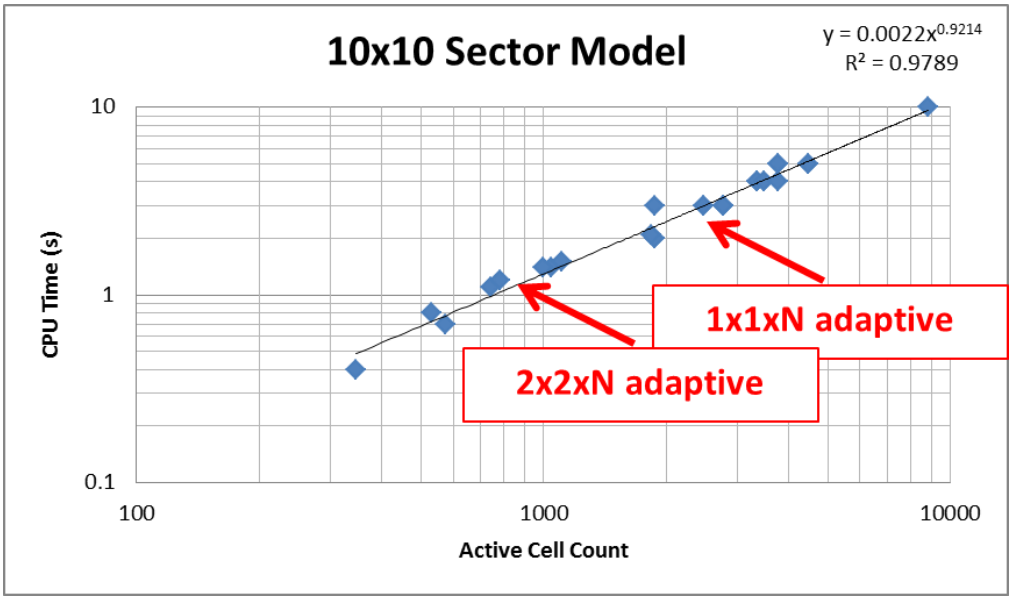

Figure 2-27: CPU time versus cell count for 10x10 sector model (fine scale and 1x1, 2x2 coarse models).

2.6.3 Full Field Application

We also apply the same upgridding & upscaling strategies for the full-field model, to ensure scaling to the full field. Similar results could be acquired for the full-field application.

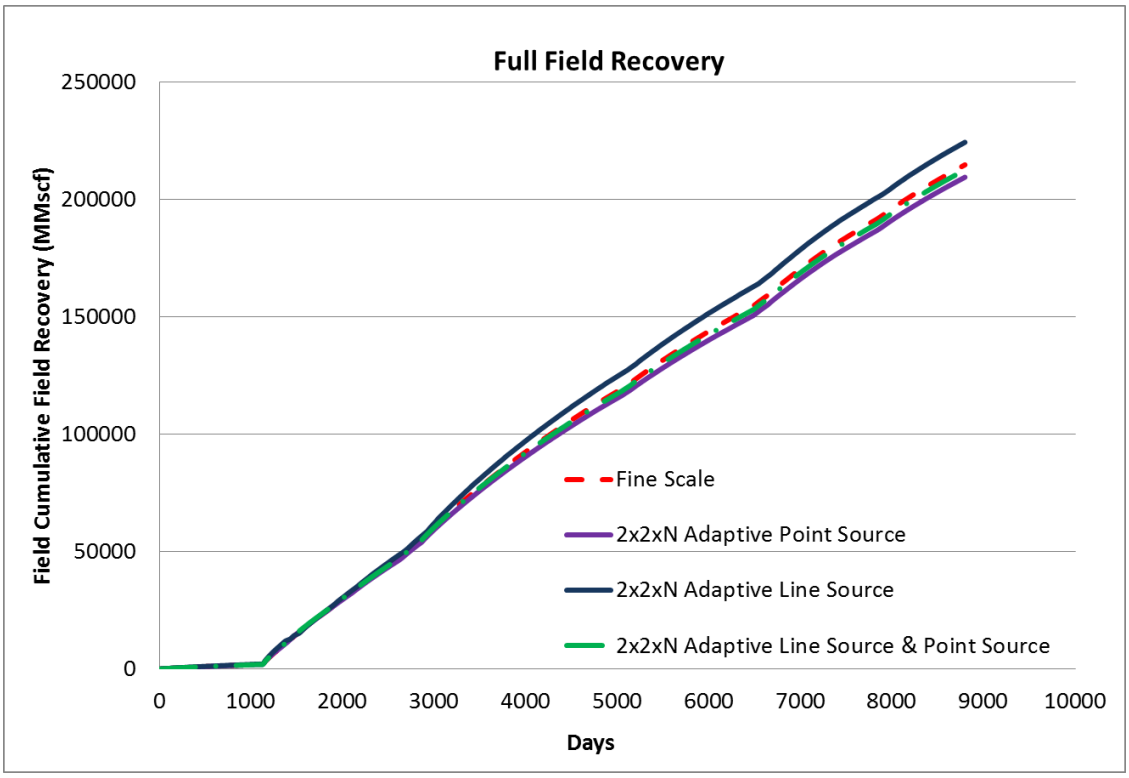

Figure 2-28: Full field recovery curves of 2x2xN coarse models

Figure 2-28 shows the comparable results corresponding to Figure 2-24, the combination of line source and point source transmissibility upscaling could produce more accurate results, compared to either of them.

Figure 2-29 shows the CPU scaling behavior for the full field model. As shown in previous figures, close to linear scaling also occurs in the full field model. Specifically, the full field model simulation time has been reduced from 76 minutes down to 20 minutes for 1x1xN coarse model, and further down to 6.5 minutes for 2x2xN coarse model.

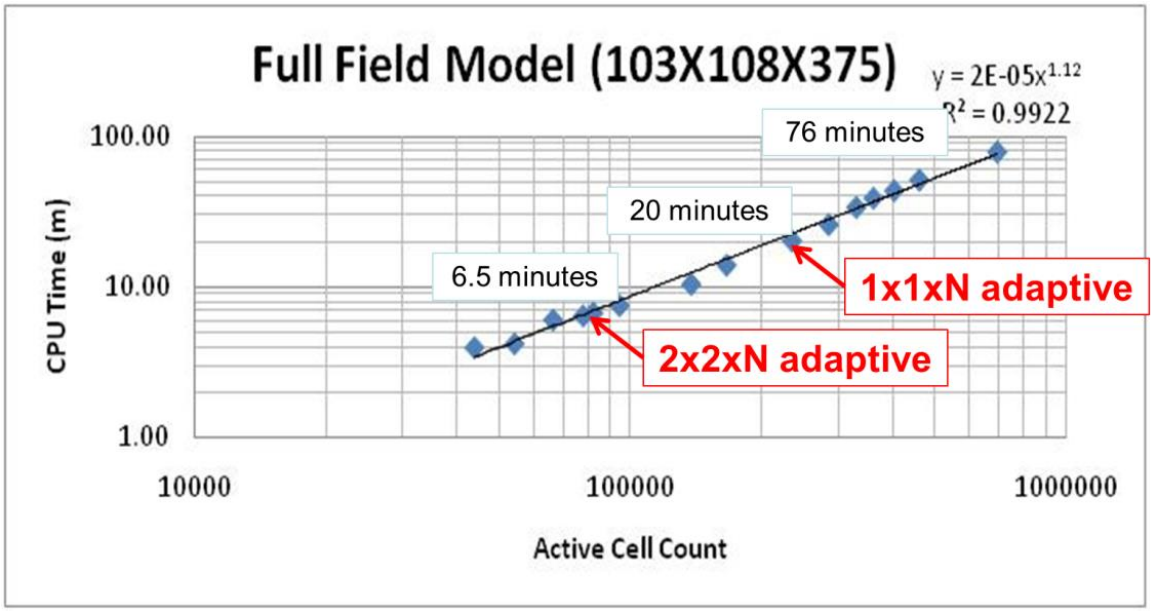

Figure 2-29: CPU time versus cell count for the full field model (fine scale and 1x1, 2x2 coarse models).

1x1xN adaptive coarse model has CPU speed-up x 3.5, with most accurate results. While 2x2xN adaptive coarse model could provide CPU speed-up x10, with slightly less accurate results. Next section will further extend the techniques we had shown to 3x3xN adaptive coarsening.

2.7 3x3xN Adaptive Upgridding & Upscaling

2.7.1 3x3xN Upgridding & Upscaling Approaches

1x1xN vertically adaptive upgridding is designed to make sure that pay and non-pay cells can never be merged together. 2x2xN means areally the cells are merged with a fixed resolution (2x2), and vertically the cells are merged with a flexible resolution. Based on the same concept, we can continue to design the 3x3xN adaptive coarsening. 3x3xN will consider 9 columns as one individual group, and merging is permissible

when the top and base of these reservoir layers have sufficient pressure continuity, similar to 2x2xN case.

Specifically, we will apply a uniform 3x3 areal coarsening on the grid, and then adapt N vertically. N will only be constrained by the layers in which the cells in the upper layer have no communication with the cells in the lower layer.

Due to the wider coarsening region horizontally, we can achieve a larger CPU speed-up factor. However, we recognized there are 30% of pay cells acting as the flow barriers in the priori error analysis. 3x3xN coarsening has a greater chance to merge such barrier cells, compared to 2x2xN coarsening. Therefore, we should expect greater upscaling errors here.

Similar to 2x2xN transmissibility upscaling, 3x3xN upscaling also requires flow based transmissibility calculation. Figure 2-30 shows the 3x3xN adaptive upscaling strategies. Here, we utilize the local seal side boundary flow-based transmissibility calculation. There are two variations regarding to the placement of boundary condition: line source and point source. The left diagram shows line source and sink boundary condition. Pressure is assigned as 1 along the central line of the yellow coarse cell, and assigned as 0 along the central line of the green coarse cell, follow this construction, the inter-cell flux, thus, transmissibility could be obtained. It should be the upper estimation of the upscaled transmissibility. Similarly, the right diagrams shows point source and sink boundary condition. Pressure is assigned as 1 at the center of the yellow coarse cell, and assigned as 0 at the center of the green coarse cell, follow this construction, the inter-cell flux, thus, transmissibility could be obtained. It should be the lower estimation of the upscaled transmissibility. Here, we also recommend using the geometric average of the two estimations as the upscaled transmissibility.

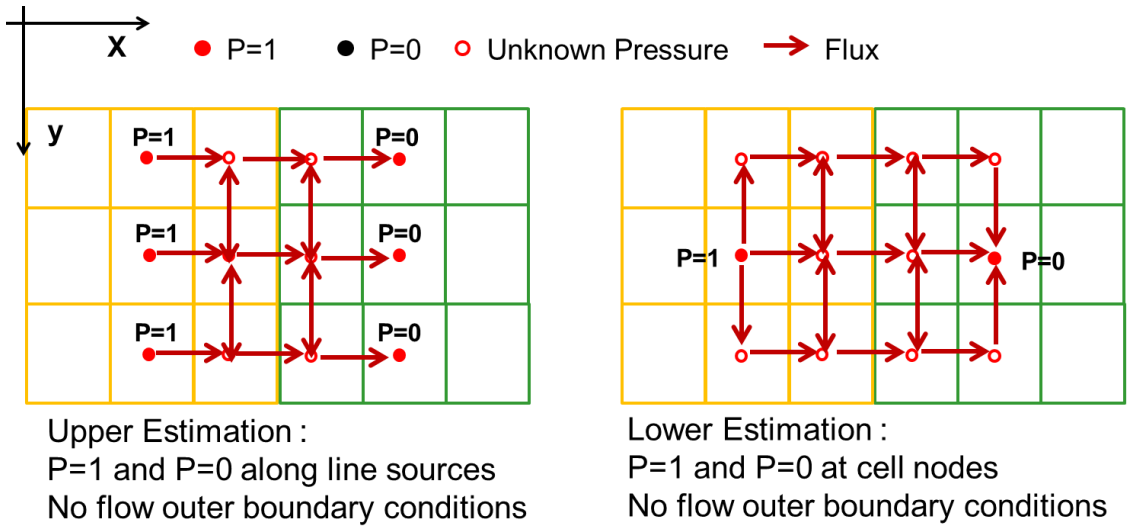

Figure 2-30: 3x3xN local sealed side flow based transmissibility calculations. Left diagram shows the line source and sink construction of two coarse cells, which should be our upper estimation of the transmissibility. Right diagram shows the point source and sink construction of two coarse cells, which should be our lower estimation of the transmissibility.

Note that the difference between 2x2xN and 3x3xN is that later one would place pressure boundary at the center of fine cells, instead of edges for point source construction. It is quite possible that the source/sink is in the non-pay cell, which could generate zero transmissibility. We can predict point source of 3x3xN should give us much lower recovery.

2.7.2 3x3xN Upgridding & Upscaling Results

The results of the flow simulation are shown in Figure 2-31 for the 3x3xN upscaled sector model. This figure should be contrasted with Figure 2-6 (fine scale model), Figure 2-12 (1x1xN coarse model), and Figure 2-23 (2x2xN coarse model).

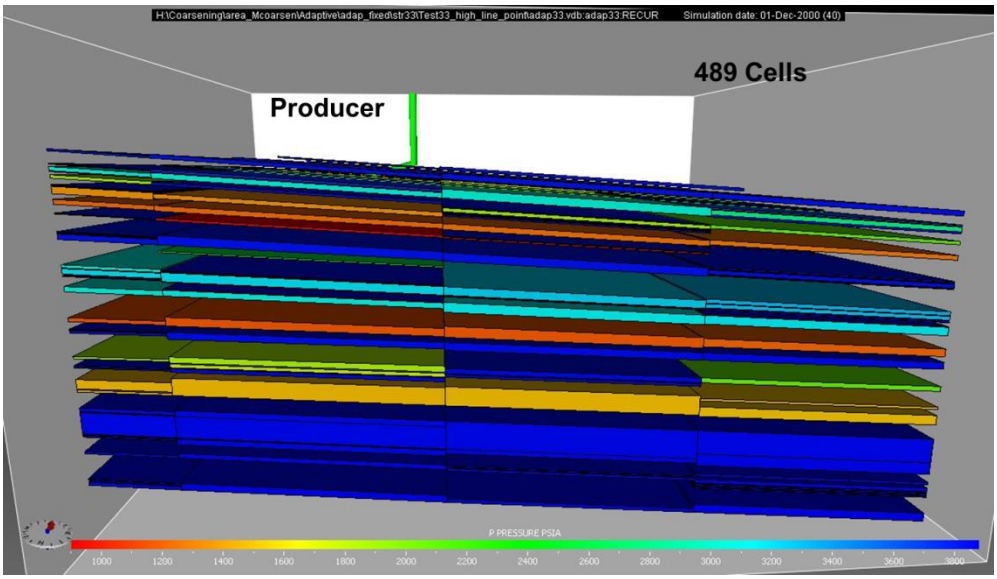

Figure 2-31: 3x3xN adaptive coarse model.

Figure 2-31 shows the final pressures of the 3x3xN upscaled sector model after being depleted for 8796 days. The pressure range is the same with Figure 2-6, 2-12, 2-23 for comparison. 3x3xN adaptive grid design has reduced the cell count to 489 active cells. Despite the reduction in spatial resolution compared to the 1x1xN, and 2x2xN adaptive upscaled model, and 3x3xN adaptive upscaled model basically preserves the drainage area and isolated volumes. Please note that at the boundary of this sector model, 1x3xN, or 3x1xN adaptive coarsening is applied.

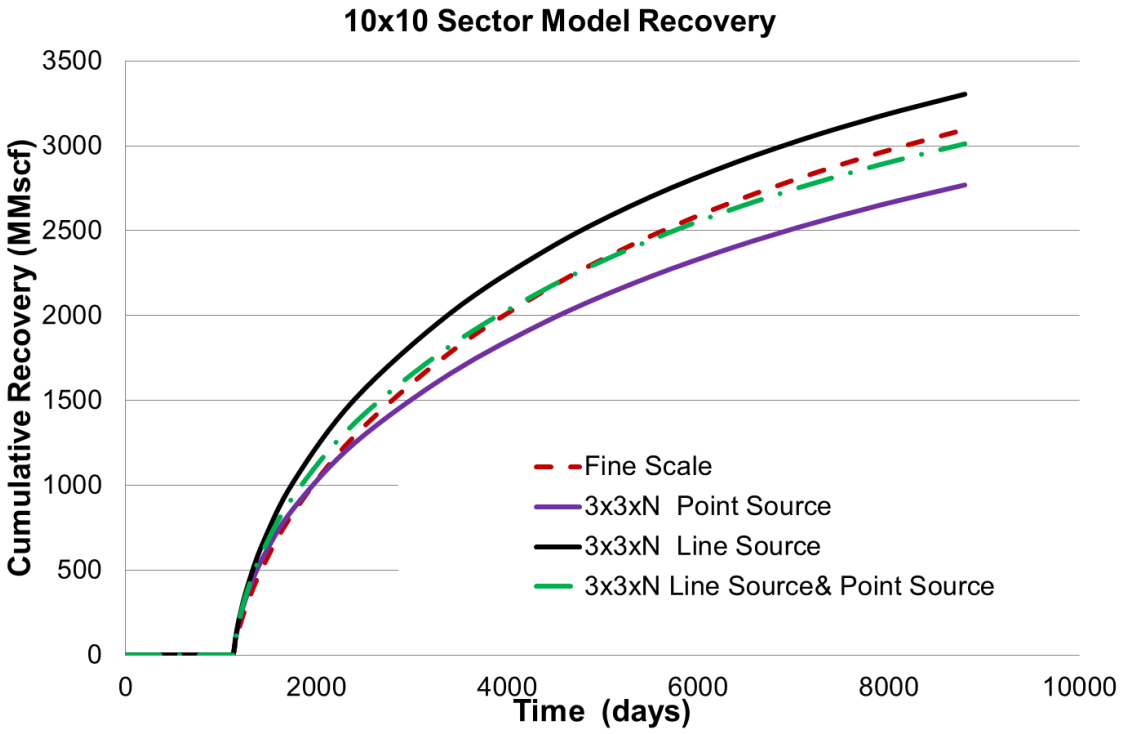

Figure 2-32: Recovery curves of 3x3xN coarse model with different upscaling methods.

The cumulative recovery versus time of 3x3xN coarse model with different transmissibility calculation methods is shown in Figure 2-32. Figure 2-32 also includes the recovery curve of the fine scale geologic model.

The recovery curve of fine scale geologic model is shown in the red line; Black line shows the line source transmissibility calculation result, as discussed, it serves as the upper estimation of the upscaled transmissibility, thus, overestimates the recovery. In contrast, purple line shows the point source transmissibility calculation result, it serves as the lower estimation of the upscaled transmissibility. Line source approximation would have 4% error, while point source has about 6% error, in terms of final recovery. Point source produces a large error since the source/sink maybe located at the non-pay cell, as discussed before.

A geometric average of the upper estimation and lower estimation of the transmissibility should prove more accurate results, as the green line. It has about 3% errors, but with the CPU speed-up x 20. Due to its efficiency, 3x3xN coarsening also provides a good option for the upgridding & upscaling in tight gas reservoirs.

3 more upscaled models could be added in the cell count ration vs. recovery ratio plot in Figure 2-15, as shown in Figure 2-33.

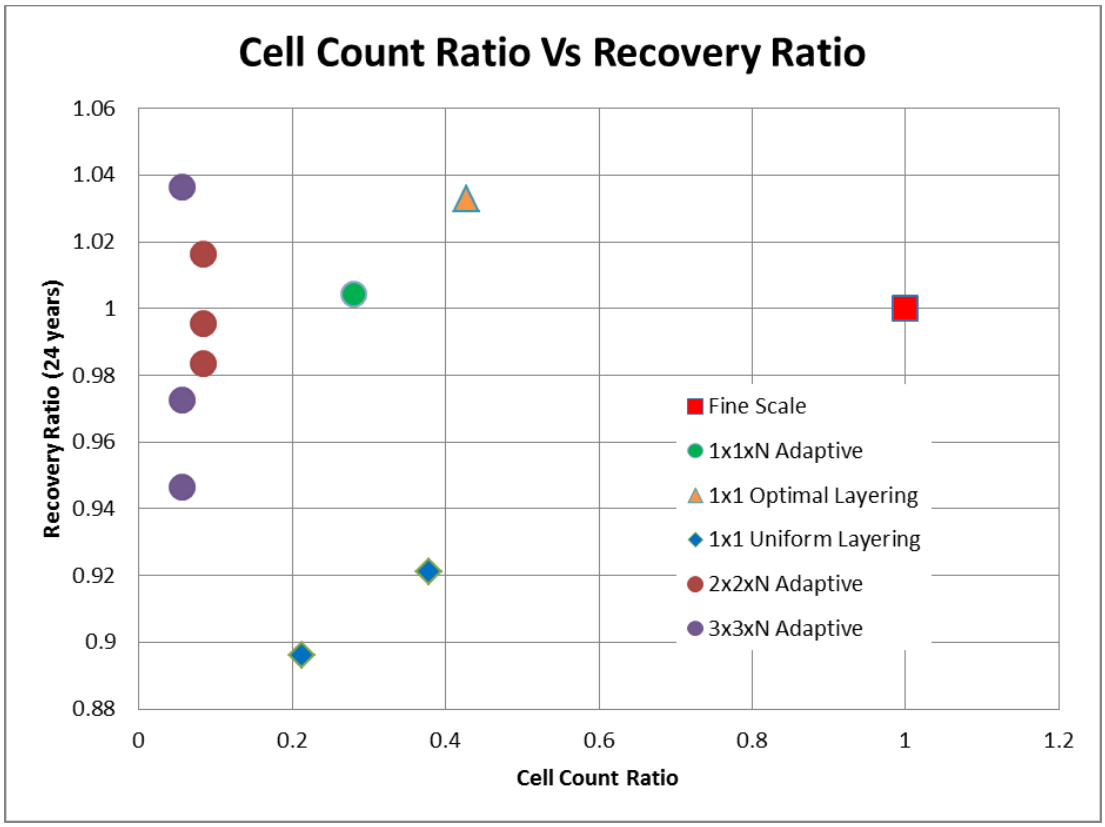

Figure 2-33: Cell count ratio versus sector model recovery ratio (fine scale and 1x1, 2x2, 3x3 coarse models).

The axis are still the same with Figure 2-15, 2-25, horizontal axis is the ratio of active cells between the two models. Red square is the fine scale model. And 1x1xN is the green point, which is most accurate coarse model. 2x2xN adaptive upscaled models are 3 maroon points. And 3 more purple points in the left most are the 3x3xN adaptive upscaled models. Upper point is the line source upscaling method, and lower point is the point source upscaling method. The middle one is the geometric average of these two methods, which also provides accurate result, with about 5% of the cell count ratio.

Similarly, we also plot the differences in the final pressures of the coarse model and fine scale model. Note that here we show the coarse model with our recommend upscaling method.

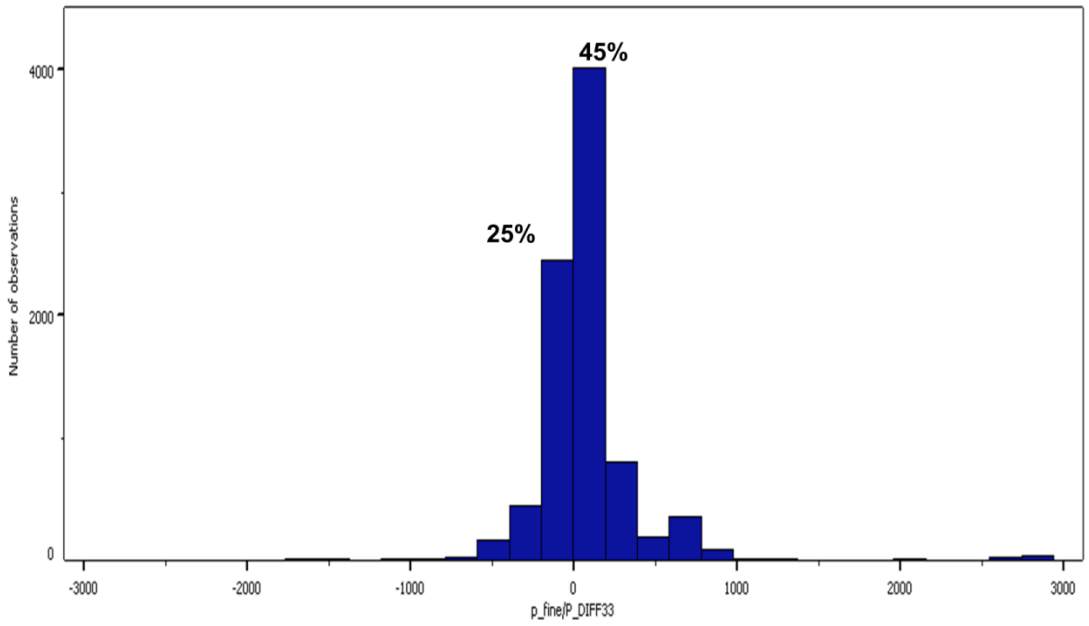

Figure 2-34: Final pressure difference between 3x3xN adaptive upscaled model and reference model (channel facies only).

Figure 2-34 shows the histogram of the final pressure difference between the 3x3xN adaptive upscaled model and the fine scale geologic model. This figure should be contrasted with Figure 2-16 (1x1xN coarsening) and Figure 2-26 (2x2xN coarsening). Here, pressure error of 45% of cells is in the region of 0~150 psi, and 25% of cells is in the region of -150~0 psi. In total, 70% of cells pressure error is within 150 psi, which is relatively larger than 2x2xN adaptive case. More positive pressure errors means we might underestimates some of the internal communications, which can be proved in the recovery curve.

Again, we re-examine the scaling of the simulation CPU time for these calculations. Figure 2-35 shows the relationship between the active cell count and CPU time for the 10x10 sector model, and more upscaled models are taken into account, compared to Figure 2-18, 2-27. All the 1x1, 2x2, 3x3 upgridding cases have been included in this plot. The linear trend still exists here. 1x1xN adaptive coarse model could provide CPU speed-up x 3.5, with most accurate results. 2x2xN adaptive coarse model could provide CPU speed-up x 10, with slightly less accurate results. 3x3xN adaptive coarse model could provide CPU speed-up x 20, with a relatively large error.

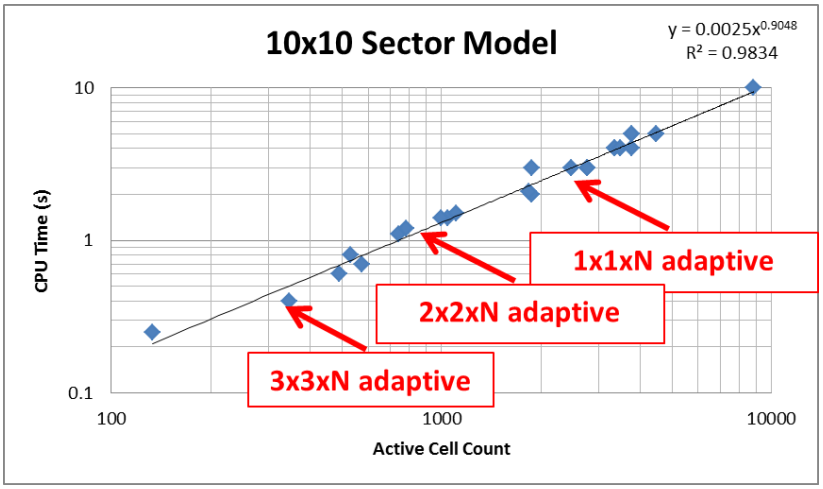

Figure 2-35: CPU time versus cell count for 10x10 sector model (fine scale and 1x1, 2x2, 3x3 coarse models).

2.7.3 Full Field Application

We also apply the same upgridding & upscaling strategies for the full-field model, to ensure scaling to the full field. Similar results could be acquired for the full-field application.

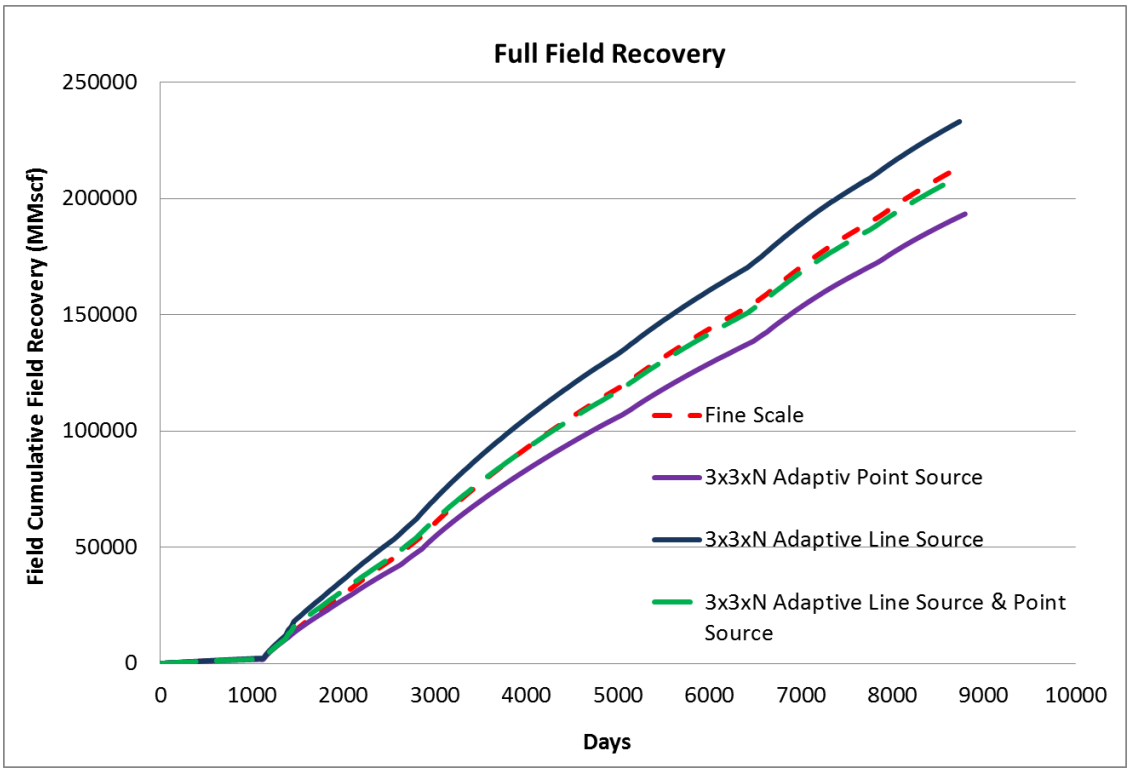

Figure 2-36: Full field recovery curves of 3x3xN coarse models

Figure 2-36 shows the comparable results corresponding to Figure 2-24, 2-28, the combination of line source and point source transmissibility upscaling could produce more accurate results, compared to either of them.

Figure 2-37 shows the CPU scaling behavior for the full field model. As shown in previous figures, close to linear scaling also occurs in the full field model. Specifically,

the full field model simulation time has been reduced from 76 minutes down to 20 minutes for 1x1xN coarse model, 6.5 minutes for 2x2xN coarse model, and 3 minutes for 3x3xN coarse model.

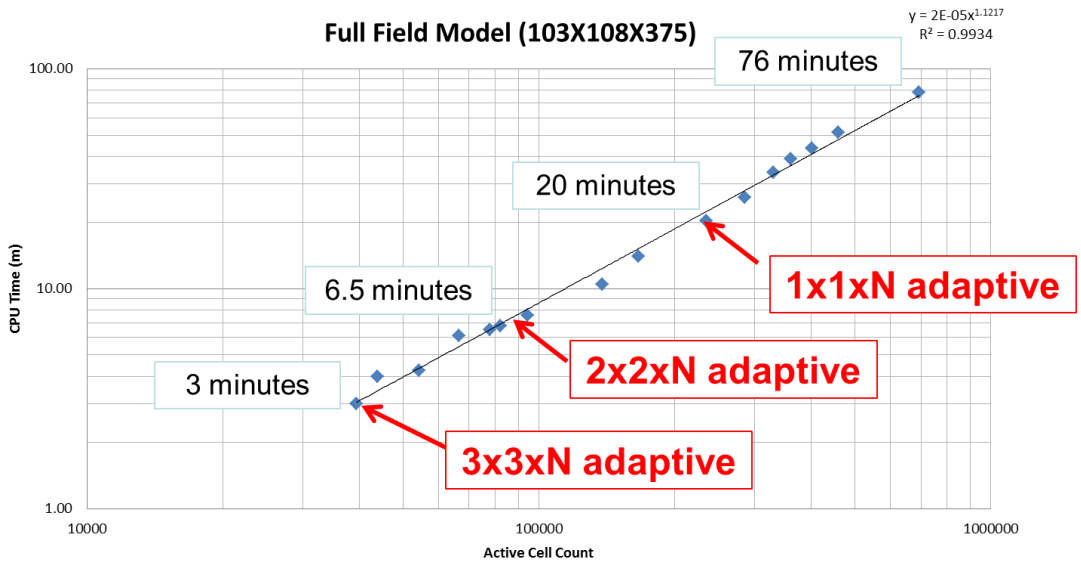

Figure 2-37: CPU time versus cell count for the full field model (fine scale and 1x1, 2x2, 3x3 coarse models).

The objective for adaptive coarsening is to design the coarse model that can get at least one-order magnitude simulation speed-up. 3x3xN should be good enough for this objective. However, we can still move on to 4x4, or 5x5 with the same procedures.

2.8 3D Adaptive Upgridding & Upscaling

2.8.1 3D Adaptive Upgridding & Upscaling Approaches

All the adaptive coarsening strategies we discussed before are designed with a fixed areal resolution and flexible vertical resolution. Such adaptive coarsening strategies, including 1x1xN, 2x2xN, 3x3xN, are designed to preserve the coarse grid corner point

geometry. However, 2x2xN and 3x3xN may sacrifice the accuracy in order to keep this geometry. As discussed earlier, there are 30% of horizontal baffles may introduce the upscaling errors if we include them in one coarse cell. 2x2xN and 3x3xN could preserve the pressure connectivity in vertical direction, but not in horizontal direction, which is proved in the previous sections.

In order to design the coarse grid which can preserve the pressure connectivity both in vertical & horizontal direction, a combination of vertical & horizontal adaptive grid could be utilized based on the same concept of depth of investigation and diffusive time of flight. Our work also tries to design the 3D adaptive upgridding and upscaling strategies to achieve this objective.

The diffusive time, mentioned above, actually represents the pressure wave propagate time across a single cell in certain direction. In this section, we utilize the accumulative diffusive time, which calculates the pressure wave propagate time, starting from every perforation/well to the center of each cell. Fast Marching Method (Xie et al., 2012) could be utilized to simulate the pressure wave propagation.

The upgridding strategy is to merge the cells within certain diffusive time region, the pressure connectivity could be preserved in each coarse cell. However, an issue about cell geometry would arise with such adaptive or unstructured grids. Since the grids are designed to preserve the internal connectivity, we could have some bizarre geometry for the coarse grid, like “L” or “U” shape grid. The upscaling strategies based on such adaptive or unstructured grids is still an open question, we proposed several strategies for such grids, which can be categorized as point source transmissibility calculation and diffusive source transmissibility calculation. Figure 2-38 shows these two transmissibility calculation methods.

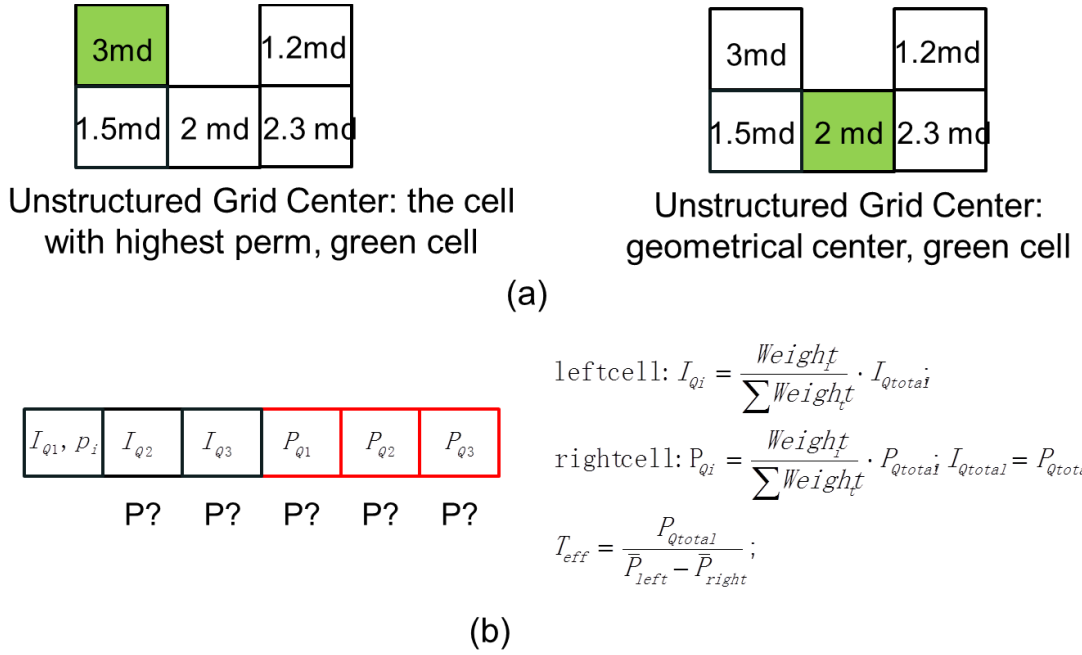

Figure 2-38: Unstructured transmissibility upscaling methods. (a): Point source transmissibility upscaling. The source are chosen at the highest perm cell (left) or geometrical center (right); (b) Diffusive source transmissibility upscaling. Instead of assigning the pressure, the flux is assigned for each cell of the coarse model based on the weights, which could be perm, or pore volume, etc.

Point source transmissibility calculation, as discussed in Figure 2-22, 2-30, pressure is assigned as 1 at one particular location of the coarse cell, and assigned as 0 at one particular location of another coarse cell. However, the tricky part is how to determine the location of the pressure source and sink. Two possible options are shown in Figure 2-38a, left diagram shows that the pressure source and sink could be chosen at the cell which has the highest permeability, while the right diagram shows that the pressure source and sink could be chosen at the geometrical center of the coarse grid, if there is any. Note that for this point source upscaling, the upscaled transmissibility may not be the lower estimation of the actual transmissibility. For example, if we pick the highest permeability cell as the pressure source or sink, we might overestimate the intercell transmissibility, since both the source and sink are located at the cells with have good flow capacity.

The limitation of the point source transmissibility upscaling is that the results are very sensitive to the pressure source and sink locations. But the advantage of this method is that it is very easy to implement.

Diffusive source transmissibility calculation is shown in Figure 2-38b. Consider we merge the left 3 black cells as one coarse cell, and right 3 red cells as another coarse cell, and then we need to calculate the transmissibility. Here, instead of specifying the pressure at certain location/ cell, we specify the flux at each coarse cell. Assuming we place one pseudo well at each of the fine cells, 3 injection wells in the black cells, and 3 production wells in the red cells, the injection/ production flux is distributed according to each cell's weight. The weight could be pore volume, permeability, or other property. With the known flux of each cell, pressure could be obtained. The upscaled transmissibility would be the total flux divided by the average pressure difference, as the equation shows.

Diffusive source transmissibility calculation is not sensitive to the coarse cell geometry, since it does not require the information of the boundary location. But it is sensitive to how the flux is distributed in each cell, specifically, how to choose the weight.

2.8.2 3D Upgridding & Upscaling Results

As discussed, accumulative diffusive time which calculates the pressure wave propagates time, starting from every perforation/well to the center of each cell is obtained through the Fast Marching Method. The adaptive upgridding strategy is to merge the cells within certain diffusive time region, the pressure connectivity could be preserved in each coarse cells. Figure 2-39 shows the snapshots of pressure propagation in the sector model.

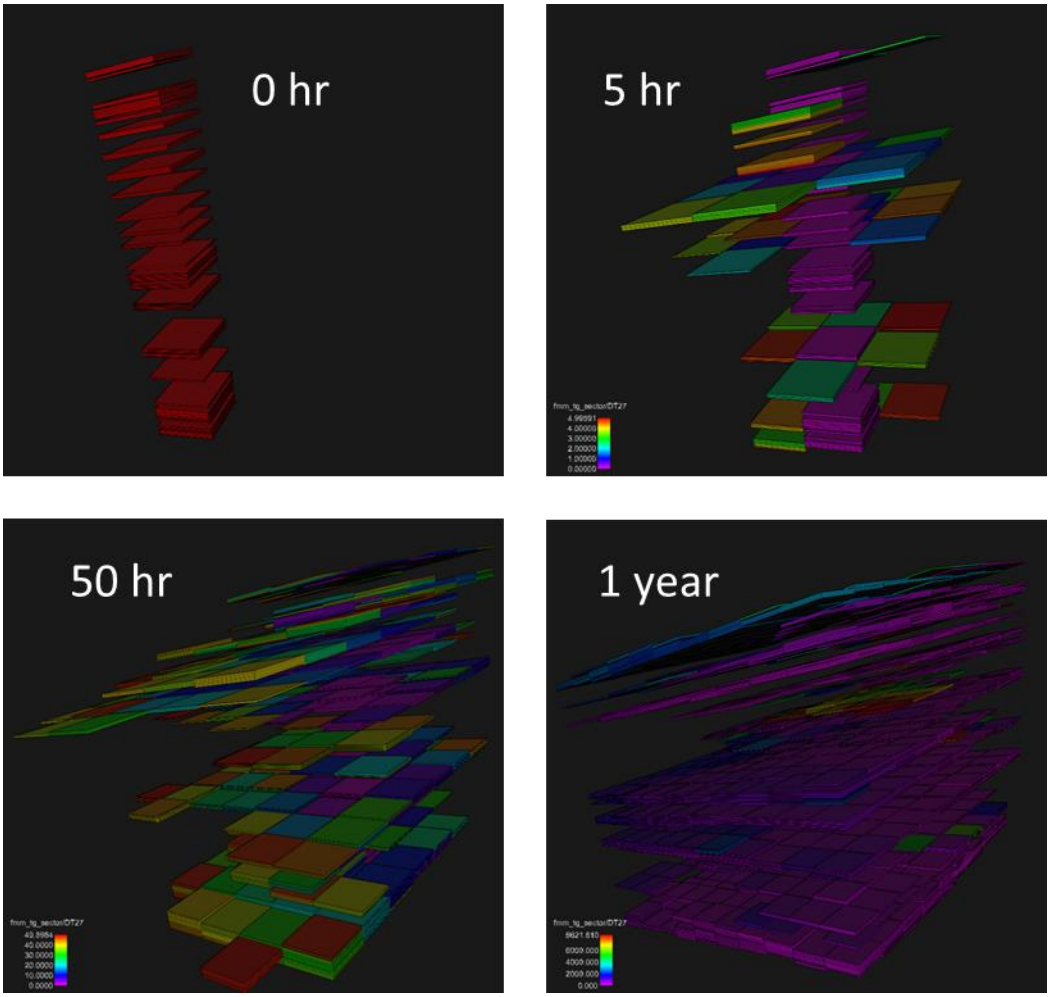

Figure 2-39: Snapshots of pressure propagation in the sector model.

The cutoff time is 0 hr, 5 hr, 50 hr, and 1 year, in Figure 2-39. At 0 hr, the pressure propagation or pressure impulse starts from every perforation, after that, the pressure propagates across the sector model. Pressure propagates mainly in vertical direction at early time, then in both vertical and horizontal direction at late time, which is consistent with our previous analysis.

3D adaptive coarsening is designed to merge the cells within certain diffusive time region. Properly choosing the time region is crucial for the upgridding design, the basic

idea to make sure the pressure continuity within each region. Figure 2-40 shows an example of the 3D adaptive coarse model, by choosing the time threshold as 1 month.

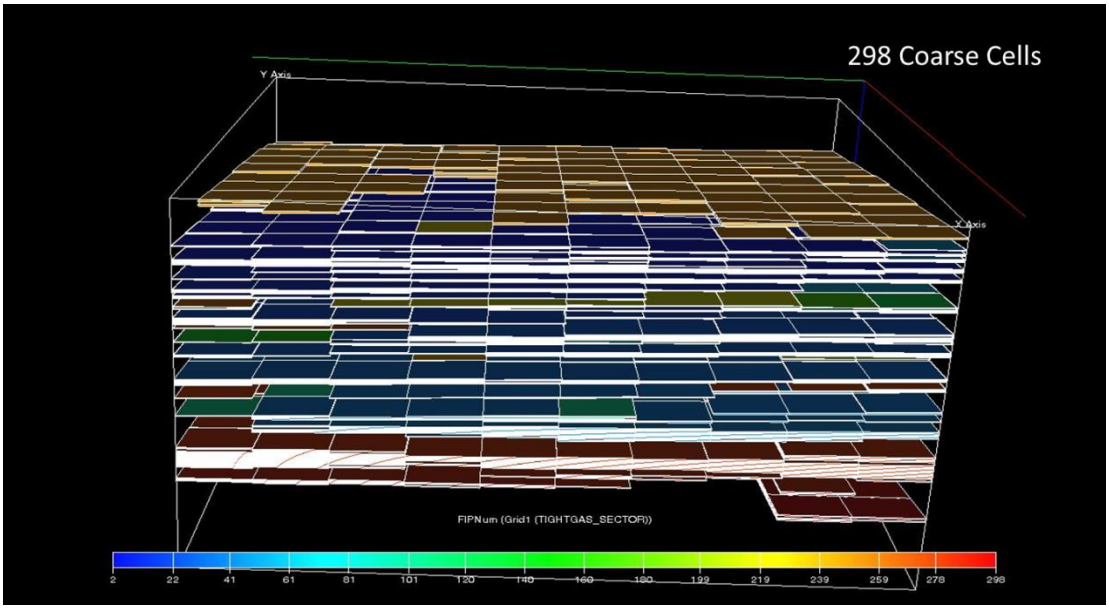

Figure 2-40: 3D adaptive coarse model. Cells with the same color ID are merged together.

Cells within the sector model are first divided into several groups, according to their diffusive time. The cells within the same month belong to same group. Then within each group, the cells will be sub-divided according to their connectivity. As shown in Figure 2-40, cells with the same color ID will be merge together, since they are connected to each other, and also have similar diffusive time of flight. Note that in order to preserve the well productivity, only vertical adaptive coarsening, 1x1xN, is applied for the well penetrated column.

Figure 2-41 shows a top view of layer 13 in this sector model, Cells with the same color ID are merged together.

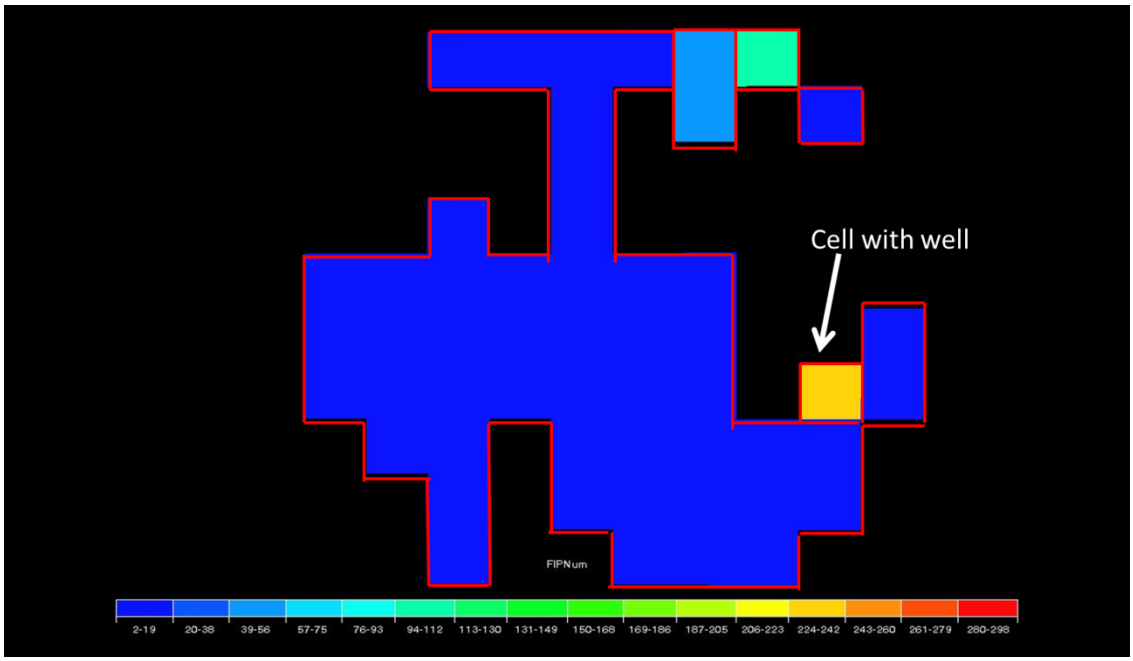

Figure 2-41: Topview of layer 13 in this sector model.

From Figure 2-41, extremely bizarre cell geometry could be observed. The implementation of 3D adaptive coarsening is based on the Nexus unstructured workflow, as discussed before. Once the fine scale pore volumes, intercell transmissibilities, and well indices are generated by simulator pre-processor, we will replace these properties with the calculated upscaled properties.

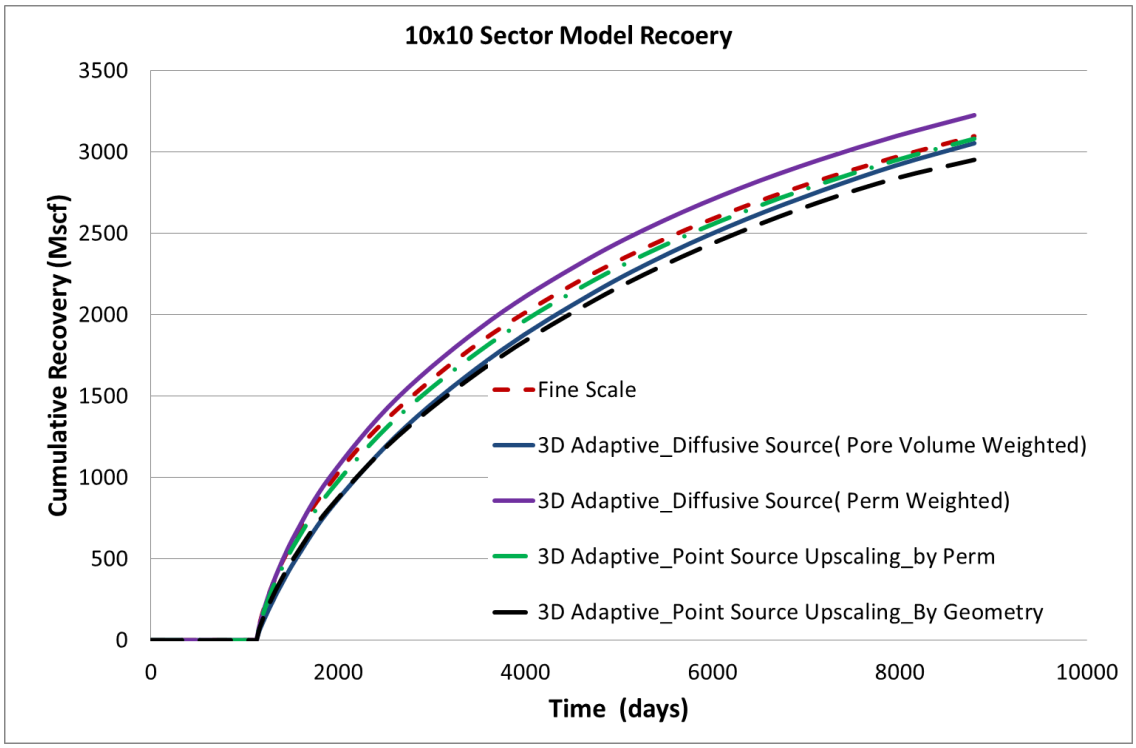

Figure 2-42: Recovery curves of 3D adaptive coarse model with different upscaling methods.

The cumulative recovery versus time of 3D adaptive coarse model with different transmissibility calculation methods is shown in Figure 2-42. Figure 2-42 also includes the recovery curve of the fine scale geologic model.

The recovery curve of fine scale geologic model is shown in the red line. Diffusive source transmissibility upscaling is shown in blue and purple curve, which are pore volume weighted and permeability weighted flux distribution. With the same upscaling method, how to assign the flux distribution can influence the final results. Permeability weighted flux distribution seems overestimate the recovery, and pore volume weighted flux distribution seems underestimate the recovery.

Point source transmissibility upscaling is shown in green and black dash line, depends on how to place the pressure source and sink. Green line shows the recovery when we place the source and sink at the highest permeability cell, while black line shows the recovery when we place the source and sink at the geometrical center of the coarse cell. Note that the source and sink locations can also influence the final results. Through the comparison, it seems point source transmissibility upscaling, when we place the source and sink at the highest permeability cell, could produce the most accurate results. But does this technique can apply to the full field model?

2.8.3 Full Field Application

We also apply the same upgridding & upscaling strategies for the full-field model, the recovery comparison is shown in Figure 2-43.

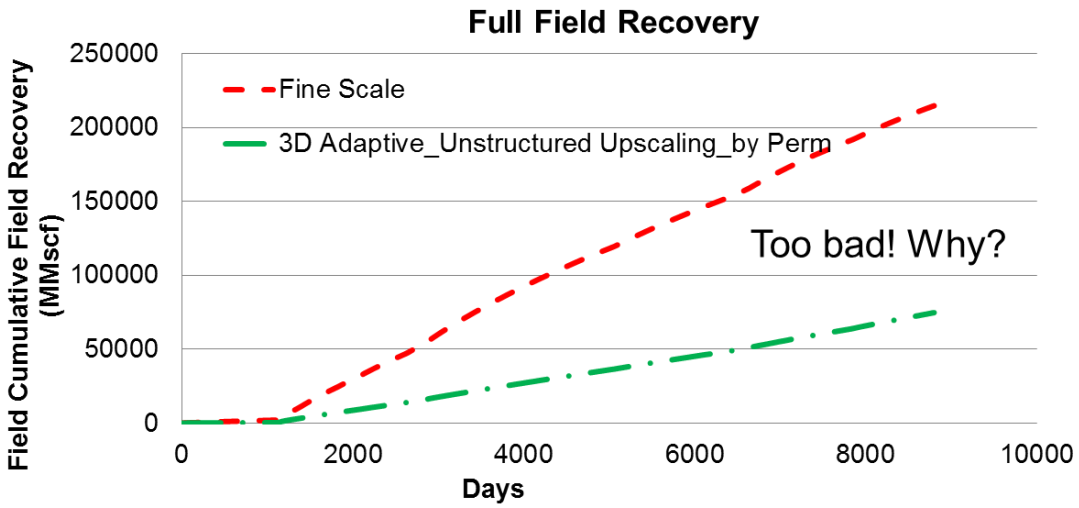

Figure 2-43: Full field recovery curve of 3D adaptive coarse model.

Figure 2-43 shows that 3D adaptive coarse model greatly underestimate the recovery. Same technique that works for 10x10 sector model, does not work for the full field model. This is because that we only studied the single well depletion within the sector model, and in the full field model, multiple wells depletion behavior cannot be preserved here. Also, 3D adaptive coarsening in the full field model would produce the cell with extremely bizarre geometry, due to the larger coarse scale.

2.9 Technology Transfer

Previous section discussed 1x1xN, 2x2xN, 3x3xN and 3D adaptive upgridding & upscaling strategies. Each strategy has its own limitations and advantages. We studied these strategies with Nexus unstructured workflow. To compare different simulator performance, we also implement the adaptive strategies into different simulators, shown in Figure 2-44.

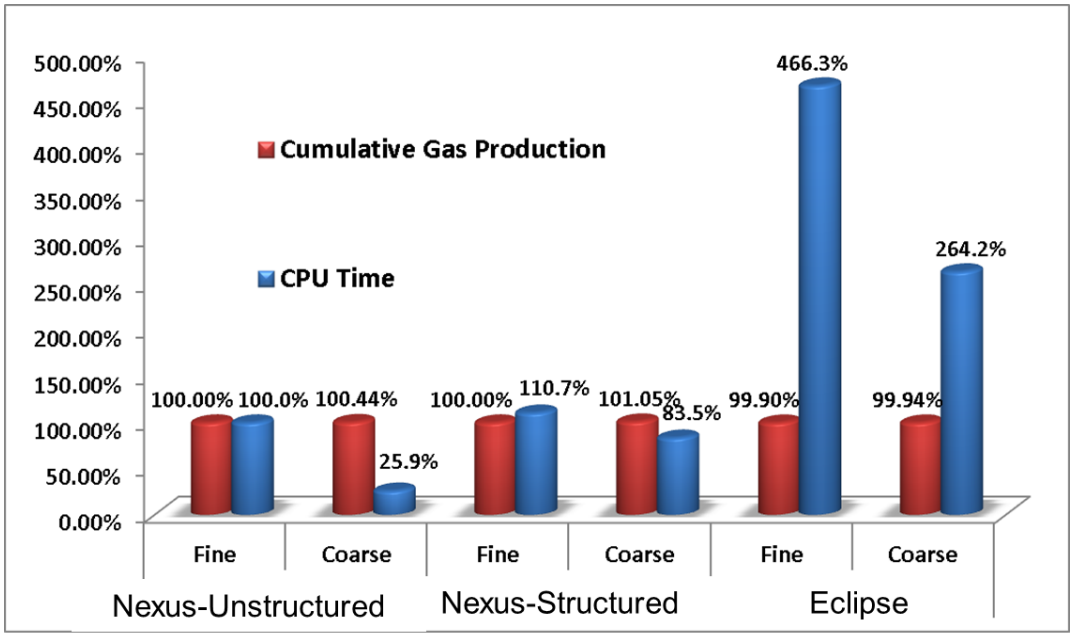

Figure 2-44: Adaptive upscaling strategy performance in different simulator (King et al., 2013).

Our reference case would be the simulation time and result on Nexus unstructured workflow. Figure 2-44 shows that the same technique cannot bring as much benefit on structured workflow (Nexus and Eclipse), as that on the unstructured workflow. The reason maybe that this technique generates lots of non-neighbor connections. The simulator takes relatively longer time processing the transmissibility multipliers assigned for those unstructured grids in the structured workflow, compared to assigning the transmissibilities directly in the unstructured workflow. Also, with the same model, it seems Eclipse would take longer simulation time, compared to Nexus.

In common with unconventional source rock plays, it is important to understand near well fracture characteristics in tight gas reservoir simulation. To achieve this objective, we combine local grid refinement with adaptive upscaling techniques to design a complex multi-scale simulation model (King et al., 2013). The multi-scale simulation model has very high resolution near the fractures, high resolution for the interaction between a well, its fractures, and the reservoir, and progressively lower resolution between wells. The extreme low resolution is reached by using adaptive upgridding technique with transmissibility upscaling.

Below figures show an example of such multi-scale simulation model. The reservoir structures and distributions of the fractures are presented in Figure 2-45. Vertical fractures penetrate the whole geologic model and the horizontal wells are restricted within certain zones. Figure 2-46 shows a cross-section view of the pore volume of the hydraulic fractures in the multi scale reservoir model. The fractured wells are represented with non-uniform distributed LGRs in both x and y directions. The near fracture regions are preserved as a transition zone. For all other cells that are away from the fracture locations, pillar based coarsening algorithm is applied. Various cell pore volumes for the coarsened cells can be observed in Figure 2-46.

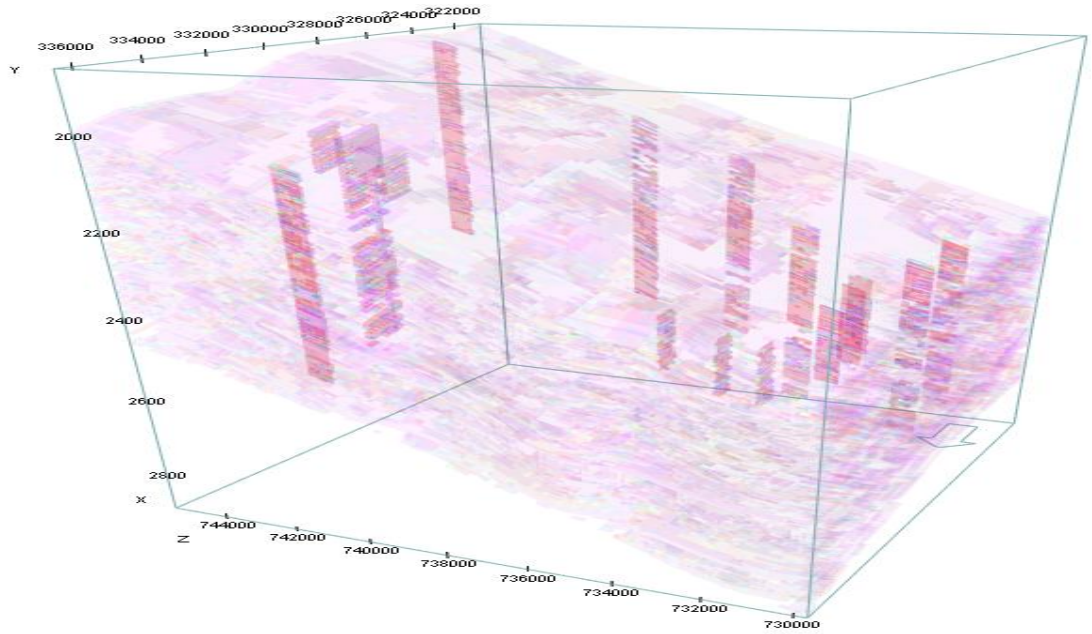

Figure 2-45: Fracture distributions and cross-section of upscaled models.

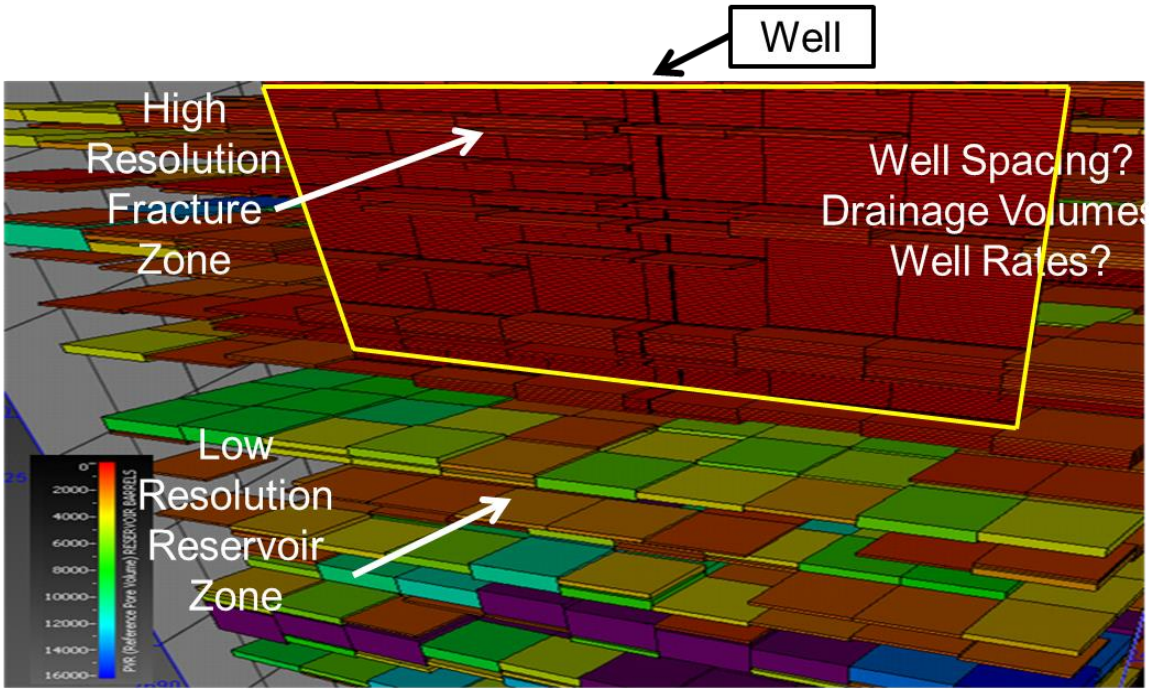

Figure 2-46: Cross-section view of the fracture representation in a multi scale model.

2.10 Conclusions

We developed novel techniques for robust upscaling of tight gas reservoir models. Adaptive coarsening is systematically more effective than current layer based upgridding techniques. 1x1xN adaptive coarsening will preserve the connectivity of pay cells and barriers of non-pay cells. With the use of well index and transmissibility upscaling it will generate upscaled model which can preserve internal reservoir heterogeneity with the minimum cell count. Even better simulation performance is obtained with 2x2xN adaptive coarsening where over a factor of 10 CPU time reduction has been achieved. However, 2x2xN coarsening may not preserve all of the lateral barriers, especially those associated with large diffusive time. The simulation results are not as accurate as those for 1x1xN adaptive coarsening. 3x3xN adaptive coarsening could further achieve a factor of 20 CPU time reduction. But it has a higher chance to lose the lateral barriers, thus, produce a relatively large error. However 2x2xN, and 3x3xN coarsening does generate the upscaled model with the minimum cell count. It provides a very good option if we do not have a strict requirement for the accuracy. A detailed illustration of these techniques' performance is listed in Table 2.

Options	Error	CPU Speed Up Factor
1x1xN	0.4%	3.5
2x2xN	1%	12
3x3xN	3%	20

Table 2: The performance of coarsening strategies

We introduce the depth of investigation and diffusive time of flight to understand tight gas reservoir pressure continuity, which can guide us develop the adaptive upgridding strategies to honor the continuity of the reservoir sands.

We also designed the 3D adaptive coarsening to preserve the reservoir sands continuity and barriers. However, due to the limitation of cell geometry and corresponding upscaling issue, we cannot apply this technique to large scale tight gas field. Further investigation is still required.

3. A SIMULATION-FREE APPROACH FOR WELL PLACEMENT UNDER UNCERTAINTY IN TIGHT GAS RESERVOIRS*

3.1 Introduction

The development strategy of any field highly depends on the placement of infill wells. Successful placement of the infill wells would not only increase the oil or gas production, but also improve the understanding of the reservoir description and performance, thus reducing the uncertainty or risk during the subsequent reservoir production. Therefore, well placement optimization has been one of the most important topics for reservoir studies. In tight gas reservoirs specifically, well locations depend upon the internal reservoir heterogeneity, the complex dynamic reservoir response associated with depletion history, and also the uncertainties associated with the reservoir parameters.

Previous well placement optimization work utilized some optimization algorithms, like genetic algorithm (Centilmen et al., 1999; Yeten et al., 2003), or gradient-based optimization algorithm (Sarma et al., 2008; Vlemmix et al., 2009), with an attempt to locate the optimum infill well location which can maximize a particular objective function. Such optimization methods proved good application for the infill well placement; however, they always require a large number of iterations to converge. They are also very sensitive to the starting point, thus pose great computational burden for the routine application, especially for the high resolution large scale field application. Da Cruz et al. (2004) proposed quality maps which convert 3D reservoir models into 2D maps showing cumulative oil production by perforating the well through all the layers, but it still requires a large number of flow simulation runs. Later work (Kang et al.,

2011; Taware et al., 2012) proposed a similar "quality map", which is typically based on static properties, like absolute permeability, porosity, etc. and dynamic properties, like pressure, viscosity, saturation, etc. By combining the static properties with dynamic properties, a good correlation could be detected between the proposed combination and the exhaustive calculation map. These methods can effectively determine the sweet spots for infill well location, or provide good starting point for the optimization algorithms. However, they still rely on reservoir or streamline modeling to acquire the dynamic properties for the reservoir, which are designed to represent secondary recovery, not primary depletion.

Zhou et al. (2013) proposed a simulation-free workflow to determine the infill well location for the tight gas reservoir management. We also suggest a quality map, which is a combination of static and dynamic properties, to place the infill wells in the tight gas reservoir. The dynamic property we utilize in this work is pressure, which is acquired through a geometric pressure approximation (Xie et al., 2012), instead of flow simulation. As the later section shows, the geometric pressure approximation may not give the exact pressure solution, but the pressure ranking from this approximation is quite close to that obtained from flow simulation, thus good enough to generate the quality map.

The uncertainty is also an important aspect that cannot be neglected in any of the reservoir studies, due to the sparse well data and the difficulty in accurately relating geophysical/petrophysical measurements to reservoir-scale heterogeneities. Without doubt, uncertainty should also be taken into account to determine the infill well locations. Earlier studies (Da Cruz et al., 2004; Taware et al., 2012) account for geologic uncertainty by using multiple plausible realizations, the optimum infill well location is determined based on the mean or expected value of all realizations. However, a few realizations cannot provide detailed information about the geologic uncertainty, plus the computational cost scales with the number of realizations. Probability approaches and

risk analysis (Yuen et al., 2011; Manceau et. Al., 2001) are also proposed to quantify the subsurface uncertainty during well placement optimization. They can provide detailed assessment of the subsurface uncertainty, but the expensive simulation limits the application to large scale reservoir models.

We propose a different method to represent geologic uncertainty, and also take it into account for infill well placement. Besides the quality map, we propose a corresponding uncertainty map, through a spatial connectivity analysis and the variogram in the static model. Assuming we have the most confidence about the data at the existing well locations, then as the distance from the existing wells increases, our confidence about the data at this particular location decreases, and the risk correspondingly increases. Combining the quality map and uncertainty map, good infill well locations and drilling sequence can be determined for improved reservoir management.

Without considering subsurface uncertainty, the sweet spots for well placement are often the un-depleted regions far from existing wells. However, these regions would also be the most risky in that we have the least confidence about the reservoir model far from well data. We contrast a multi-year drilling sequence, with and without this risk assessment and show the benefit including risk. We also contrast our approach with a uncertainty assessment based upon multiple realizations to further show the benefits of our proposed workflow.

The structure of this section is as follows: first, we outline our approach and basic mathematical background. Next, we demonstrate this approach on the 10x10 test area of a U.S. on-shore tight gas reservoir model. After that, we utilize this approach to design the depletion schedule for the full field tight gas reservoir model. Then, we contrast this multi-year drilling sequence, with and without this risk assessment and show the benefit including the subsurface uncertainty. Next, we will compare our uncertainty assessment method with the one that using multiple realizations, and provide some guidelines on the

management of the uncertainty of recovery predictions. In the end, we briefly conclude this work.

3.2 Proposed Approach

A good quality map always combines the static properties and dynamic properties, since the dynamic properties can take the dynamic reservoir response into consideration, to best represent the production/depletion history. For tight gas single phase depletion, pressure best represents the reservoir dynamic response, since it is the primary recovery mechanism. After a detailed comparison of different column-based properties, the combination of permeability, net pay thickness, and pressure (defined as recovery potential in this section) shows a good correlation with the exhaustive recovery calculation, which will be discussed in the next section.

The quality map is built based on a deterministic model. To account for the geologic uncertainty, the corresponding uncertainty map should be also taken into consideration for the placement of infill wells. Typically, we have the most confidence about the well data, and as the distance from the wells increases, our confidence about the data at this particular location decreases, and the risk correspondingly increases. The uncertainty map is generated from the variogram map through the geostatistical analysis.

The objective of this section is to outline the proposed approach and basic mathematical background for each step, including the geometric pressure approximation, proposed recovery potential map, and the corresponding uncertainty map.

3.2.1 Geometric Pressure Approximation

This work utilizes the geometric pressure approximation (Xie et al. 2012), instead of flow simulation to calculate the recovery potential. The derivation of the geometric pressure solution starts from the diffusivity equation. For radially symmetric flow, diffusivity equation is shown as following:

$$A(r)\phi c_t \frac{\partial p}{\partial t} = \frac{\partial q}{\partial r} \qquad q = \frac{kA(r)}{\mu}\frac{\partial p}{\partial r} \tag{3-1}$$

Here, q is the Darcy flux, and A is the cross surface area for the Darcy flux. For cylindrical radial flow, $A = 2\pi rh$; for spherical radial flow, $A = 4\pi r^2$; for linear flow, A is a constant. Eq. (3-1) can also be expressed in terms of pore volume, and then it becomes:

$$c_t \frac{\partial p}{\partial t} = \frac{\partial 1}{\partial V_p} \qquad V_{\mathrm{p}}(r) = \phi\int_0^r A(r)dr \tag{3-2}$$

Here, V_{p} is the drainage volume, which is obtained from the Fast Marching Method (Xie et al. 2012). If we assume that the drainage volume acts as a moving no flow boundary, the Darcy flux is negligible beyond the drainage volume. Within the drainage volume, the pressure can be approximated by a pseudo steady state solution; Eq. (3-2) can be further simplified as:

$$\frac{\partial p}{\partial t} \cong \frac{\partial \bar{p}}{\partial t} = \frac{1}{c_t}\frac{q_w}{V_p(r(t))} \tag{3-3}$$

Here, we assume q_w is the constant well rate, the corresponding constant rate pressure drawdown is obtained by integrating Eq. (3-3) starting from a time after which the drainage volume boundary passes over the location, shown as Eq. (3-4):

$$\Delta \mathrm{p} = \int \frac{1}{c_t}\frac{q_w}{V_p(r(t))}\,dt \tag{3-4}$$

Geometric pressure solution at constant well rate is obtained using Eq. (3-4). Gupta et al. (2012) also proposed the pressure solution at constant well pressure, which is not discussed in this section.

This equation assumes that the pressure drop at any point is primarily due to the first arrival pressure waves (direct or transmitted) and the pressure drop due to pressure waves reflected from media boundaries is minimal. Therefore, the geometric pressure solution may not acquire the accurate pressure solution, but as later will show, the pressure ranking from this solution is quite accurate. The geometric pressure solution has proven to be a good pressure approximation approach which we can apply without flow simulation. This work utilizes this approach to estimate the pressure changes during the depletion history of a tight gas reservoir. A detailed illustration will be shown in next section.

3.2.2 Quality Map: Recovery Potential

The proposed recovery potential is a combination of static properties such as permeability (k), net pay thickness (h) and dynamic properties, specifically pressure (p). Considering a well perforating cell, for single phase flow, the flux is obtained as:

$$q = \frac{2\pi kh}{(\ln \frac{r_o}{r_w} + s) \cdot B \cdot \mu}(p - p_{wf}) \tag{3-5}$$

If we assume the geometry of simulation cells is similar, which is true for our studied model, and neglect the changes of formation volume factor (B) and viscosity (μ), then we can neglect the denominator part of Eq. (3-5). Also, to account for the boundary effect, 2π is adjusted to π if at the edges and $\pi/2$ if at the corners, since the central area should be more attractive than the area near the edges and corners. Therefore, our proposed recovery potential is defined as:

$$RP = 2\pi kh(p - p_{wf}) \tag{3-6}$$

Assuming a constant bottom hole pressure for each infill well, we calculate the recovery potential for each cell, then take the summation for every column of the model. The 2D

recovery potential map shows a good correlation with an exhaustive calculation of the recovery through the flow simulation by placing the infill well at every column of this model. As shown in next section, the proposed recovery potential is much better than the other properties or properties combination, since it can best represent the flow capacity and depletion potential of every infill candidate without any simulation runs.

3.2.3 Uncertainty Map

The recovery potential map only works for a deterministic model. Without considering uncertainty, the infill well location from this map may select areas in which we have the least confidence in the model. To account for the geologic uncertainty, the corresponding uncertainty map should be also taken into consideration for the placement of infill wells.

We first consider the data at well locations are from reliable measurements. However, at the other areas, due to the sparse well data, we rely on the geostatistical techniques or geophysical/petrophysical interpretations, which we do not have so much confidence. Uncertainty map is actually an uncertainty index that permits the ranking of data at each location in order of reliability. Assuming we have the data information, Isaaks & Srivastava (1989) proposed an uncertainty assessment that quantifies the reliability of the data based on Kriging interpretation (Appendix A). Zhou et al. (2013) utilized this method to produce the uncertainty map. Here, we introduce a different uncertainty assessment method, which does not require the data information of studied area. The variogram map is obtained first from the geostatistical analysis. Based on the variogram map, and the existing well locations, the corresponding uncertainty map could be determined, which will be shown in later section.

To incorporate the uncertainty map with the recovery potential map, we propose the recovery potential with risk, as following:

$$APWR = 2\pi kh(p - p_{wf}) \cdot (1 - \text{Uncertainty}_{Normalized})^{a} \quad (3\text{-}7)$$

Here, the uncertainty index is normalized. The coefficient a at is introduced to account for the degree of confidence in the static model, for example, more aggressive plan would pose less weight on the confidence term, smaller a accounts for more risk we like to take for the well placement, $a = 0$ means the uncertainty is not taken into consideration, thus becomes the most dangerous well placement. Here, we suggest $a = 1$ for the well placement in this section, but the other values can also be utilized depends on the different decision making procedures.

3.3 Procedure Illustration: Tight Gas Sector Model

In this section, the same tight gas model is utilized here for infill well placement, as the upscaling work we presented before. We demonstrate the procedure using the 10x10 test area of a large scale U.S. on-shore tight gas reservoir model. The sector model is used to validate our procedure, and we will discuss the field application in the large scale model in the next section.

The 3-D sector model with 10x10x375 grid blocks only has one producing well, which locates at cell (9, 7), perforating from layer 1 to 300. The well is shut in for the first 3 years, then start producing at constant pressure 900 psi. Figure 3-1 shows the final pressure of this sector model after 24 years depletion (same with Figure 2-2), and the cumulative gas recovery for this well.

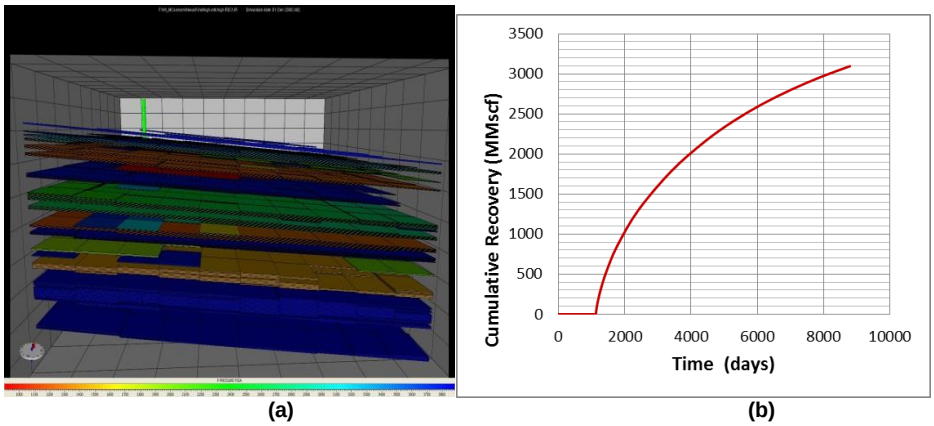

Figure 3-1: Single well depletion within 10x10 sector model. (a): Final pressure of this sector model after 24 years depletion; (b): Cumulative recovery for this well

The final pressure shown in Figure 3-1a varies from 900 psi to 4000 psi. The red area is the drainage volume, pressure here is close to 900 psi, almost the same with the bottom hole pressure, since it has excellent communication with the well. On the other hand, the blue area is the isolated volume; pressure here is close to 4000 psi, close to the initial pressure, since it does not have a connection with the well. Therefore, Figure 3-1a also shows the depletion pattern of this sector model. The objective of the infill well placement is to determine the best infill location within this model to deplete as much as possible isolated volumes, and thus boost the cumulative recovery after 24 years existing depletion history.

In order to validate our approach, a reference map, which is an exhaustive calculation of the cumulative recovery by placing a well at each available location and performing flow simulation, is generated for comparison. Since this work only considers vertical wells, the available locations are every column of this model. We can convert the 3-D model into 2-D map, shown in Figure 3-2a.

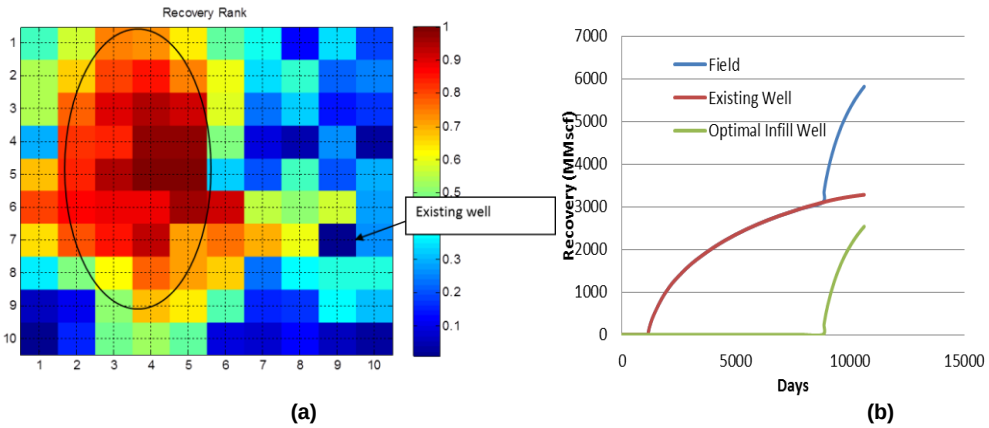

Figure 3-2: Reference map from exhaustive calculation. (a): Exhaustive calculation of the cumulative recovery, generated by placing a well at each available location, and producing 5 years more. Red region (circled) is the recommended good infill well locations. (b): Cumulative recovery of existing and optimum infill well. Infill well starts producing at 24 years after the existing well. Optimum location is chosen from the exhaustive calculation, which shows the maximum cumulative recovery, locates at cell (5, 5). Note that the optimum location is based on the deterministic model, if the uncertainty is included, the location may also change.

Figure 3-2a shows the cumulative recovery rank for every infill well location within 5 years, the red region means higher rank of the cumulative recovery, thus becomes the sweet spot for the infill well placement. Blue region means lower rank of the cumulative recovery; it is not as attractive as the red region for infill well placement. This map is generated by performing flow simulation for every possible location within this model; therefore, 100 simulation runs are required. The expense of this computation makes it infeasible for the large scale field application.

The quality maps have been proposed (Kang et al., 2011; Taware et al., 2012) to mitigate the computational burden. As discussed in previous section, quality maps are the combinations of static and dynamic properties. By choosing the appropriate combination, we can get a good correlation with the exhaustive calculation of recovery map.

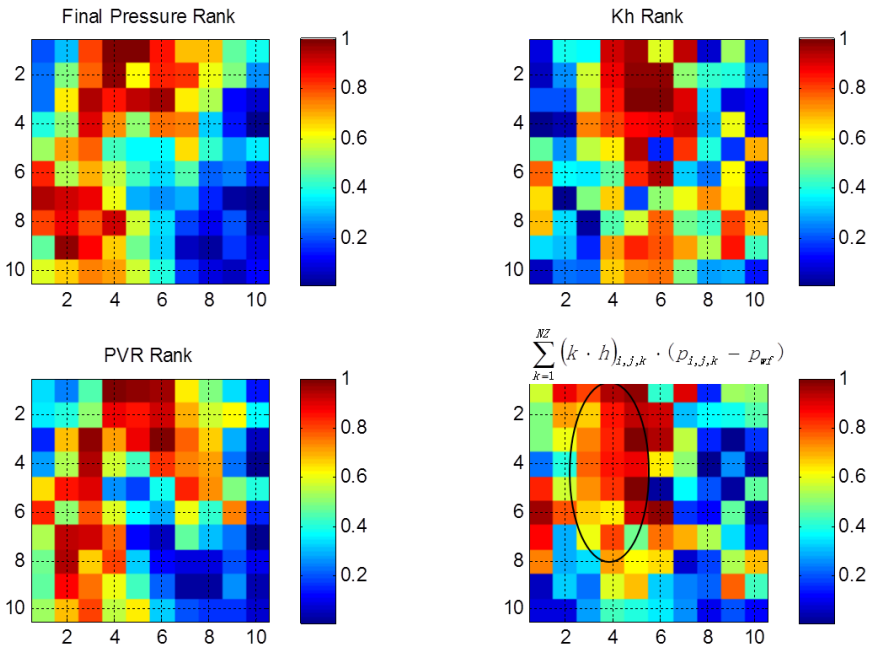

Figure 3-3: Different column-based properties or properties combination for the sector model. From top left to lower right, they are the final pressure map, flow capacity map, pore volume map, and a new combination of flow capacity and final pressure difference map. We sum all the properties or properties combinations within the same column, and rank them from smallest to largest. Red region is the higher rank area, and blue region is the lower rank area.

Figure 3-3 compares different column-based properties or properties in combination. The combination of flow capacity and final pressure difference map seem to match with the recovery map much better than the other properties, except the area near the corners and edges, which is caused apparently by the boundary effect. To further improve the quality map, Eq. (3-6) is utilized here to include the boundary effect, note that the coefficient 2π is adjusted according to the position of the infill well locations. Figure 3-4 shows a detailed comparison of the exhaustive calculation of recovery and the recovery potential map, defined in Eq. (3-6).

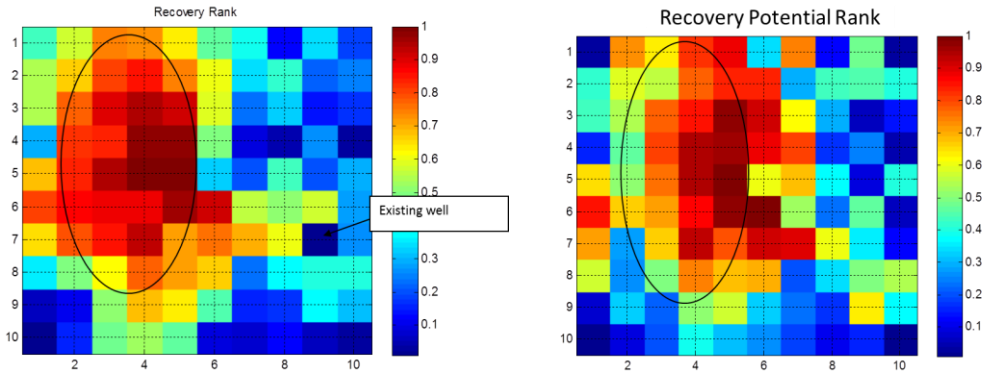

Figure 3-4: Comparison of the reference map and the recovery potential map. (a): Exhaustive calculation of recovery; (b): Recovery potential map, defined in Eq. (6). The sweet spots circled are quite match in both maps.

Figure 3-4 validates that the recovery potential map can be utilized to choose the sweet spots for infill well placement; at least, it could provide a good starting point for any optimization algorithm. For this particular sector model, the highest rank in both maps is cell (5, 5). Note the recovery potential map requires the final pressure information, and the pressure we utilized for the above figures is still from simulation, that is to say, one simulation run is still required.

Our previous work introduced the 1x1xN, 2x2xN and 3x3xN adaptive coarsening strategies to build the accurate and efficient simulation models, which can decrease the simulation time by at least one order magnitude. And we also show that these coarse models can provide very accurate pressure predictions. Here, we can also check the recovery potential of each coarse model, which is shown in Figure 3-5:

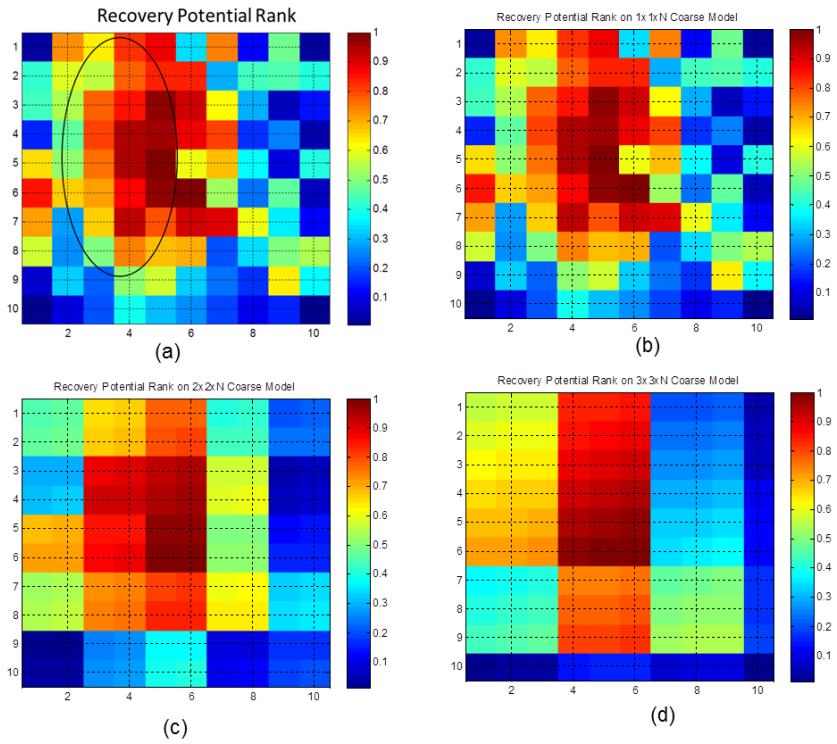

Figure 3-5: Recovery potential map on each simulation models. (a): Recovery potential map on the fine scale model; (b): Recovery potential map on the 1x1xN coarse model; (c): Recovery potential map on the 2x2xN coarse model; (d): Recovery potential map on the 3x3xN coarse model. Note that at the boundary of this sector model, 1x3xN, or 3x1xN adaptive coarsening is applied.

Figure 3-5a shows the recovery potential of the fine scale model, which is same with Figure 3-4b. The recovery potential of 1x1xN coarse model (Figure 3-5b) is almost same with that of fine scale model, since the pressure and well productivity is accurately preserved in the coarse model. The recovery potential of 2x2xN and 3x3xN coarse models can also roughly estimate the sweet spots for the infill wells, despite the decreased resolutions. Therefore, our adaptive coarsening strategies also have a good application in the infill well placement.

One of the objectives of this work is to develop a simulation-free approach, which can be utilized efficiently and accurately for large scale reservoir development. From this

perspective, the geometric pressure approximation provides a useful tool to achieve this objective. The theoretical background of geometric pressure approximation has been discussed in the previous section. Now we apply this approximation to obtain the pressure solution for this sector model. Figure 3-6 shows a comparison of pressure drop, from flow simulation and the geometric approximation. From the comparison of Figure 3-6a and 3-6b, we found that geometric pressure approximation cannot give the exact pressure solution, but it roughly estimates the pressure change magnitude. Also from Figure 3-6c and 3-6d, pressure ranking from approximation is quite close to the flow simulation.

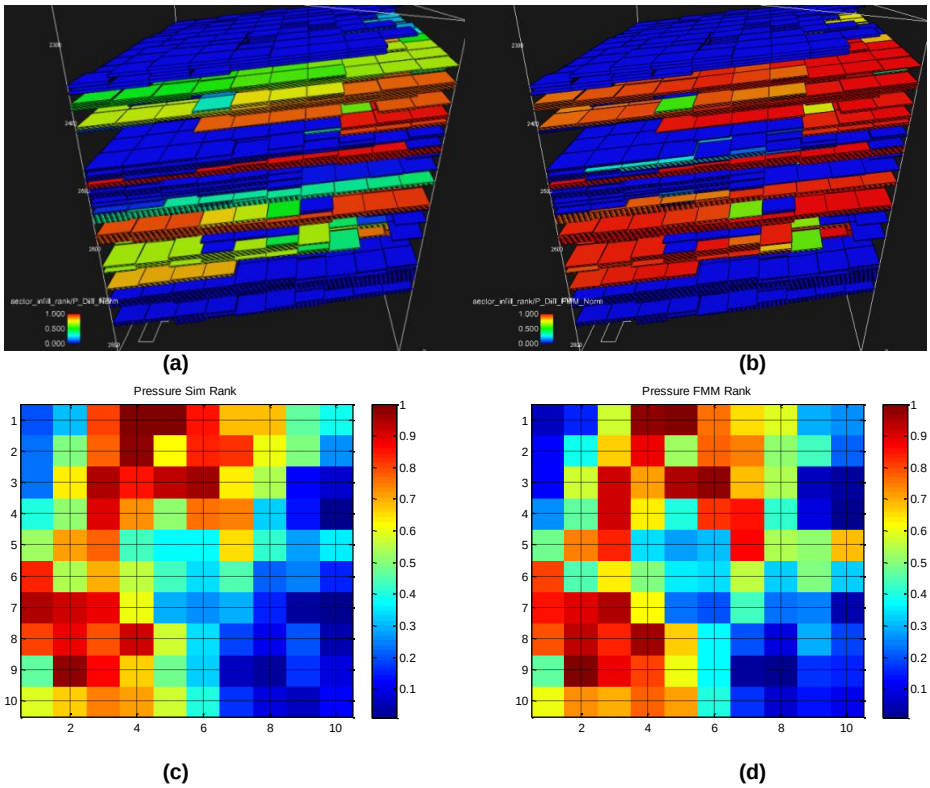

Figure 3-6: A comparison of pressure, from the simulation and geometric approximation. (a): Normalized pressure drop after 24 years depletion from the flow simulation. (b): Normalized pressure drop after 24 years depletion using geometric pressure approximation. (c): Column based pressure rank from simulation. (d): Column based pressure rank using geometric pressure approximation. Geometric pressure approximation may not give the exact pressure solution, but the pressure ranking from approximation is quite close to the flow simulation.

Through a comparison of the recovery potential map, generated by flow simulation, and geometric pressure approximation, shown in Figure 3-6, we can still see that geometric pressure approximation works very well for the pressure, and recovery potential ranking, thus becomes a useful approach for the infill well placement.

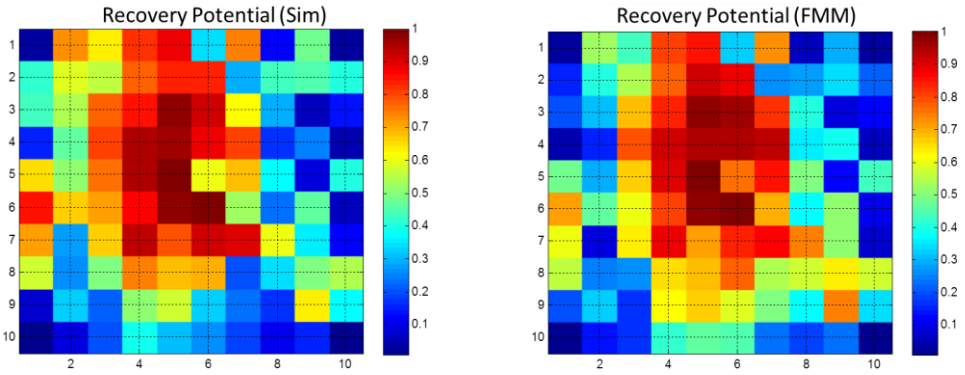

Figure 3-7: Recovery potential maps. (a): Flow simulation; (b): Geometric pressure approximation.

Above discussions are all based on the deterministic model, including the exhaustive recovery calculation, and the recovery potential maps, the geologic uncertainty has not been considered so far. However, as discussed before, the uncertainty cannot be neglected in any of the reservoir studies, due to the sparse well data and the difficulty in accurately relating geophysical/petrophysical measurements to reservoir-scale heterogeneities. Following the discussions in previous section, we incorporate a permeability uncertainty map to the recovery potential, Eq. (3-7) to determine the infill well location.

Figure 3-8a shows the uncertainty map, generated by variogram map for this sector model, the higher rank means higher risk, and data in this region (red) is less reliable; and lower rank means lower risk, and data in this region (blue) is more reliable. The

existing well location is (9, 7), blue areas are the lower risk regions, since they are close to the existing well location. And red areas are the high risk regions since they are far away from the existing well location. Figure 3-8b shows the recovery potential with risk map, generated by Eq. (3-7). It shows that when we take the uncertainty into consideration, the optimum location becomes cell (6, 6), instead of cell (5, 5) from the deterministic model, which is closer to the exiting well (9, 7).

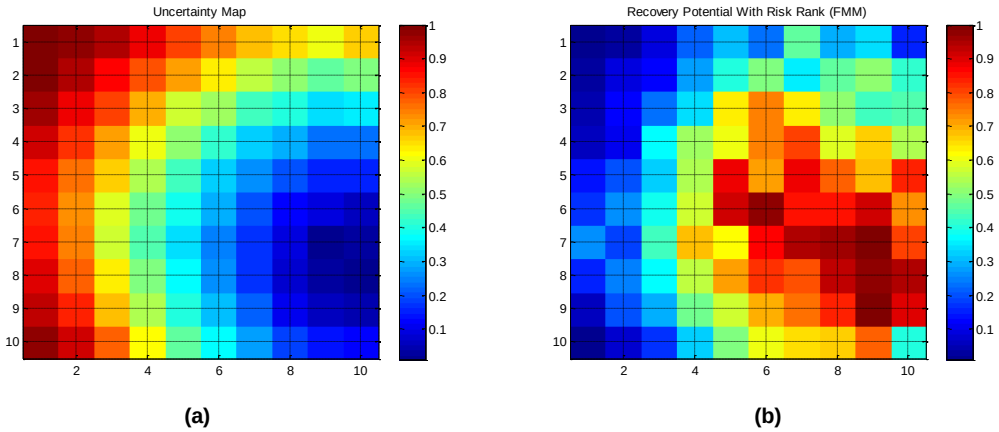

Figure 3-8: Well placement under uncertainty. (a): Uncertainty map, generated from the variogram of this sector model; (b): Recovery potential with risk map, generated by Eq. (3-7).

To sum up, we validate the proposed approach using a 10x10 sector model. The recovery potential map we proposed shows a good correlation with the exhaustive flow simulations. From this map, we can infer the good infill well locations, or at least provide a good starting point for any optimization algorithm. We also propose the uncertainty map to access the geologic uncertainty, and also incorporate the uncertainty into the recovery potential to determine the infill well location. Geometric pressure approximation may not give the exact pressure solution, but it can provide accurate pressure ranking, thus is quite useful for the efficient infill well placement work.

3.4 The Drilling Sequence Design for Large Scale Tight Gas Reservoir

In this section, we study the full field tight gas reservoir development. Figure 3-9 shows a detailed description of this high resolution geologic model, and the statistics of some properties, which has been shown in Figure 2-1. Figure 3-9a shows the facies of this 3-D model with a relative uniform cell size. This is a multi-million cell model, red cells are non-pay cells, and blue cells are pay cells. The model is on a non-pay background, and consists of some intermittent connectivity within thin fluvial sands. Figure 3-9b shows the porosity of the pay cells only, the distribution is also relatively uniform. The majority of the pay cells have porosity values from 10%~15%. Meanwhile, Figure 3-9c shows a relatively heterogeneous permeability distribution of the pay cells within this model, with a range of 0.0001 to 10 md. 70% of the pay cells permeability is above 0.1 md, while the other 30% of the permeability is below 0.1md. Permeability shows a greater variance, thus, our uncertainty analysis will focus on the permeability data.

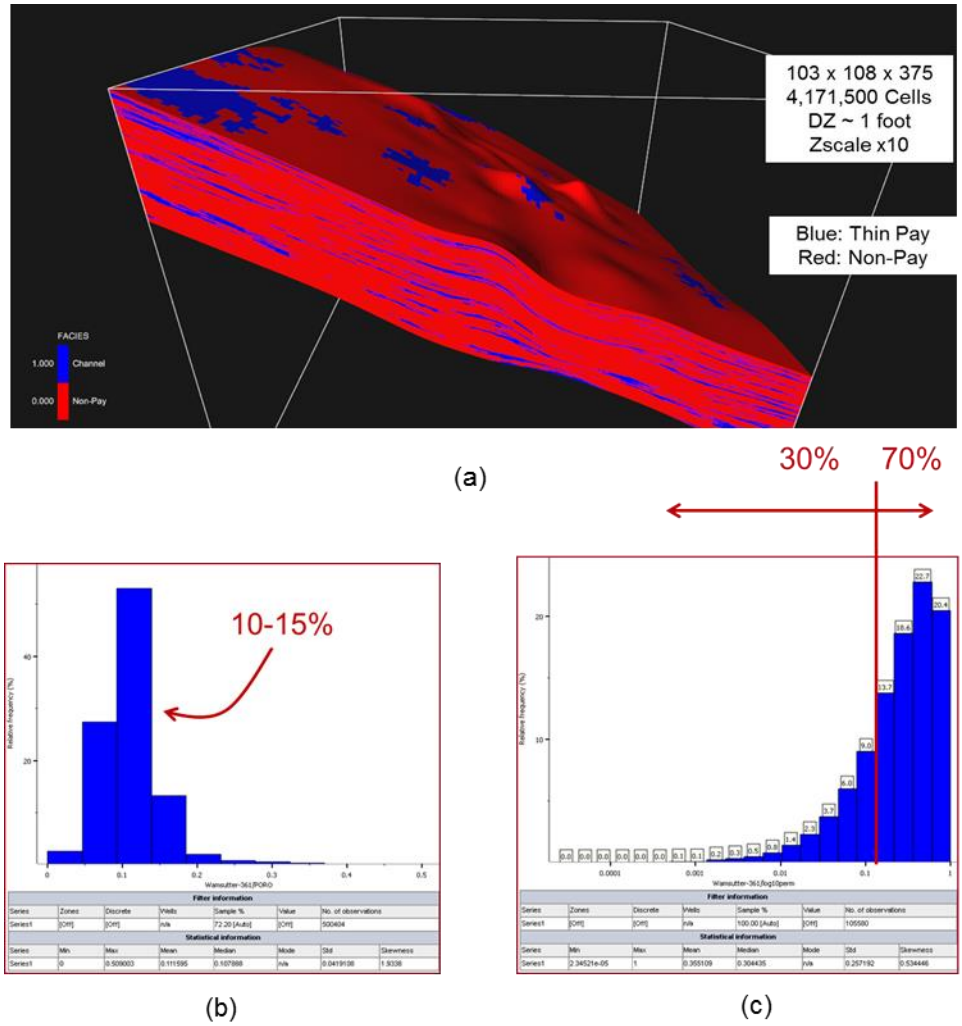

Figure 3-9: Statistics of a large scale tight gas reservoir. (a): High resolution geologic model of our studied field, red cells are non-pay cells, and blue cells are pay cells; (b): Histogram of the porosity for the pay cells only; (c): Histogram of the permeability for the pay cells only.

To access the geologic uncertainty in the permeability data, the variogram in major and minor direction, and the variogram map are calculated using Petrel workflow (Petrel, 2011). Petrel defines the semivariance variogram as:

$$\gamma(\mathrm{h}) = \frac{1}{2N(h)} \sum_{i=1}^{N(h)} \left| x_i - y_i \right| \tag{3-8}$$

Here: h is the separation distance, and $N(h)$ is the number of data pairs with same separation distance, x_i, y_i is the pair of data. Figure 3-10 shows the variogram information about the permeability data.

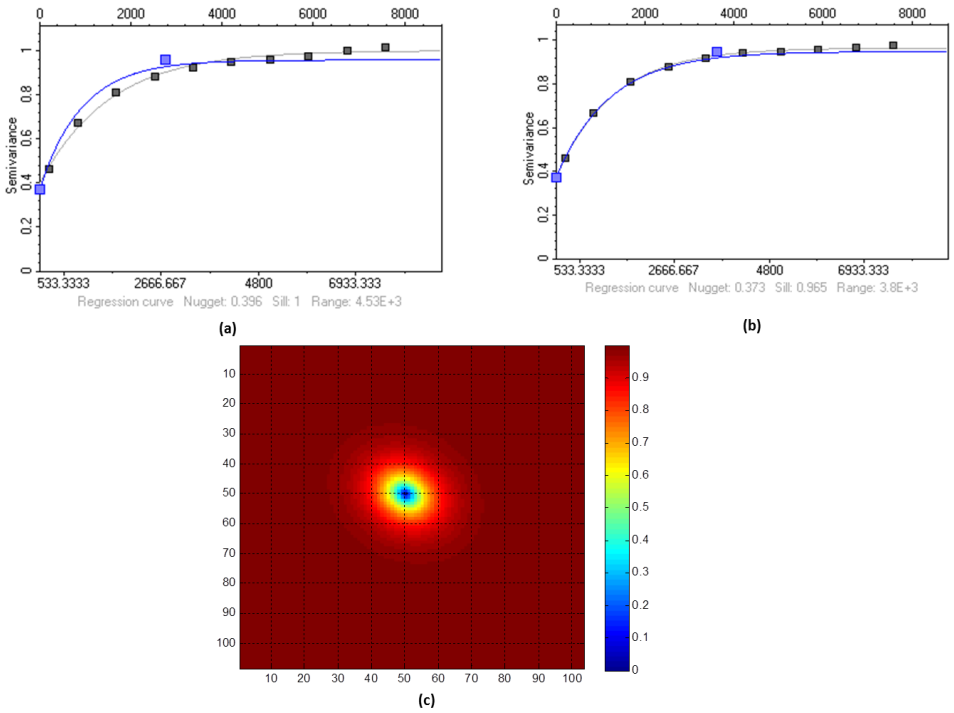

Figure 3-10: Geostatistical analysis for the large scale model. (a): The variogram in major direction, black line is the calculated curve, and blue line is the fitted curve; (b): The variogram in major direction, black line is the calculated curve, and blue line is the fitted curve; (c): The variogram map for the static model. Note that the semivariance is normalized here.

Figure 3-10a shows the variogram in major direction, basically is in the northwest direction, and the range in this direction is about 4,530ft. Figure 3-10b shows the variogram in minor direction, which is perpendicular to the major direction, and the range in this direction is about 3,800ft. The black curves are the calculated values, and the blue curves are the fitted curves using exponential variogram model (Petrel, 2011)

based on the calculated values. Figure 3-10c is the variogram map generated based on the fitted exponential variogram model. Once the well locations are available, it could be utilized to generate the uncertainty map for the infill well placement.

The objective of this section is to develop a good infill well drilling sequence for this tight gas reservoir field, thus, provides the reasonable development strategy for the large scale field management. Here, we utilize the proposed approach to achieve this objective by generating and updating the recovery potential and uncertainty map at each development stage. To simplify this problem, we assume the drilling cost per well is constant, and the drilling budget for the large scale field is 4 wells every 3 years. This is the economic considerations, or constraint, for this particular study, decision makers can also change the budget based on some practical considerations. For the demonstration purpose, we will show the workflow of the design of the first 3 development stages, about 10 years depletion history.

Assume this is a new tight gas field, which means we have zero confidence about the data in this static model, since there is no well before. Therefore, 4 appraisal wells are drilled first near the corners of this model, to acquire some confidence about the data. One year after the appraisal wells, we begin to place the infill wells at each development stage.

The design of first development stage is shown in Figure 3-11. Figure 3-11a shows the recovery potential map, using the initial uniform pressure information, since the 4 appraisal wells are shut-in. Without considering the uncertainty, we could see that central area is a good region for infill well placement. However, we also noticed that the central area also shows a higher risk, in Figure 3-11b, due to the longer distance to the existing wells. Figure 3-11c shows the recovery potential with risk map, when we take the uncertainty into consideration; the infill wells are all located at the neighborhood of

the existing wells. Figure 3-11d shows the pressure profile, since the initial 4 appraisal wells are shut-in (green well), the pressure remains at initial pressure.

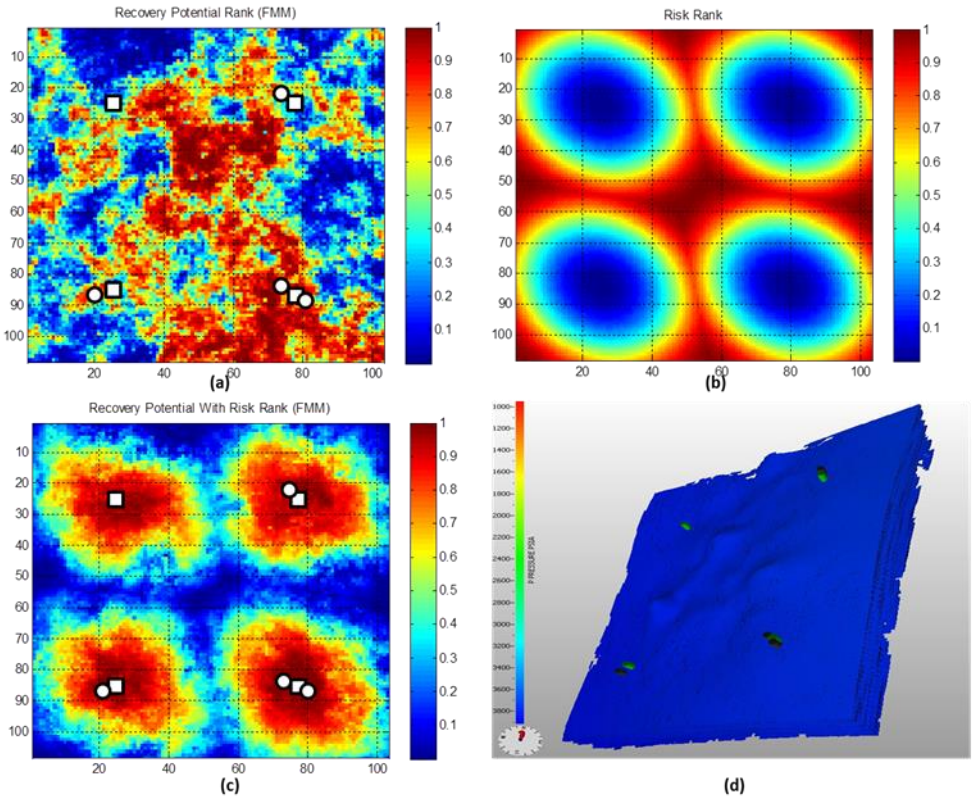

Figure 3-11: First development stage design, 4 infill wells within 3 years. (a): Recovery potential map using Eq. (3-6); (b): Uncertainty map from variogram map; (c): Recovery potential with risk map using Eq. (3-7). White square point marks the existing wells, and white round points mark the infill well locations. (d): Pressure profile, since the initial 4 appraisal wells are shut-in (green well), the pressure remains at initial pressure. Grey wells are the infill wells that are about to producing after one year.

Figure 3-11 only shows the initial recovery potential map and recovery potential with risk map. Actually both maps are updated when every infill well is placed. For example, the first well utilizes the initial uniform pressure information, but the second well utilizes the pressure information, which is after the certain time depletion of the first well (existing well). Note that the pressure is obtained from geometric pressure

approximation, instead of flow simulation. The geometric pressure approximation takes less than 1 minute to calculate while explicit flow simulation would have taken several hours to finish this large scale reservoir simulation.

Similarly, Figure 3-12 and Figure 3-13 show the design of the second and third development stages. Figure 3-12 and Figure 3-13 are generated based on the information after 4 years, and 7 years of depletion history, respectively. With the updating of recovery potential and uncertainty maps, the recommended infill well locations would also change. Interestingly, both figures show more wells are placed near the lower right corner, which has the lower risk due to the existing wells here, and the higher recovery potential due to the good reservoir quality here. More wells are placed in this region would bring more confidence about the data here. Therefore, we could observe that the area of lower risk region in the lower right corner is expanding due to the placement of infill wells. From the pressure profiles, we could see red regions are the drainage volumes, which are depleted by the existing wells, thus have the lowest pressure. And blue regions are the un-depleted volumes, which have not been depleted by the existing wells, thus have the highest pressure. Larger drainage volumes could be found in the lower right corner, with more wells depletion.

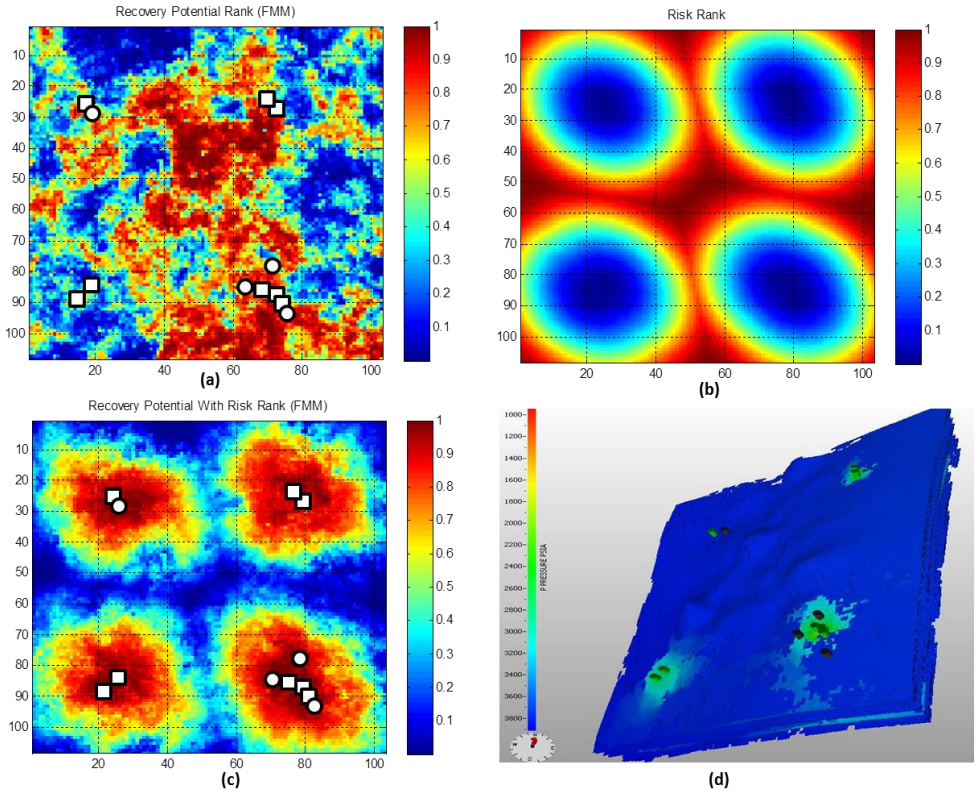

Figure 3-12: Second development stage design, 4 infill wells within 3 years. (a): Recovery potential map using Eq. (3-6); (b): Uncertainty map from variogram map; (c): Recovery potential with risk map using Eq. (3-7). White square point marks the existing wells, and white round points mark the infill well locations; (d): Pressure profiles after 4 years, green wells are the existing wells. Grey wells are the infill wells that are about to producing.

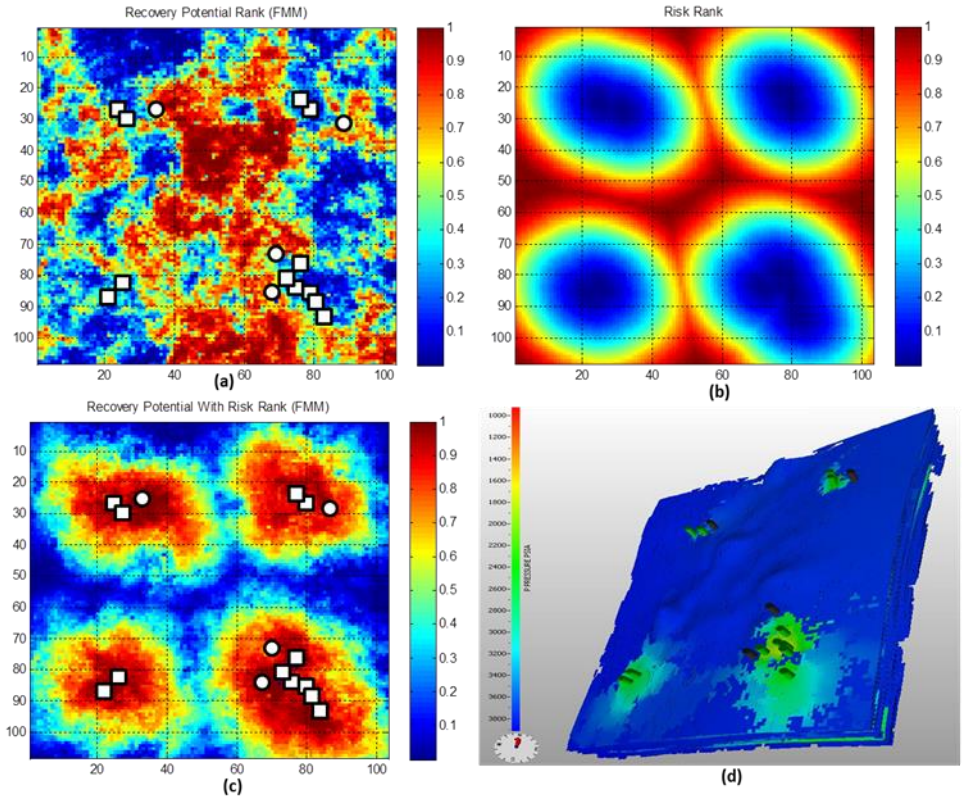

Figure 3-13: **Third development stage design, 4 infill wells within 3 years. (a): Recovery potential map using Eq. (3-6); (b): Uncertainty map from variogram map; (c): Recovery potential with risk map using Eq. (3-7). White square point marks the existing wells, and white round points mark the infill well locations; (d): Pressure profiles after 7 years, green wells are the existing wells. Grey wells are the infill wells that are about to producing.**

With another 3 years of depletion, the depletion pattern of the recommended wells and cumulative recovery is shown in Figure 3-14. The recovery is boosted every 3 years with the placement of infill wells. The wells are not only producing gas, but also providing information. As more wells are drilled in this field; our confidence about the data within this field will also increase; thus, can help us design a better development strategy.

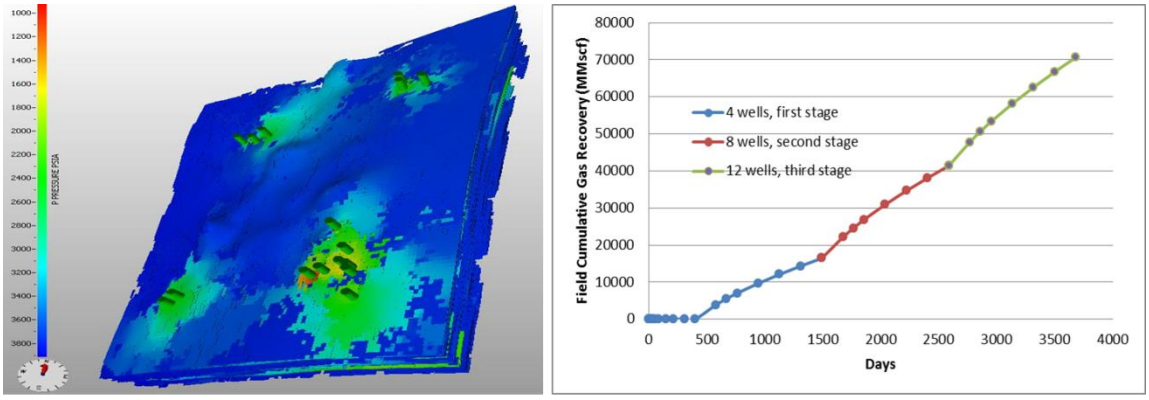

Figure 3-14: The depletion pattern of the recommended wells and cumulative recovery. (a): Final pressure after 10 years depletion schedule. (b): Cumulative recovery according to the recommended depletion schedule. Blue curve shows the first 4 wells recovery within the initial 4 years, red curve shows the 8 wells recovery within 7 years, green curve shows all the wells (12 wells) recovery within the last 3 years.

3.5 Impact of Subsurface Uncertainty

We presented an infill well drilling sequence design for this tight gas reservoir model, and we account for the subsurface uncertainty by incorporating the uncertainty map into our proposed quality map. In the previous section, we show that the infill wells are more likely to be placed around the existing wells, since the data here are more reliable. However, if we do not consider the uncertainty, or assuming the data in this model are reliable, the sweet spots for well placement are often the un-depleted regions far from existing wells. In this section, we will compare the design of the drilling sequence, with and without this risk assessment, to study the impact of subsurface uncertainty.

Without considering the uncertainty, the infill well placement depends solely on the recovery potential, Eq. (3-6), or Eq. (3-7) when $a = 0$. Then we will compare the infill well placement at each stage, with and without the risk assessment. Here we still place 4 wells every 3 years, and the results that account for uncertainty are same with previous section.

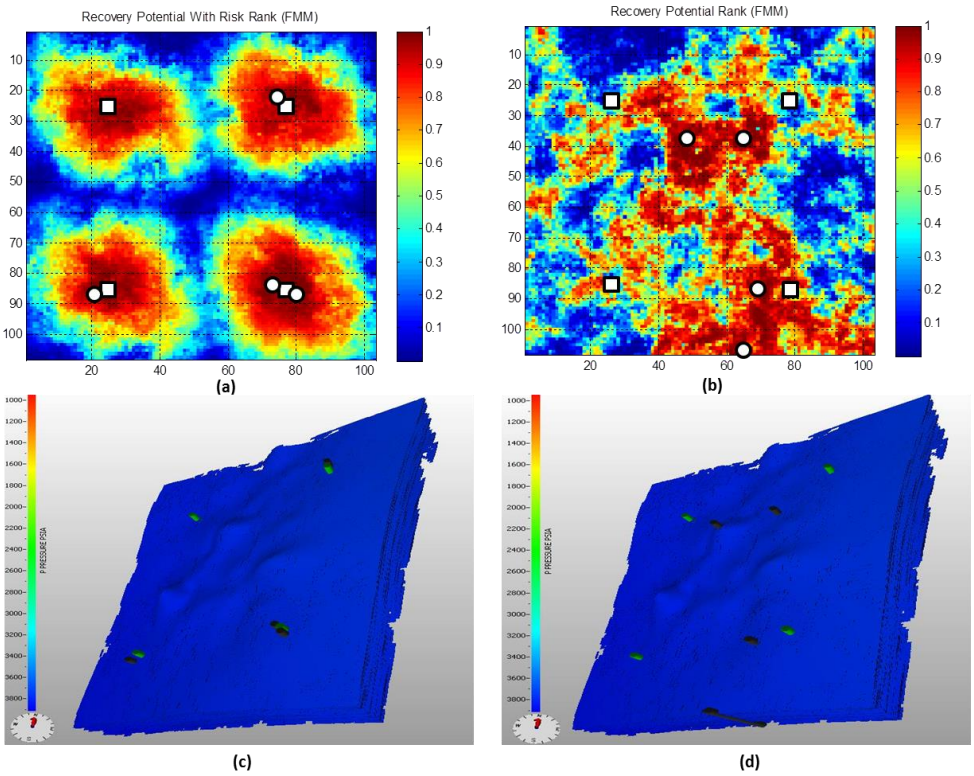

Figure 3-15: Infill well placement for the first development stage with and without uncertainty. (a): Recovery potential with risk map using Eq. (3-7); (b): Recovery potential map using Eq. (3-6). White square point marks the existing wells, and white round points mark the infill well locations; (c): Pressure profile for the infill wells with uncertainty at first development stage; (d): Pressure profile for the infill wells without uncertainty at first development stage.

Figure 3-15a has been discussed before, with the confidence from the 4 appraisal wells; the infill wells are placed at the neighborhood of the existing wells. Figure 3-15b shows the recovery potential map, here, the locations of infill wells are solely dependent on this quality map. Without uncertainty, the infill wells are chosen at the higher quality region. Two wells are at the center, and two wells are close to the bottom. All are far away from the existing wells, thus, become very risky. Note that the recovery potential map and recovery potential with risk map all need to be updated when every infill well is placed. The first stage, 4 appraisal wells are shut-in, therefore, the pressure all remains at initial pressure.

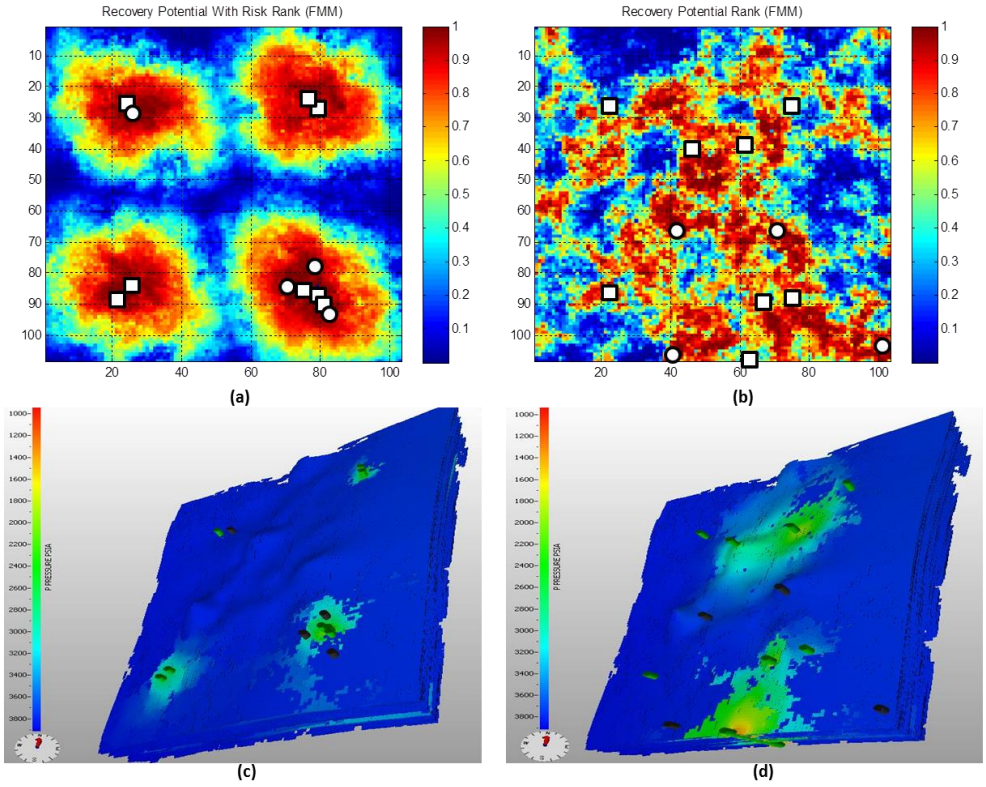

Figure 3-16: Infill well placement for the second development stage with and without uncertainty. (a): Recovery potential with risk map using Eq. (3-7); (b): Recovery potential map using Eq. (3-6). White square point marks the existing wells, and white round points mark the infill well locations; (c): Pressure profile for the infill wells with uncertainty at second development stage; (d): Pressure profile for the infill wells without uncertainty at second development stage.

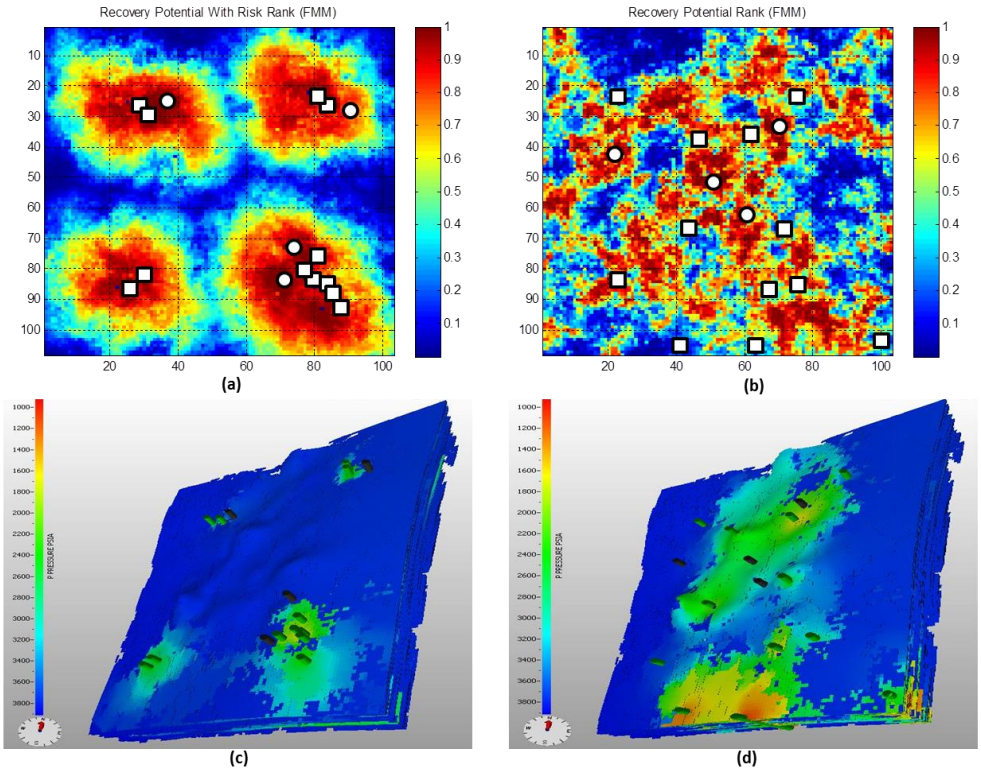

Figure 3-17: Infill well placement for the third development stage with and without uncertainty. (a): Recovery potential with risk map using Eq. (3-7); (b): Recovery potential map using Eq. (3-6). White square point marks the existing wells, and white round points mark the infill well locations. (c): Pressure profile for the infill wells with uncertainty at third development stage; (d): Pressure profile for the infill wells without uncertainty at third development stage.

Figure 3-16 and Figure 3-17 show a comparison of the infill well placement for the second and third development stage, with and without uncertainty. Without considering the uncertainty, the infill wells are more likely to spread out within the entire model, and far away from the existing wells, since these regions have the good recovery potential here. We can also find that the depleted volume would also be larger than that from the infill wells with uncertainty.

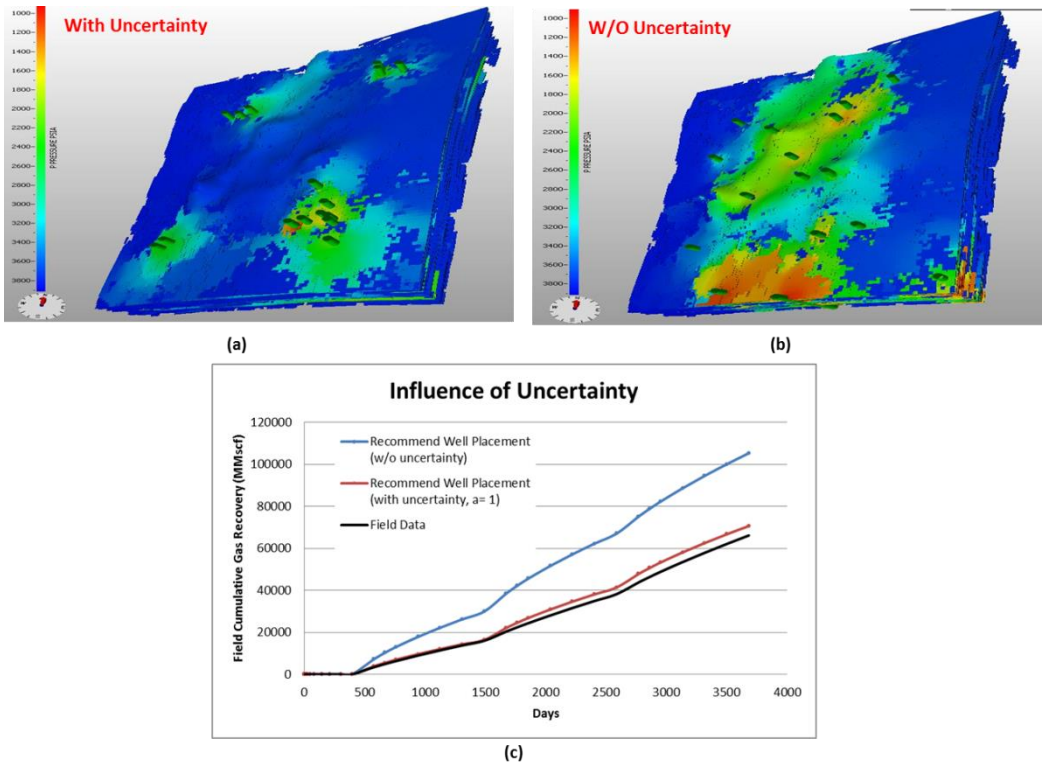

Figure 3-18: Influence of subsurface uncertainty on the depletion pattern and field recoveries. (a) Final pressure after 10 years depletion, when considering uncertainty; (b): Final pressure after 10 years depletion, without considering the uncertainty. (c): Cumulative recovery according to the different recommended depletion schedule. Blue curve is the infill wells without considering the uncertainty, and red curve is the infill wells with uncertainty. Also, the black curve is the exiting well locations from field data.

Figure 3-18 shows a comparison of the depletion patterns and field recoveries of infill wells, with and without uncertainty. As discussed, without considering the uncertainty, the infill wells are more likely to be at the regions that far away from the existing wells, since these regions have the good recovery potential here, the depleted volumes should be bigger and the recovery is also higher, compared to the infill wells with uncertainty. Also, as a comparison, Figure 3-18b also shows the field recovery of the wells from the field data, here, when we considering the subsurface uncertainty, our recommended infill wells would have similar recovery history with the field data, thus are more realistic. And without considering the uncertainty, the recommended infill wells have much higher recoveries, which may be too risky for the field management.

3.6 Comparison with the Uncertainty Assessment from Multiple Realizations

As discussed before, for the well placement optimization, since one realization cannot represent many combinations of the uncertainties, people tend to account for geologic uncertainty by using multiple plausible realizations , the optimum infill well location is determined based on the mean or expected value of all realizations (Da Cruz et al., 2004; Taware et al., 2012). This section will compare our uncertainty assessment from the variogram map, with the traditional uncertainty assessment from multiple realizations, to show the benefits of our method.

We build 10 geologic realizations using the petrophysical modeling workflow of Petrel (Petrel, 2011). In order to generate multiple realizations, 2 inputs are required in this workflow: the existing permeability logs for the 4 appraisal wells, and variogram information from the reference model, which is shown in Figure 3-10. Figure 3-19 shows the pay cell permeability of our reference model and the first 4 realizations in log scale.

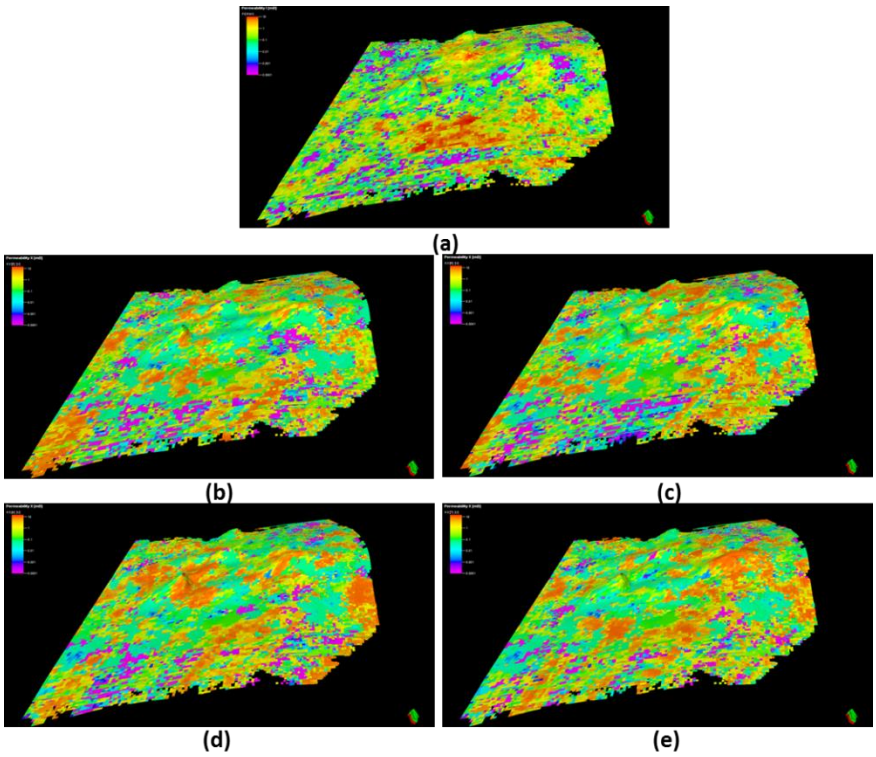

Figure 3-19: Permeability of our reference model and the first 4 realizations. (a): Permeability of our reference model; (b), (c), (d), (e) are the permeabilities of 4 realizations.

The permeability varies from 10-4~10 md in each of the models, pink cells are the low permeability cells, and red cells are the high permeability cells. The locations of fluvial channels and baffles change from one realization to another realization. We calculated the recovery potential of each realization, using Eq. (3-6), then the variance of each column in these 10 realizations can be obtained, which provide another method to access the geological uncertainty. Figure 3-20 provides a comparison of our uncertainty map from the variogram map, with the variance map from multiple realizations.

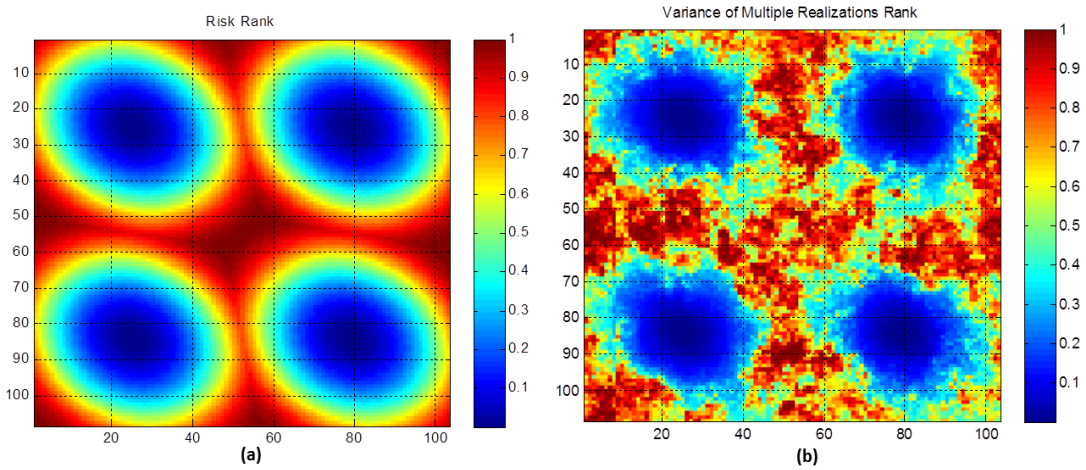

Figure 3-20: Comparison of the uncertainty assessments. (a): Uncertainty map from the variogram map; (b): Variance map from 10 realizations, the variance of each column is ranked and normalized.

Our uncertainty map has more smooth data, compared to the variance map, since it is generated from the fitted exponential variogram model. Both maps show a similar structure here, less uncertainty near the wells, and high uncertainty that far away from the wells, since they are built based on the same information: 4 appraisal well logs and variogram. Therefore, we validate our uncertainty assessment through the comparison with multiple realizations, which is more computational expensive.

To further study the influence of subsurface uncertainty on the recovery, we utilized the recommended well placement, with and without uncertainty, to check the cumulative gas recovery on each of the realizations. In additional, the gas recoveries on the original model are also included as the reference.

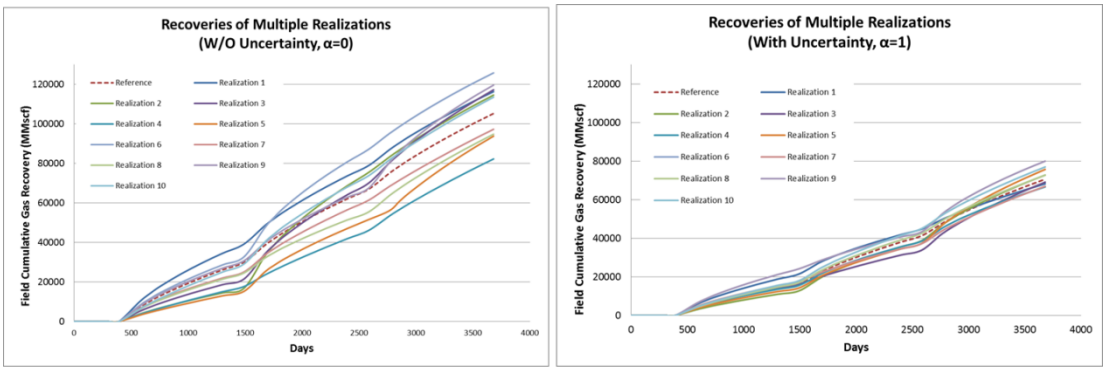

(a) (b)

Figure 3-21: Recoveries of multiple realizations with the recommended well placement. (a): Recoveries of multiple realizations when the infill wells are placed without considering the uncertainty; (b): Recoveries of multiple realizations when the infill wells are placed when the uncertainty is taken into account.

Figure 3-21 shows the recoveries of multiple realizations with the recommended well placement, with and without uncertainty. When the uncertainty is not taken into account, the infill well locations are more likely in the risky region, which is far away from the existing wells. More uncertainty occurs in such risky region. Therefore, we could expect a larger recovery variation. The recoveries from Figure 3-21a are about 78%~119% of the reference recovery. When the uncertainty is taken into account, the well locations are more likely close to the existing wells, which is a more reliable region. Therefore, the variation region of the recoveries here is smaller, which is about 89%~113% of the reference recovery. The proposed approach can be easily utilized to manage the uncertainty on the recovery prediction.

3.7 Conclusions

We present a simulation-free approach to determine the infill well placement effectively, based on the concept of recovery potential map and risk map. This approach can be utilized to design the development strategy for large scale field management by monitoring the dynamic changes of recovery potential map and uncertainty map during the depletion history. We utilize this workflow to study the impact of subsurface

uncertainty on an infill well drilling sequence and the recoveries in a large scale tight gas reservoir model.

The detailed conclusions can be summarized as following:

(1): We introduce and utilize a rapid simulation-free approach to approximate the pressure, and incorporate the pressure information into the proposed recovery potential to determine the infill well location. The recovery potential map we proposed shows a good correlation with the exhaustive flow simulations. From this map, we can infer the good infill well locations, or at least provide a good starting point for any optimization algorithm.

(2): We propose the uncertainty map to access the geologic uncertainty, and also incorporate the risk into the recovery potential to determine the infill well location, Eq. (3-7). The weight of the risk/confidence is chosen based on the degree of confidence in the static model. Subsurface uncertainty has significant influence on the well placement strategies, which cannot be neglected.

(3): We validate our uncertainty map through the comparison with the variance map, calculated from the multiple realizations. Therefore, the proposed uncertainty map provides a more efficient tool to access the geologic uncertainty.

(4): We compare the recoveries of multiple realizations, with and without uncertainty; the proposed approach can be easily utilized to manage the uncertainty on the recovery prediction, provide good opportunities for the field management.

(5): This approach does not require the flow simulation, for a multimillion cells model, the approach can quickly determine the infill well location within minutes, which is at least one order of magnitude CPU speed-up, compared to the

simulation work. The efficiency of this approach makes it feasible for large scale field application, as shown in the previous section.

However, due to the limitation of 2D maps, the approach can only consider the vertical well placement. Further studies on the well trajectory and fracture design are still required to develop the robust tight gas field development strategy.

4. IMPROVED GEOMETRIC PRESSURE SOLUTION

4.1 Introduction

Well test analysis, including pressure transient and rate transient analysis is widely used in unconventional resources to estimate reservoir properties and optimize hydraulic fracture design in unconventional reservoirs. Lee and Hopkins (1994) and Holditch (2006) showed flow regimes for a vertical well with hydraulic fracture. In shale gas reservoirs, Al-Kobaisi et al. (2006), Bello and Wattenbarger (2010), Clarkson et al. (2009) and Freeman et al. (2009) analyzed flow regimes for multi-stage transverse fractures. Al-Kobaisi et al. (2006) identified a pseudo-radial flow regime for a finite conductivity fracture system. Much of the current well test analysis can only provide the pressure depletion behavior and flow regimes in homogeneous or layered reservoirs. They are difficult to generalize to arbitrary reservoir conditions and well locations.

Xie et al. (2012) proposed a novel semi-analytical approach which can provide a rapid estimation of the reservoir drainage volume and the pressure and rate response, without a conventional numerical simulation. The Eikonal equation that governs the propagation of a pressure 'front' is first derived from diffusivity equation. Through the concept of depth of investigation, Eikonal equation and the Fast Marching Method (Appendix B) are utilized to calculate drainage volume. From drainage volume calculations, a generalized pressure solution based on a geometric approximation of the drainage volume could be acquired. A major advantage of this approach is that the Eikonal equation can be solved very efficiently using the Fast Marching Methods (FMM). Thus, transient pressure response can be obtained in multimillion cell geologic models in minutes without resorting to reservoir simulators. Our previous work about well placement also introduces this geometric pressure approximation to provide a rapid estimation of the pressure depletion behavior.

However, as we will show later, there is one inconsistency between the Fast Marching Method and the geometric pressure approximation. The Fast Marching Method can only provide the diffusive time of flight (τ) information, more specifically, the drainage volume vs. diffusive time of flight (τ) relationship. But geometric pressure approximation actually requires the relationship between drainage volume and actual time (t). This implies that a conversion between actual time (t) and diffusive time of flight (τ) is required. Gupta et al. (2012) proposed a simple conversion from diffusive time of flight (τ) and actual time (t) based on the analysis on symmetric flow in the homogeneous reservoir. However, such conversions cannot work in the heterogeneous reservoir. Furthermore, geometric pressure approximation assumes that the drainage volume acts as a moving no flow boundary, the pressure drop and flux are negligible beyond the drainage volume. Within the drainage volume, the pressure can be approximated by a steady state solution. Such assumptions also become the major limitations for accurate pressure approximation. They may provide a good relative pressure solution in a heterogeneous media, like we discussed in the well placement work. But, this approach cannot provide accurate pressure solution in the heterogeneous media.

To better understand the pressure behavior of the heterogeneous reservoirs, especially tight gas systems, we actually need to overcome the limitations of this pressure approximation method. The objective of this work is to introduce and evaluate an improved geometric pressure approximation in tight gas systems.

4.2 A Review of Previous Work

4.2.1 Eikonal Equation

Previous work relies on the definition of radius of investigation given by Lee (1982). Lee defines the radius of investigation as the propagation distance of a 'peak' pressure disturbance for an impulse source or sink. In heterogeneous reservoirs, since the pressure

front is not expected to be uniform in all directions, the term “depth of investigation”, instead of “radius of investigation”, is introduced. To obtain the depth of investigation, an asymptotic solution for the diffusivity equation has been obtained (Datta-Gupta and King 2007; Vasco et al. 2000).

The derivation begins with the three dimensional diffusivity equation for a heterogeneous system, shown as following:

$$\phi(x)\mu c_t \frac{\partial p(x,t)}{\partial t} = \nabla.\left(k(x)\nabla p(x,t)\right) \tag{4-1}$$

Where, $\phi(x)$ is porosity and $k(x)$ is permeability, we assume constant fluid properties, viscosity (μ) and compressibility (c_t).

Now, by applying a Fourier transform to this equation, it becomes the following in the frequency domain:

$$\phi(x)\mu c_t(-i\omega)\tilde{p}(x,\omega) = k(x)\nabla^2\tilde{p}(x,\omega) + \nabla k(x).\nabla\tilde{p}(x,\omega) \tag{4-2}$$

The asymptotic solution to this equation can be obtained by considering the following pressure solution in terms of inverse powers of $\sqrt{-i\omega}$.

$$\tilde{p}(x,\omega) = e^{-\sqrt{-i\omega}\tau(x)}\sum_{j=0}^{\infty}\frac{A_j(x)}{\left(\sqrt{-i\omega}\right)^j} \tag{4-3}$$

where, $\tau(x)$ is the Diffusive Time of Flight, which denotes the propagation time of the pressure ‘front’, and $A_j(x)$ the pressure amplitude at the j-th order. The leading order high frequency term in the asymptotic expansion determines the pressure front propagation, as following.

$$\tilde{p}(x,\omega) = A_o(x)e^{-\sqrt{-i\omega}\tau(x)} \tag{4-4}$$

By substituting this solution in Eq. (4-2) and collecting the terms with the highest order of $i\omega$. Eq. (4-5) can be obtained for the pressure front propagation.

$$\sqrt{\alpha(x)}\left|\nabla \tau(x)\right| = 1 \tag{4-5}$$

Here α(x) stands for diffusivity and can be defined as:

$$\alpha(x) = \frac{k(x)}{\phi(x)\mu c_t} \tag{4-6}$$

The above equation is in the form of an Eikonal equation and indicates that the pressure front propagates in the reservoir with a velocity of the square root of diffusivity α(x). Also, diffusive time of flight, τ(x) has unit of square root of time which is consistent with scaling behavior of pressure diffusion. The pressure 'front' propagation depends on reservoir and fluid properties and is independent of flow rate.

4.2.2 Depth of Investigation for Symmetric Flow

The conversion from diffusive time of flight (τ) to actual physical time (t) could be acquired from the depth of investigation. Gupta et al. (2012) proposed a simple derivation of the depth of investigation based on the analysis on symmetric flow in the homogeneous reservoir. τ(x) is related to physical time through a simple expression of the form $t(x) = \frac{\tau(x)^2}{c}$ where the pre-factor c depends on the specific flow geometry. For example, for linear flow, c = 2, for radial flow, c = 4 and for spherical flow, c = 6.

For a homogeneous reservoir with constant rock properties (porosity, permeability, reservoir thickness and rock compressibility) and single phase fluid with constant properties (viscosity and compressibility), the diffusivity equation in terms of pressure (p) and Darcy flux (q) can be written as following:

$$A\phi c_t \frac{\partial p}{\partial t} = \frac{\partial q}{\partial r} \tag{4-7}$$

The flux term, q is defined by Darcy's law

$$q = \frac{kA}{\mu}\frac{\partial p}{\partial r} \tag{4-8}$$

Where, A is the cross sectional area for flow (radially symmetrical); p is the pressure at any location and q is Darcy flux. Symmetrical flow in 1D is linear flow, $r = |x|$, and $A = Constant$; for 2D is cylindrical flow, $r^2 = x^2 + y^2$, and $A = 2\pi rh$; for 3D is spherical flow, $r^2 = x^2 + y^2 + z^2$, and $A = 4\pi r^2$; The flow cross sectional area for a symmetric flow can be simplified as written in the form of $A = A_0 r^n$, where n= 0, 1, 2 for linear, cylindrical and spherical flow respectively.

The diffusivity equation can be written in terms of pressure:

$$\frac{\phi\mu c_t}{k}\frac{\partial p}{\partial t} - \frac{1}{A}\frac{\partial}{\partial r}\left(A\frac{\partial p}{\partial r}\right) = 0 \tag{4-9}$$

Or in terms of the flux:

$$\frac{\phi\mu c_t}{k}\frac{\partial q}{\partial t} - A\frac{\partial}{\partial r}\left(\frac{1}{A}\frac{\partial q}{\partial r}\right) = 0 \tag{4-10}$$

The initial and boundary conditions are not discussed in this section. Here, to simplify Eq. (4-10), Boltzmann variable, ξ, as the independent variable, defined as:

$$\xi = \frac{r^2}{4T} \tag{4-11}$$

Where, $T = \dfrac{kt}{\phi\mu c_t}$, it has units of (Length)^2.

For symmetric flow, Darcy flux solely in terms of the Boltzmann variable, $q(\xi)$. The time derivative term of Eq. (4-10) becomes:

$$\frac{\phi\mu c_t}{k}\frac{\partial q}{\partial t} = \frac{\partial q}{\partial T} = \frac{\partial \xi}{\partial T}\frac{dq}{d\xi} = -\frac{r^2}{4T^2}\frac{dq}{d\xi} = -\frac{\xi}{T}\frac{dq}{d\xi} \tag{4-12}$$

And the spatial derivative becomes:

$$\frac{\partial}{\partial r} = \frac{\partial \xi}{\partial r}\frac{\partial}{\partial \xi} = \frac{r}{2T}\frac{\partial}{\partial \xi} \tag{4-13}$$

We have defined flow cross sectional area $A = A_n \cdot r^n$, $n = 0,1,2$, then the spatial derivative term of Eq. (4-10) becomes:

$$A\frac{\partial}{\partial r}\left(\frac{1}{A}\frac{\partial q}{\partial r}\right) = r^n \frac{\partial}{\partial r}\left(\frac{1}{r^n}\frac{\partial q}{\partial r}\right) = \frac{1}{4T^2} r^{1+n}\frac{\partial}{\partial \xi}\left(r^{1-n}\frac{\partial q}{\partial \xi}\right) = \frac{1}{4T^2}(4\xi T)^{(1+n)/2}\frac{\partial}{\partial \xi}\left((4\xi T)^{(1-n)/2}\frac{dq}{d\xi}\right)$$
$$= \frac{1}{T}\xi^{(1+n)/2}\frac{\partial}{\partial \xi}\left(\xi^{(1-n)/2}\frac{dq}{d\xi}\right) \tag{4-14}$$

If we introduce $m = (n-1)/2 = -\frac{1}{2}, 0, \frac{1}{2}$, then Eq. (4-14) becomes:

$$\frac{1}{T}\xi^{m+1}\frac{d}{d\xi}\left(\xi^{-m}\frac{dq}{d\xi}\right) \tag{4-15}$$

Combine Eq. (4-10), Eq. (4-12) and Eq. (4-15), equation (10) becomes:

$$0 = -\frac{\xi}{T}\frac{dq}{d\xi} - \frac{\xi^{m+1}}{T}\frac{d}{d\xi}\left(\xi^{-m}\frac{dq}{d\xi}\right) \tag{4-16}$$

This could be further simplified as:

$$0 = \left(1 - \frac{m}{\xi}\right)\frac{dq}{d\xi} + \frac{d^2q}{d\xi^2} \tag{4-17}$$

The radius of investigation can be obtained by solving for the maximum pressure derivative $\frac{\partial p}{\partial T}$, we have:

$$\frac{\partial p}{\partial T} = \frac{\phi\mu c_t}{k}\frac{\partial p}{\partial t} = \frac{\mu}{Ak}\frac{\partial q}{\partial r} = \frac{\mu}{Ak}\frac{\partial \xi}{\partial r}\frac{dq}{d\xi} = \frac{\mu}{Ak}\frac{r}{2T}\frac{dq}{d\xi} \tag{4-18}$$

Combine Eq. (4-17) and Eq. (4-18), we can calculate the second derivative of pressure, which is:

$$\frac{\partial^2 p}{\partial T^2} = -\left(\frac{\mu r}{2kAT^2}\right)\left(\frac{dq}{d\xi}\right)(1 + m - \xi) \tag{4-19}$$

Maximize the first derivative implies that the second derivative should be zero. Thus we have:

$$1 + \mathrm{m} - \xi = 0 \tag{4-20}$$

and

$$T = \frac{r^2}{2(n+1)} \tag{4-21}$$

For symmetric homogeneous cases, the Eikonal equation can be written as:

$$r = \frac{\tau}{\sqrt{\frac{\phi\mu c_t}{k}}} \tag{4-22}$$

Combine Eq. (4-21) and Eq.(4-22), we can have:

$$t = \frac{\tau^2}{2(n+1)} \tag{4-23}$$

Thus: we can get 1D linear flow, $n = 0$, and $t = \frac{\tau^2}{2}$; for 2D cylindrical flow, $n = 1$, and $t = \frac{\tau^2}{4}$; for 3D spherical flow, $n = 2$, and $t = \frac{\tau^2}{6}$;

4.3 Improved Pressure Approximation Method

As discussed before, simple conversion from diffusive time of flight (τ) and actual time (t) based on the analysis on symmetric flow in the homogeneous reservoir cannot work in the heterogeneous reservoir. Furthermore, the assumptions of geometric pressure approximation are also the major limitations for accurate pressure approximation.

In order to overcome such limitations, we still need to go back to check our diffusivity equation for a heterogeneous system, shown as Eq. (4-1). The equation in frequency domain through Fourier transform can be obtained as Eq. (4-2). And the leading order high frequency term of the asymptotic solution is $\tilde{p}(x, \omega) = A_o(x) e^{-\sqrt{-i\omega}\tau(x)}$, as Eq. (4-4) shows, $A_o(x)$ is the amplitude of the leading order term.

Taking the inverse Fourier transform of the Eq. (4-4), we can get the leading order term solution in the time domain expression (Virieux et al., 1994). The solution in 3D for an impulse source (delta function) is:'

$$p(x, t) = A_o(x) \frac{\tau}{2\sqrt{\pi t^3}} e^{-\frac{\tau^2}{4t}} \tag{4-24}$$

And for a constant rate source (Heaviside function), the solution becomes:

$$\frac{\partial p(x, t)}{\partial t} = A_o(x) \frac{\tau}{2\sqrt{\pi t^3}} e^{-\frac{\tau^2}{4t}} \tag{4-25}$$

Similarly, in 2D, leading order term solution in the time domain is:

$$\frac{\partial p(x,t)}{\partial t} = A_o(x)\frac{\tau}{2\sqrt{\pi t^2}}e^{-\frac{\tau^2}{4t}} \tag{4-26}$$

In 1D, the solution would be:

$$\frac{\partial p(x,t)}{\partial t} = A_o(x)\frac{\tau}{2\sqrt{\pi t}}e^{-\frac{\tau^2}{4t}} \tag{4-27}$$

The diffusion solution in 3D/2D/1D has the same power exponent part, but it also exhibits a time decrease of $1/\sqrt{t^3}$ which is converted in a $1/t$ decrease in the 2D case and $1/\sqrt{t}$ in the 1D case.

For 3D symmetric homogeneous case, we have the diffusion equation in term of pressure as Eq. (4-9). By introducing the Eikonal equation, Eq. (4-22), the diffusion equation can be further simplified as:

$$\frac{\partial p}{\partial t} = \frac{1}{\tau^2}\frac{\partial}{\partial \tau}\left(\tau^2\frac{\partial p}{\partial \tau}\right) \tag{4-28}$$

Then we plug the diffusion solution in 3D into Eq. (4-28), we have the following relationship for the amplitude:

$$A_o = -A_o'\tau \tag{4-29}$$

And:

$$A_o' = -\frac{A_o'' \tau}{2} \tag{4-30}$$

Similarly, we can also plug the diffusion solution in 2D and 1D into its corresponding diffusion equation, the relationship of Eq. (4-29) and Eq. (4-30) are still valid.

From Eq. (4-29) and Eq. (4-30), we can predict that the amplitude should have such expression:

$$A_o \tau = B \tag{4-31}$$

Where, B is independent of τ.

Therefore, the diffusion solution in 3D, 2D and 1D case become:

$$\frac{P(x,t)}{\partial t} = B \frac{1}{2\sqrt{\pi t^n}} e^{-\frac{\tau^2}{4t}} \tag{4-32}$$

Where, n=3, 2, 1 for in 3D, 2D and 1D case.

From the geometric pressure approximation, we also know that the pressure depletion within the drainage volume as:

$$c_t \frac{\partial p}{\partial t} = \frac{\partial q}{\partial V_p} \approx -\frac{q_w}{V_p(t)} \tag{4-33}$$

Through the analogical reasoning of Eq. (4-32) and Eq. (4-33), we introduce an improved pressure approximation solution, as:

$$c_t \frac{\partial p}{\partial t} = \frac{\partial q}{\partial V_p} \approx -\frac{q_w}{V_p(t)} e^{-\tau^2/4t} \tag{4-34}$$

The underlying assumptions imply that Eq. (4-33) only works within the drainage boundary (depth of investigation), and beyond that, we assume no flux or pressure drop. But Eq. (4-34) allows the pressure and flux vary smoothly at the depth of investigation. Furthermore, the dimensional analysis also validates the Eq. (4-34) when compared to Eq. (4-32).

From Eq. (4-34), we can have the flux expressed as:

$$q(\tau, t) = \frac{q_w}{V_p(t)} \int_{V_p(\tau)}^{\infty} dV_p \cdot e^{-\tau^2/4t} = \frac{q_w}{V_p(t)} \int_{V_p(\tau)}^{\infty} d\tau \frac{dV_p}{d\tau} e^{-\tau^2/4t} \tag{4-35}$$

The boundary condition at the wellbore ($V_p = 0, q = q_w$) now provides the equation for $V_p(t)$:

$$V_p(t) = \int_0^{\infty} dV_p \cdot e^{-\tau^2/4t} = \int_0^{\infty} d\tau \frac{dV_p}{d\tau} e^{-\tau^2/4t} \tag{4-36}$$

We also can calculate the depth of investigation by take the maximum value of the first derivative, which means, second derivative should be zero.

$$0 = \left\{ \frac{1}{V_p(t)^2} \frac{dV_p}{dt} - \frac{1}{V_p(t)} \frac{\tau^2}{4t^2} \right\} e^{-\tau^2/4t} \tag{4-37}$$

Therefore, the conversion of diffusive time of flight (τ) and actual time (t) can be obtained as:

$$\tau^2 = \frac{4t^2}{V_p(t)} \frac{dV_p}{dt} \tag{4-38}$$

From Eq. (4-36), we have:

$$\frac{dV_p(t)}{dt} = \int_0^\infty dV_p \cdot \frac{\tau^2}{4t^2} \cdot e^{-\tau^2/4t} \tag{4-39}$$

Hence:

$$\tau^2 = \int_0^\infty dV_p \cdot \tau^2 \cdot e^{-\tau^2/4t} \Big/ \int_0^\infty dV_p \cdot e^{-\tau^2/4t} \tag{4-40}$$

Note that this general conversion can be simplified as the symmetric homogenous case in 3D, 2D and 1D, using the $V_p \propto \tau^n$, $n = 3, 2, 1$.

4.4 Case Study

We have derived the improved pressure approximation method, and from which, we also obtained the conversion of diffusive time of flight (τ) and actual time (t) in heterogeneous reservoirs. In this section, we will compare the new method with the previous method and the simulation results through a conceptual case study.

A 2D heterogeneous reservoir model is built to compare the new method with previous method and the simulation results, following are the properties of this conceptual model:

Property		Value	Unit
Reservoir	Porosity	0.20515	fraction
	Number of Grids	100x100x1	
	Grid Size	25x25x100	ft^3
	Thickness	100	ft
	Initial Pressure	5000	psi
Fluid	Viscosity	1	cp
	Oil FVF	1	
	Total Compressibility	3.00E-06	1/psi
Well	Well Radius	0.3	ft
	Well Rate	1	bbl/day

Table 3: Properties of the 2D conceptual model

This conceptual model has the homogenous porosity, but with the heterogeneous permeability. Figure 4-1 shows the permeability distribution in log scale.

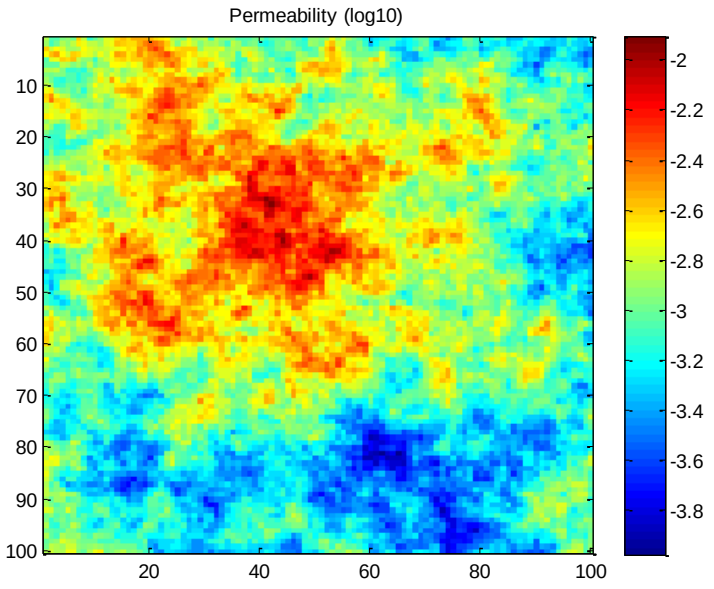

Figure 4-1: The permeability distribution (log scale) of the conceptual model

The top left and central region is basically the high permeability region, and bottom region is the low permeability region, and the well is located in the center of this model. Figure 4-2 shows the diffusive time of flight, calculated by the Fast Marching Method.

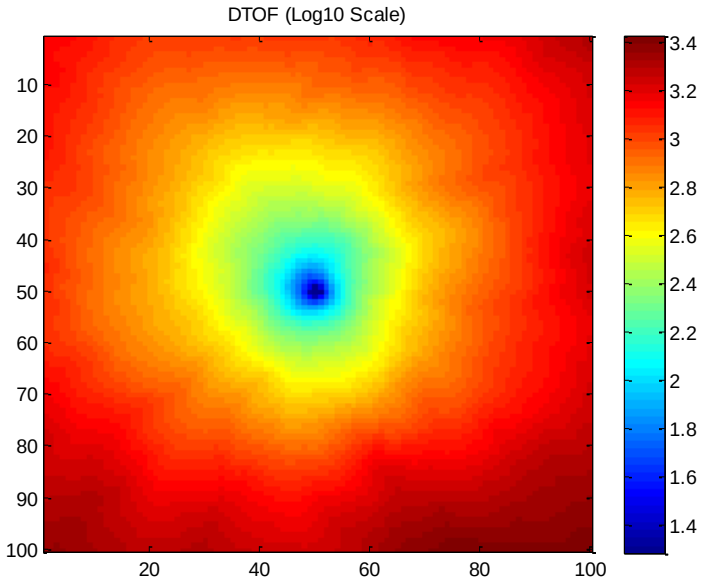

Figure 4-2: Diffusive time of flight (log scale) of the conceptual model

The central region has the smaller diffusive time of flight, since the pressure propagation starts from the central point. On the contrary, the four corners should have the bigger diffusive time of flight due to the longer distance to the pressure impulse. The top left corner's diffusive time of flight is smaller than the other corners, due to the high permeability in this region.

From Figure 4-2, the drainage volume could be calculated by setting the different cut off values of diffusive time of flight, which is shown in Figure 4-3:

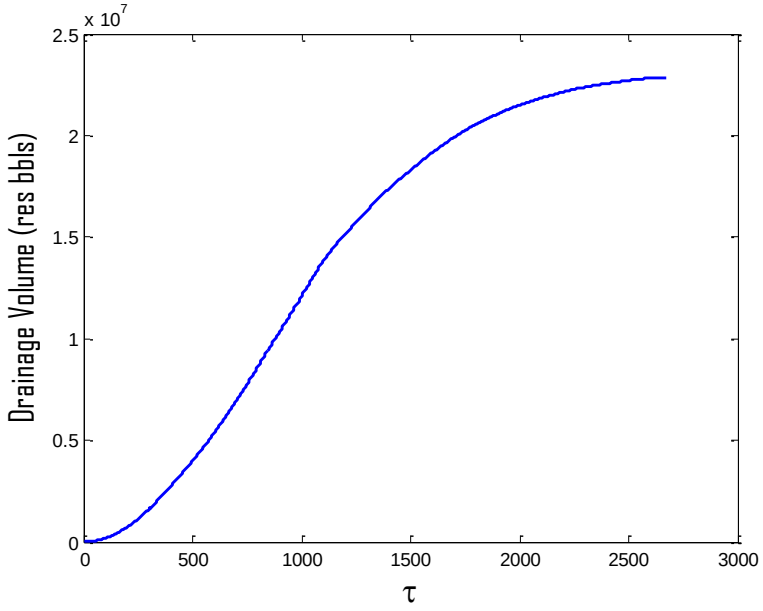

Figure 4-3: Drainage volume vs. the diffusive time of flight

The diffusive time of flight could be converted into actual time next to get the relationship of drainage volume and the actual physical time.

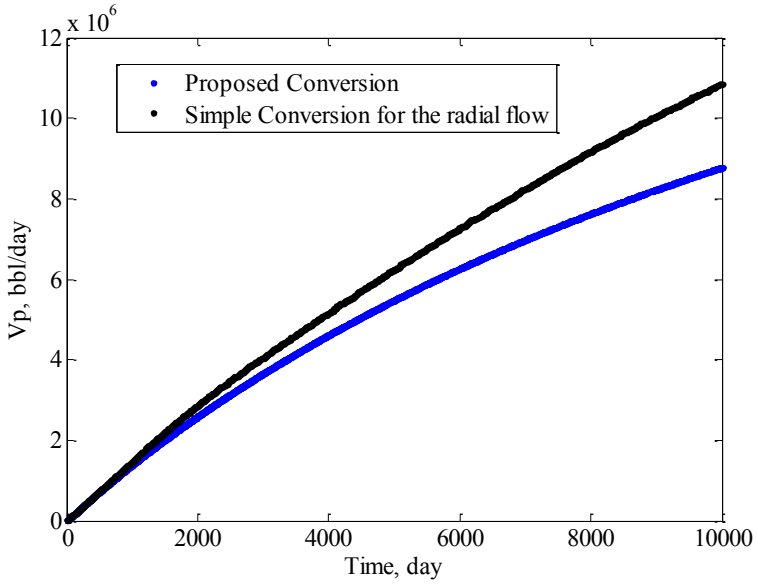

Figure 4-4: Drainage volume vs. time, the time is converted from different methods

Figure 4-4 shows a comparison of the actual time, which is converted from the simple algebra, $t = \frac{\tau^2}{4}$, by assuming the radial flow, and the proposed conversion, using Eq. (4-40). Here, we could find that if we assume the radial flow, the time we estimated will be too early for the heterogeneous reservoir.

Figure 4-5 shows a detailed comparison of the pressure propagation arrival time, here, the simulation results from Eclipse are also presented as the reference.

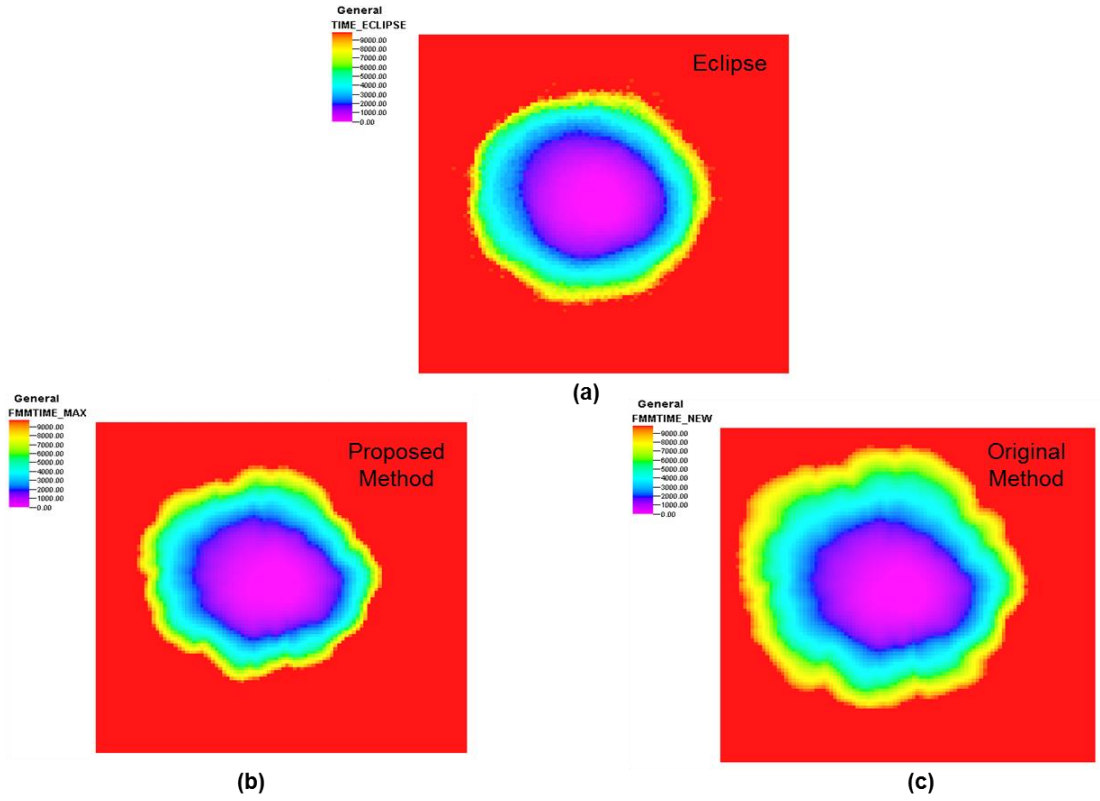

Figure 4-5: The pressure propagation arrival time contour. (a): The arrival time is calculated from Eclipse simulation. (b): The arrival time is calculated using the proposed conversion Eq. (4-39). (b): The arrival time is calculated by assuming the radial flow.

Figure 4-5b shows a good match with the Figure 4-5a, the simulation results, which validates our proposed conversion in the heterogeneous reservoir. While, compared to Figure 4-5a, Figure 4-5c shows a wider region of the smaller arrival time. This is consistent with our analysis in Figure 4-4, the arrival time we estimated will be too early for the heterogeneous reservoir, if we assume the radial flow.

Figure 4-6 shows another comparison of the arrival time in the cross plots.

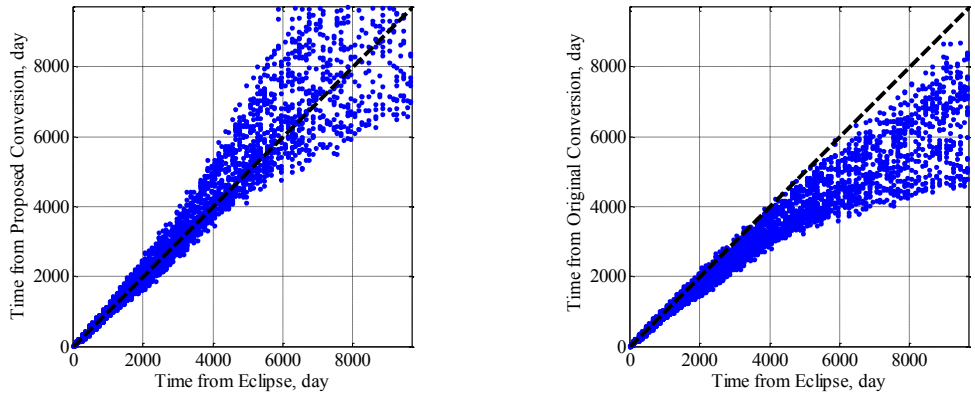

(a) **(b)**

Figure 4-6: The arrival time comparison in the cross plots. (a): The arrival time from proposed conversion vs. the arrival time from Eclipse simulation. (b): The arrival time from original conversion by assuming radial flow vs. the arrival time from Eclipse simulation.

Figure 4-6a shows the arrival time from proposed conversion vs. the arrival time from Eclipse simulation, even though we have the numerical noise from the proposed conversion, but the scatter is basically aligned with the 45 degree line in the cross plot, thus, the proposed conversion can get the correct arrival time that match with the simulation results.

Figure 4-6b shows the arrival time from original conversion by assuming radial flow vs. the arrival time from Eclipse simulation, the scatter is aligned with the 45 degree line initially, and then began to deviate from 45 degree line at the later time. From here, we can see the radial flow assumption is valid at the early time, but at the later time, it is no longer valid.

Figure 4-7 shows the comparison of bottom hole pressure. The bottom hole pressure is calculate from the reservoir simulation, and the improved pressure approximation, Eq. (4-24) and the original pressure approximation, Eq.(3-4).

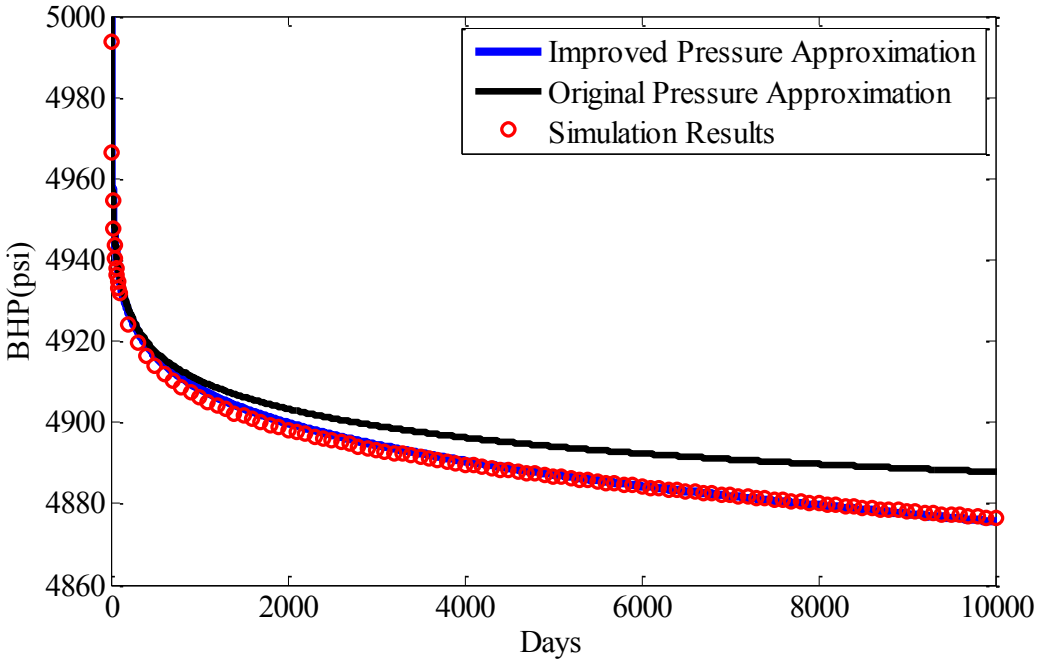

Figure 4-7: Bottom hole pressure comparison

In Figure 4-7, red points are the simulation results, and blue line is the bottom hole pressure at different times, which is calculated from Eq. (4-24). We could see the improved pressure approximation method could provide a very accurate pressure approximation. However, the original pressure approximation, which is the black line, cannot match with the simulation results. The pressure is also accurate at early time, but is then overestimated at later time, when the influence of heterogeneity occurs.

4.5 Conclusions

We present an improved pressure approximation method, through the comparison with the leading order high frequency term of the asymptotic solution and the unit analysis. For this approximation, the pressure and flux vary smoothly at the depth of investigation, instead of having different governing equations within, at, and beyond the depth of investigation in the original approximation method. From the improved approximation,

we can also derive the general conversion of the diffusive time of flight (τ) and pressure impulse actual time (t). The general conversion and improved geometric approximation can be applied in the heterogeneous reservoir, with any flow regimes. The detailed conclusion and discussions can be summarized as below:

1) The original conversion of the diffusive time of flight (τ) and pressure impulse actual time (t) relies on the analysis of the symmetric flow in homogeneous reservoir. Directly apply such conversion in the heterogeneous reservoir can lead to inaccurate estimation of the arrival time, pressure and flux. On the contrary, the proposed conversion can account for the influence of the reservoir heterogeneity, and can also be simplified as the original conversions in the homogenous reservoir.

2) The original geometric pressure approximation assumes pseudo steady state pressure depletion behavior within the drainage boundary (depth of investigation), and beyond that, we assume no flux or pressure drop. But the improved pressure solution allows the pressure and flux vary smoothly at the depth of investigation, which should be more accurate.

3) Through the comparison with the simulation results, based on a 2D conceptual model, improved pressures approximation can obtain more accurate pressure impulse arrival time and bottom hole pressure. The original pressure approximation can only provide accurate solutions at earlier time, when the influence of heterogeneity has not occurred yet.

However, we also realized that the improved geometric pressure solution is still based on the first wave arrival concept, which means we do not account the influence of reflected pressure waves. But when the contrast in the reservoir properties in heterogeneous

reservoirs is big, the influence of reflected pressure waves should be taken into consideration when applying this approximation (Gupta et al., 2012).

5. CONCLUSIONS & FUTURE WORK

With the increasing importance of unconventional gas resources, they also pose very challenging questions for the reservoir engineers, compared to the conventional resources. The current techniques, like layer-based upgridding & upscaling, pressure transient analysis, are quite mature and successful for conventional reservoirs. However, such techniques cannot work for tight gas resources due to its complex spatial pattern of partially or intermittently connected fluvial sand packages within a non-pay background, interactions between wells and fractures, complex reservoir dynamic responses which associated with depletion history, and also the geological subsurface uncertainties.

This work proposed some novel techniques for the upgridding & upscaling in tight gas reservoir simulation, efficient well placement in tight gas reservoir management, and the improved pressure approximation solution for heterogeneous reservoirs, which can also apply in the tight gas reservoirs. Such techniques are proved to work efficiently in tight gas reservoirs, thus, provide good opportunities for tight gas reservoir simulation and management.

However, each part of our research work also leave some open questions, that may require further investigations to improve the potential of the proposed techniques. Therefore, we also provide some suggestions for the future work in this section.

5.1 Conclusions

We first developed novel techniques for robust upscaling of tight gas reservoir models through the concept of diffusive time of flight. We design the fixed areal and variable vertical resolution, which is adapted to honor the continuity of the reservoir sands. We use the high resolution transmissibility based upscaling of flow properties to preserve the 3D flow tortuosity. Based on this concept, 3 successful upgridding & upscaling strategies are proposed, and which are proved to be more effective than current layer based upgridding techniques.

1) 1x1xN adaptive coarsening will preserve the connectivity of pay cells and barriers of non-pay cells. With the use of well index and transmissibility upscaling, it will generate upscaled model which can preserve internal reservoir heterogeneity with the minimum cell count.

2) Even better simulation performance is obtained with 2x2xN adaptive coarsening where over a factor of 10 CPU time reduction has been achieved. However, 2x2xN coarsening may not preserve all of the lateral barriers, especially those associated with large diffusive time. The simulation results are not as accurate as those for 1x1xN adaptive coarsening.

3) 3x3xN adaptive coarsening could further achieve a factor of 20 CPU time reduction. But it has a higher chance to lose the lateral barriers, thus, produce a relatively large error. However 2x2xN, and 3x3xN coarsening provide a very good options if we do not have a strict requirement for the accuracy.

We also designed the 3D adaptive coarsening to preserve the reservoir sands continuity and barriers. However, due to the limitation of cell geometry and corresponding upscaling issue, we cannot apply this technique to large scale tight gas field. Further investigation is still required.

We then introduced a simulation-free approach to determine the infill well placement effectively. This approach can be utilized to design the development strategy for large scale field management by monitoring the dynamic changes of recovery potential map and uncertainty map during the depletion history. We utilize this workflow to study the impact of subsurface uncertainty on an infill well drilling sequence and the recoveries in a large scale tight gas reservoir model.

The detailed conclusions can be summarized as following:

(1): We introduce and utilize a rapid simulation-free approach to approximate the pressure, and incorporate the pressure information into the proposed recovery potential to determine the infill well location. The recovery potential map we proposed shows a good correlation with the exhaustive flow simulations. From this map, we can infer the good infill well locations, or at least provide a good starting point for any optimization algorithm.

(2): We propose the uncertainty map to access the geologic uncertainty, and also incorporate the risk into the recovery potential to determine the infill well location, Eq. (3-7). The weight of the risk/confidence is chosen based on the degree of confidence in the static model. Subsurface uncertainty has significant influence on the well placement strategies, which cannot be neglected.

(3): We validate our uncertainty map through the comparison with the variance map, calculated from the multiple realizations. Therefore, the proposed uncertainty map provides a more efficient tool to access the geologic uncertainty.

(4): We compare the recoveries of multiple realizations, with and without uncertainty; the proposed approach can be easily utilized to manage the uncertainty on the recovery prediction, provide good opportunities for the field management.

(5): This approach does not require the flow simulation, for a multimillion cells model, the approach can quickly determine the infill well location within minutes, which is at least one order of magnitude CPU speed-up, compared to the simulation work. The efficiency of this approach makes it feasible for large scale field application, as shown in the previous section.

However, due to the limitation of 2D maps, the approach can only consider the vertical well placement. Further studies on the well trajectory and fracture design are still required to develop the robust tight gas field development strategy.

In the end, we present an improved pressure approximation method, through the comparison with the leading order high frequency term of the asymptotic solution and the unit analysis. For this approximation, the pressure and flux vary smoothly at the depth of investigation, instead of having different governing equations within, at, and beyond the depth of investigation in the original approximation method. From the improved approximation, we can also derive the general conversion of the diffusive time of flight (τ) and pressure impulse actual time (t). The general conversion and improved geometric approximation can be applied in the heterogeneous reservoir. The detailed conclusion and discussions can be summarized as below:

1) The original conversion of the diffusive time of flight (τ) and pressure impulse actual time (t) relies on the analysis of the symmetric flow in homogeneous reservoir. Directly apply such conversion in the heterogeneous reservoir can lead to inaccurate estimation of the arrival time, pressure and flux. On the contrary, the proposed conversion can account for the influence of the reservoir heterogeneity, and can also be simplified as the original conversions in the homogenous reservoir.

2) The original geometric pressure approximation assumes pseudo steady state pressure depletion behavior within the drainage boundary (depth of investigation), and beyond that, we assume no flux or pressure drop. But the improved pressure solution allows the pressure and flux vary smoothly at the depth of investigation, which should be more accurate.

3) Through the comparison with the simulation results, based on a 2D conceptual model, improved pressure approximation can obtain more accurate pressure impulse arrival time and bottom hole pressure. The original pressure approximation can only provide accurate solutions at earlier time, when the influence of heterogeneity has not occurred yet.

However, we also realized that the improved geometric pressure solution is still based on the first wave arrival concept, which means we do not account the influence of reflected pressure waves. But when the contrast in the reservoir properties in heterogeneous reservoirs is big, the influence of reflected pressure waves should be taken into consideration when applying this approximation (Gupta et al., 2012).

5.2 Future work

To further improve the potential of our proposed techniques, some additional work may be required in the following areas:

1) We tried an integrate design of the vertical and horizontal adaptive coarse grid to preserve the reservoir sands continuity and barriers. Such simulation grid could achieve the maximum simulation speed-up with the minimum cell count, without losing too much accuracy, since it still preserve the reservoir fundamental heterogeneity. However, we have not find an effective upscaling method that can works for the arbitrary cell geometry. Future work to develop accurate upscaling method on the arbitrary cell geometry is required.

2) We proposed the simulation-free approach for well placement in tight gas reservoirs. However, due to the limitation of 2D maps, the approach can only consider the vertical well placement. Further studies on the well trajectory and fracture design are still required to develop the robust tight gas field development

strategy. Also, current work assuming the drilling cost for every well is same, future work can also take more realistic economic factors into considerations.

3) The improved geometric pressure approximation is proposed for the heterogeneous reservoirs, but only when the reservoir with smooth varying properties. Since we only consider first wave arrival, and do not account the influence of reflected pressure waves. But when the contrast in the reservoir properties in heterogeneous reservoirs is big, the influence of reflected pressure waves should be taken into consideration when applying this approximation. Additional work about incorporate the reflected pressure into pressure approximation is still required. Also, we only apply the proposed method in a conceptual model; more field studies should be tested for the field applications.

REFERENCES

Al-Kobaisi, M., Ozkan, E., Kasogi, H., and Ramirez, B. 2006. Pressure-Transient Analysis of Horizontal Wells with Transverse, Finite-conductivity Fractures. PETSOC 2006-126 presented at Canadian International Petroleum Conference, Calgary, Alberta.

Bello, R. O., Wattenbarger, R. A. 2010. Multi-stage Hydraulically Fractured Shale Gas Rate Transient Analysis, paper presented at SPE North Africa Technical Conference and Exhibition, Cairo, Egypt. 126754.

Centilmen, A., Ertekin, T., Grader, A. 1999. Applications of Neural Networks in Multiwell Field Development. Paper presented at the SPE Annual Technical Conference and Exhibition, Houston, Texas. 56433.

Chen, Y., Bernath, A., Rai, H. and Muron, P. 2009. Development and Application of Upscaling Techniques for Modeling near-Well Flow in Heterogeneous Reservoirs. Paper presented at the SPE Annual Technical Conference and Exhibition, New Orleans, Louisiana. 124955.

Chen, Y., Durlofsky, L.J., Gerritsen, M. et al. 2003. A Coupled Local-Global Upscaling Approach for Simulating Flow in Highly Heterogeneous Formations. *Advances in Water Resources* 26 (10): 1041-1060.

Chen, Y. and Wu, X.-H. 2008. Upscaled Modeling of Well Singularity for Simulating Flow in Heterogeneous Formations. *Computational Geosciences* 12: 29-45.

Clarkson, C. R., Jordan, C. L., Ilk, D. and Blasingame, T. A. 2009. Production Data Analysis of Fractured and Horizontal CBM Wells. paper presented at SPE Eastern Regional Meeting. Charleston, West Virginia. 125929.

Da Cruz, P.S., Horne, R.N., Deutsch, C.V. 2004. The Quality Map: A Tool for Reservoir Uncertainty Quantification and Decision Making. Paper SPE 87642, *SPE Reservoir Evaluation & Engineering*, February, 6-14.

Datta-Gupta, A. and King, M.J. 2007. *Streamline Simulation: Theory and Practice.* SPE Textbook Series. 222, Palisades Creek Drive, Richardson, TX, 75080-2040 USA: Society of Petroleum Engineers. Original edition.

Ding, Y. 1995. Scaling-up in the Vicinity of Wells in Heterogeneous Field. Paper presented at the SPE Reservoir Simulation Symposium, San Antonio, Texas. 29137.

Du, S., Hosseini,S.A., Zhou, Y., and King, M.J. 2010. Effective Local and Extended Local Single–Phase Upscaling. In ECMOR XII.

Durlofsky, L.J. 1991. Numerical Calculation of Equivalent Grid Block Permeability Tensors for Heterogeneous Porous Media, *Water Resources Research* 27, 699.

Durlofsky, L.J., Jones, .R.C., and Milliken, W.J. 1997. A Non-Uniform Coarsening Approach for The Scale Up of Displacement Processes in Heterogeneous Porous Media. *Advances in Water Resources*, 20: 335-347.

Durlofsky, L.J., Milliken, W.J., and Bernath, A. 2000. Scaleup in the Near-Well Region. *SPE Journal* 5 (1). 61855.

Gupta, N. 2012. Rapid Estimation of Drainage Volume, Pressure and Rates in Heterogeneous Reservoirs. Master Thesis, Texas A&M University, Texas, USA.

Fincham, A.E., Christensen, J.R., Barker, J.W., and Samier, P. 2004. Upgridding from Geologic Model to Simulation Model: Review, Application and Limitations. Paper presented at the Annual Technical Conference and Exhibition, Houston, Texas. 90921.

Freeman, C. M., Moridis, G., Ilk, D. and Blasingame, T. A. 2009. A Numerical Study of Performance for Tight Gas and Shale Gas Reservoir Systems, paper presented at SPE Annual Technical Conference and Exhibition, New Orleans, Louisiana. 124961.

Holden, L. and Nielsen, B.F. 2000. Global Upscaling of Permeability in Heterogeneous Reservoirs: The Output Least Squares (OLS) Method. *Transport in Porous Media* 40: 115-143.

Holditch, S. A., 2006. Tight Gas Sands. *Journal of Petroleum Technology* 58(6): 86-94.

Hosseini, S.A. and Kelkar, M.G. 2010. Analytical Upgridding Method to Preserve Dynamic Flow Behavior. *SPE Reservoir Evaluation & Engineering*. 473-484.

Isaaks, E.H., Srivastava, M. 1989. An Introduction to Applied Geostatistics. Oxford University Press, New York, USA.

Kang, S., Datta-Gupta, A., Lee, J. 2011. Impact of natural fractures in drainage volume calculations and optimal well placement in tight gas reservoirs. Paper presented at the SPE North American Unconventional Gas Conference and Exhibition, The Woodlands, Texas. 144338.

Kasap, E. and Lake, L.W. 1990. Calculating the Effective Permeability Tensor of a Gridblock. *SPEFE*, 192-200.

Kelkar, M.G. and Atiq, M. 2010. Upgridding Method for Tight Gas Reservoirs. Paper presented at the SPE Annual Technical Conference and Exhibition, Florence, Italy. 133301.

King, M.J. 1995. Application and Analysis of a New Method for Calculating Tensor Permeability in New Developments in Improved Oil Recovery, ed. H.J. de Haan, Geological Society Special Publication 84, Geological Society Publications, Bath, UK.

King, M.J. 2007A. Recent Advances in Upgridding. *Oil & Gas Science and Technology - Rev. IFP*, 62(2): 195-205.

King, M.J. 2007B. Upgridding and Upscaling: Current Trends and Future Directions. SPE Distinguished Lecture. 112810.

King, M.J., Abacioglu, Y., Ballin, P.R., Sebastian, H.M., Du, S., Zhou, Y. 2013. Multiscale Grid Design for a Full Field Tight Gas Reservoir on a Next Generation Simulator, paper presented at SPE Middle East Unconventional Gas Conference and Exhibition, Muscat, Oman, 163993.

King, M.J., Burn, K.S., Wang, P., Venkataramanan, M., Alvarado, F., Ma, X., and Datta-Gupta, A. 2006. Optimal Coarsening of 3D Reservoir Models for Flow Simulation. *SPE Reservoir Evaluation & Engineering* 9: 317-334.

King, M.J., MacDonald, D.G., Todd, S.P., Leung, H. 1998. Application of Novel Upscaling Approaches to the Magnus and Andrew Reservoirs. Paper presented at the European Petroleum Conference, The Hague, Netherlands. 50643.

Li, D. and Beckner, B. 2000. Optimal Uplayering for Scaleup of Multimillion-Cell Geologic Models. Paper presented at the SPE Annual Technical Conference and Exhibition, Dallas, Texas. 62927.

Li D., Cullick, A.S., and Lake, L.W. 1995 Global Scale-Up of Reservoir Model Permeability with Local Grid Refinement. *J. Petrol. Sci. Eng.* 14: 1-13.

Lee, W. J., Hopkins, C. W. 1994. Characterization of Tight Reservoirs. *Journal of Petroleum Technology*, 46(11): 956-964.

Lee, W.J. 1982. *Well Testing.* SPE Textbook Series. Richardson, TX: Society of Petroleum Engineers. Original edition.

Manceau, E., Mezghani, M., Zabalza-Mezghani, I., and Roggero, F. 2001. Combination of Experimental Design and Joint Modeling Methods for Quantifying the Risk Associated with Deterministic and Stochastic Uncertainties-An Integrated Test Study. SPE Paper presented at the 2001 SPE Annual technical Conference & Exhibition, New Orleans, Louisiana, USA. 71620.

Muggeridge, A.H., Cuypers, M., Bacquet, C. et al. 2002. Scale-up of Well Performance for Reservoir Flow Simulation. *Petroleum Geoscience* 8 (2): 133-139.

Nexus ® *Technical Reference Guide*. 2010. Halliburton Landmark Software and Services.

Petrel ® *Technical Reference Guide*. 2011. Schlumberger Software and Services.

Pickup G.E., Ringrose, P.S., Jensen, J.L. and Sorbie, K.S. 1994. Permeability Tensors for Sedimentary Structures. *Mathematical Geology* 26: 227-250.

Sablok, R. and Aziz, K. 2005. Upscaling and Discretization Errors. Paper presented at the Reservoir Simulation Symposium, Houston, Texas. 93372.

Sarma, P., Chen, W.H. 2008. Efficient Well Placement Optimization with Gradient-Based Algorithms and Adjoint Models. SPE paper presented at the SPE Intelligent Energy Conference and Exhibition, Amsterdam, Netherlands. 112257.

Stern, D. and Dawson, A.G. 1999. A Technique for Generating Reservoir Simulation Grids to Preserve Geologic Heterogeneity. Paper presented at the Reservoir Simulation Symposium, Houston, Texas. 51942.

Taware, S., Park, H., Datta-Gupta, A., Bhattacharya, S., Tomar, A.K., Kumar, M., Rao, H.S. 2012. Well Placement Optimization in A Mature Carbonate Waterflood Using Streamline-Based Quality Maps. Paper presented at the SPE Oil and Gas India Conference and Exhibition, Mumbai, India. 155055.

Tobin, R.C., McClain, T., Lieber, R.B., Ozkan, A., Banfield, L.A., Marchand, A.M.E. and McRae, L.E. 2010. Reservoir Quality Modeling of Tight-Gas Sands in Wamsutter Field: Integration of Diagenesis, Petroleum Systems, and Production Data. *AAPG Bulletin* 94 (8): 1229-1266.

Vasco, D., Keers, H., and Harasaki, K. 2000. Estimation of Reservoir Properties Using Transient Pressure Data: An Asymptotic Approach. *Water Resources Research* 36 (12): 3447-3465.

Virieux, J., Flores-Luna, C. and Gilbert, D. 1994. Asymptotic Theory for Diffusive Electromagnetic Imaging. *Geophysics J. Int*. 119: 857-868.

Vlemmix, S., Joosten, G.J.P., Brouwer, D.R., Jansen, J.D. 2009. Adjoint-Based Well Trajectory Optimization in A Thin Oil Rim. Paper presented at SPE EUROPEC/EAGE Annual Conference and Exhibition, Amsterdam, Netherlands. 121891.

Wen, X.-H., Durlofsky, L.J. and Edwards, M.G. 2003. Use of Border Regions for Improved Permeability Upscaling. *Mathematical Geology* 35: 521-547.

White, C.D. and Horne, R.N. 1987. Computing Absolute Transmissibility in the Presence of Fine Scale Heterogeneity, SPE Paper presented at the Reservoir Simulation Symposium, San Antonio, Texas. 16011.

Wu, X.H., Stone, M.T., Parashkevov, R.R., Stern, D., and Lyons, S.L. 2007. Reservoir Modeling with Global Scaleup. SPE Paper presented at the Middle East Oil & Gas Show, Kingdom of Bahrain. 105237.

Xie, J., Gupta, N., King, M.J. 2012. Depth of Investigation and Depletion Behavior in Unconventional Reservoirs Using Fast Marching Methods. Paper presented at the EAGE Annual Conference & Exhibition incorporating SPE Europec, Copenhagen, Denmark. 154532.

Yeten, B., Durlofsky, L., Aziz, K. 2003. Optimization of Nonconventional Well Type, Location, and Trajectory. *SPE Journal* 8 (3): 200-10.

Yuen, B., Rashid, O., Al-Shammari, M., Al-Ajmi, F., Pham, T., Rabah, M., Moreno, J. C. 2011. Optimizing Development Well Placements Within Geological Uncertainty Utilizing Sector Models. SPE paper presented at SPE Reservoir Characterisation and Simulation Conference and Exhibition, Abu Dhabi, UAE. 148017.

Zhou, Y., King, M.J., Du, S. 2013. A Simulation-Free Approach for Well Placement in Tight Gas Reservoirs. IPTC paper presented at the International Petroleum Technology Conference, Beijing, China. 16887.

Zhou, Y., King, M.J. 2011. Improved Upscaling for Flow Simulation of Tight Gas Reservoir Models. SPE paper presented at 2011 SPE Annual Technical Conference and Exhibition, Denver, Colorado, 147355.

NOMENCLATURE

A = *cross surface area*

A_o = *amplitude of the leading order asymptotic solution*

B = *fluid formation volume factor*

c_t = *total compressibility*

DX = *cell length in x axis*

DY = *cell length in y axis*

DZ = *cell length in z axis*

h = *thickness*

k = *permeability vector*

k_x = *permeability in x direction*

k_y = *permeability in y direction*

k_z = *permeability in z direction*

p = *pressure*

$\tilde{p}$ = *fourier transformed pressure*

p_{wf} = *bottom hore pressure*

q = *darcy flux*

q_w = *well rate*

r_w = *wellbore radius*

RP = *recovery potential*

s = *skin factor*

t = *time*

t_x = *diffusive time in x direction*

t_z = *diffusive time in z direction*

V_p = *drainage volume*

α = *diffusivity*

ϕ = *porosity*

μ = *viscosity*

δ = *difference*

∇ = *gradient*

γ = *semi-variance*

τ = *diffusive time of flight*

ξ = *Boltzmann variable*

ω = *frequency*

APPENDIX A: UNCERTAINTY INDEX

The difference between the true value and corresponding estimate will be the error, or residual for Kriging interpretation.

$$R(x_0) = \hat{V}(x_0) - V(x_0) \tag{A-1}$$

Here, $\hat{V}(x_0)$ is the estimate, and $V(x_0)$ is the true value, at location x_0.

The error variance can also be considered as the uncertainty risk for the estimated values.

$$Var\{R(x_0)\} = Cov\{\hat{V}(x_0)\hat{V}(x_0)\} - 2Cov\{\hat{V}(x_0)V(x_0)\} + Cov\{V(x_0)V(x_0)\} \tag{A-2}$$

From the Kriging interpretation, we know that:

$$\hat{V}(x_0) = \sum_{i=1}^{n} w_i \cdot V_i \tag{A-3}$$

The unknown value at location x_0 is the weighted linear combination of the known values at location x_i , $i = 1, 2, \cdots n$, w_i is the Kriging interpretation weight at location i. Therefore, the variance of the estimate value is:

$$Cov\{\hat{V}(x_0)\hat{V}(x_0)\} = Var\{\hat{V}(x_0)\} = Var\{\sum_{i=1}^{n} w_i \cdot V_i\} = \sum_{i=1}^{n}\sum_{j=1}^{n} w_i \cdot w_j \cdot C_{ij} \tag{A-4}$$

Where, C_{ij} is the covariance of the known values at location i and j.

$$2Cov\{\hat{V}(x_0)V(x_0)\} = 2Cov\{\left(\sum_{i=1}^{n} w_i \cdot V_i\right) \cdot V_0\} = 2\sum_{i=1}^{n} w_i \cdot Cov\{V_i \cdot V_0\} = 2\sum_{i=1}^{n} w_i \cdot C_{i0} \tag{A-5}$$

Where, C_{i0} is the covariance of the known values at location i and unknown location 0.

$$Cov\{V(x_0)V(x_0)\} = C_{00} \tag{A-6}$$

Where, C_{00} is the variance of unknown values at location 0.

Combine Eq. (A-2), Eq. (A-4), Eq. (A-5), Eq. (A-6), we have:

$$Var\{R(x_0)\} = C_{00} + \sum_i^n \sum_j^n w_i w_j C_{ij} - 2\sum_i^n w_i C_{i0} \quad \text{(A-7)}$$

Isaaks & Srivastava (1989) also utilized Eq. (A-7) to access the uncertainty that associated with the estimates, which proves Eq. (3-7), when the known values are at well locations. The first term C_{00} represents the variance of the estimates, or the areas we do not have the reliable measurements, and it accounts for the variance of the data under study. As the data becomes more variable, more risk is expected. The second term $\sum_i^n \sum_j^n w_i w_j C_{ij}$ is a weighted sum of all the covariances between the various well locations. The weights are obtained through Kriging interpretation, acting as an inverse distance. If the wells are far apart, this term will be relatively small, and uncertainty or risk will be also small. This accounts for the clustering by increasing the uncertainty if we use measurements for interpretation that are too close together. The third term $2\sum_i^n w_i C_{i0}$ is a weighted sum of the covariances between the interested area and well locations. It accounts for the proximity of the existing well locations from a spatial connectivity perspective. If the distance is too far, this term will be small, and risk will increase due to the negative sign.

Then we need calculate the weight that assigned to each known location, in the Kriging interpretation.

We have:

$$\sum_{i=1}^n w_i = 1 \quad \text{(A-8)}$$

Combine Eq. (A-7) and Eq. (A-8), we have:

$$\sigma_R^{\,2} = \sigma^2 + \sum_i^n \sum_j^n w_i w_j C_{ij} - 2\sum_i^n w_i C_{i0} + 2\mu\left(\sum_{i=1}^n w_i - 1\right) \tag{A-9}$$

Where, μ is introduced to incorporate the Eq. (A-8) into Eq. (A-7), and needs to be determined. Kriging interpretation will minimize the estimates variance, therefore, we could have

$$\begin{aligned}
&\frac{\partial\left(\sigma_R^{\,2}\right)}{\partial w_1} = 2\sum_j^n w_j C_{1j} - 2C_{10} + 2\mu = 0 \quad \Rightarrow \quad \sum_j^n w_j C_{1j} + \mu = C_{10} \\
&\qquad\qquad \vdots \\
&\frac{\partial\left(\sigma_R^{\,2}\right)}{\partial w_i} = 2\sum_j^n w_j C_{ij} - 2C_{i0} + 2\mu = 0 \quad \Rightarrow \quad \sum_j^n w_j C_{ij} + \mu = C_{i0} \\
&\qquad\qquad \vdots \\
&\frac{\partial\left(\sigma_R^{\,2}\right)}{\partial w_n} = 2\sum_j^n w_j C_{nj} - 2C_{n0} + 2\mu = 0 \quad \Rightarrow \quad \sum_j^n w_j C_{nj} + \mu = C_{n0}
\end{aligned} \tag{A-10}$$

The weight at each location could be determined through Eq. (A-10), which could be simplified as following:

$$\begin{bmatrix} C_{11} & \cdots & C_{1n} & 1 \\ \vdots & \ddots & \vdots & \vdots \\ C_{n1} & \cdots & C_{nn} & 1 \\ 1 & \cdots & 1 & 0 \end{bmatrix} \bullet \begin{bmatrix} w_1 \\ \vdots \\ w_n \\ \mu \end{bmatrix} = \begin{bmatrix} C_{10} \\ \vdots \\ C_{n0} \\ 1 \end{bmatrix} \tag{A-11}$$

Eq. (A-10) is utilized in our work to determine the uncertainty, as discussed in section 3.

APPENDIX B: AN ILLUSTRATION OF THE FAST MARCHING METHOD

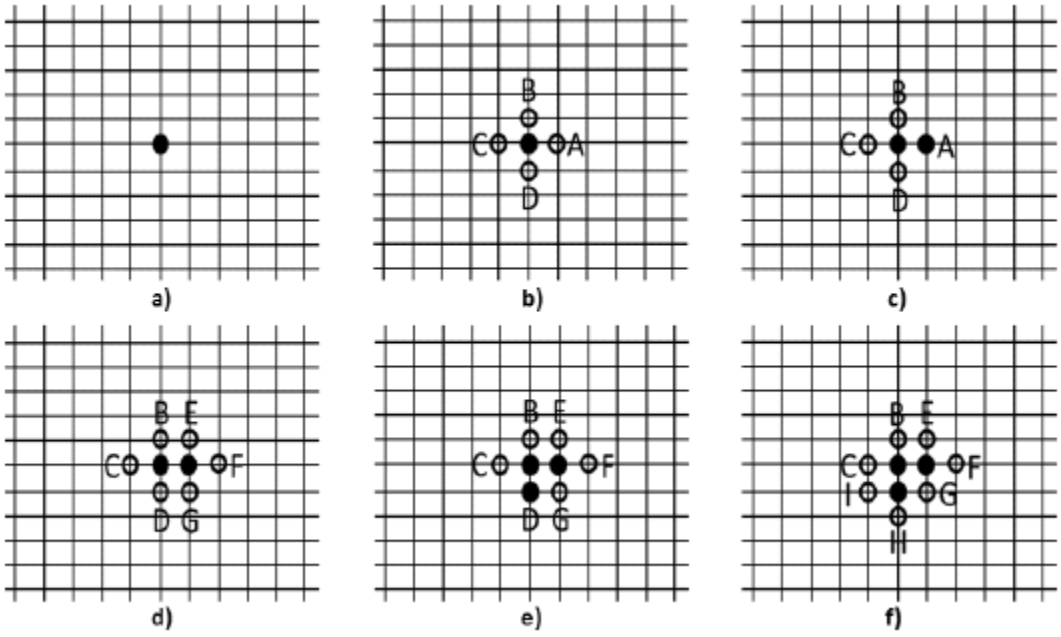

Figure B-1. Schematic description of the fast marching method showing the propagation of pressure waves in an orthogonal mesh grid

Figure B-1 shows an illustration of the Fast Marching Method, where the well location is first labeled as 'accepted' points (τ=0). Their adjacent nodes are labeled as 'neighbor' points and the rest nodes are called 'far-away' points. Now to calculate the arrival time at each point, the following procedure is applied:

1. Start from the 'accepted' points,
2. Calculate the arrival time of their 'neighbor' points (A, B, C, D, etc.) using the finite difference approximation
3. Pick the minimum arrival time in the current 'neighbor' points,
    - Label it as 'accepted' (e.g., Point A in B-1b)

- Add its neighbors that are in ‘far-away’ as ‘neighbors’, (e.g., Points E, F & G in B-1d)

4. Repeat steps 2 and 3 until all the points in the domain are labeled as ‘accepted’.

By applying the FMM approach, the arrival time for each node has been estimated in terms of diffusive time of flight. Once the conversion from diffusive time of flight to actual time is known, then the drainage volume at any time can easily be calculated by summing up the pore volumes of the mesh grids inside that time contour. But overall, the drainage volume calculation can be expressed in simple mathematical terms as Eq.(B-1):

$$V_p(t) = \sum_{i}^{i=N\ Cells} \text{Cell Pore Volumes (where } t_i < t) \qquad \text{(B-1)}$$

Where t_i denotes the arrival time for a particular cell and t denotes the time at which the drainage volume is being calculated.

The issue here is how to get the conversion from diffusive time of flight to actual time. Gupta et al. (2012) shows that when the flow type in the reservoir is symmetrical and known, the diffusive time of flight can be converted to actual time by using the corresponding constant conversion coefficient. However, for a heterogeneous reservoir with unsymmetrical flow, constant conversion coefficient does not work.